QUANTUM PHENOMENA FOR NEXT GENERATION COMPUTING

A Dissertation

Submitted to the Faculty

of

Purdue University

by

Chin-Yi Chen

In Partial Fulfillment of the

Requirements for the Degree

of

Doctor of Philosophy

May 2020

Purdue University

West Lafayette, Indiana

# THE PURDUE UNIVERSITY GRADUATE SCHOOL
# STATEMENT OF DISSERTATION APPROVAL

Dr. Gerhard Klimeck, Chair

    School of Electrical and Computer Engineering, Purdue Universality

Dr. Joerg Appenzeller

    School of Electrical and Computer Engineering, Purdue Universality

Dr. Mykhailo Povolotskyi

    School of Electrical and Computer Engineering, Purdue Universality

Dr. Mark J. Rodwell

    School of Electrical and Computer Engineering, UCSB

Dr. Zhihong Chen

    School of Electrical and Computer Engineering, Purdue Universality

**Approved by:**

    Dr. Dimitrios Peroulis

        Head of the School Graduate Program

I express my sincere gratitude to my advisor, family, friends, and all who have supported me differently during my Ph.D.

ACKNOWLEDGMENTS

TABLE OF CONTENTS

LIST OF TABLES

LIST OF FIGURES

Figure                                                                    Page

ABSTRACT

Chin-Yi Chen Ph.D., Purdue University, May 2020. Quantum phenomena for next generation computing. Major Professor: Gerhard Klimeck.

With the transistor dimensions scaling down to a few atoms, quantum phenomena - like quantum tunneling and entanglement - will dictate the operation and performance of the next generation of electronic devices, post-CMOS era. While quantum tunneling limits the scaling of the conventional transistor, Tunneling Field Effect Transistor (TFET) employs band-to-band tunneling for the device operation. This mechanism can reduce the sub-threshold swing (S.S.) beyond the Boltzmann's limit, which is fundamentally limited to 60 mV/dec in a conventional Si-based metal-oxide-semiconductor field-effect transistor (MOSFET). A smaller S.S. ensures TFET operation at a lower supply voltage and, therefore, at lesser power compared to the conventional Si-based MOSFET.

However, the low transmission probability of the band-to-band tunneling mechanism limits the ON-current of a TFET. This can be improved by reducing the body thickness of the devices i.e., using 2-Dimensional (2D) materials or by utilizing heterojunction designs. In this thesis, two promising methods are proposed to increase the ON-current; one for the 2D material TFETs, and another for the III-V heterojunction TFETs.

Maximizing the ON-current in a 2D material TFET by determining an optimum channel thickness, using compact models, is presented. A compact model is derived from rigorous atomistic quantum transport simulations. A new doping profile is proposed for the III-V triple heterojunction TFET to achieve a high ON-current. The optimized ON-current is 325 $\mu A/\mu m$ at a supply voltage of 0.3 V. The device

design is optimized by atomistic quantum transport simulations for a body thickness of 12 nm, which is experimentally feasible.

However, increasing the device's body thickness increases the atomistic quantum transport simulation time. The simulation of a device with a body thickness of over 12 nm is computationally intensive. Therefore, approximate methods like the mode-space approach are employed to reduce the simulation time. In this thesis, the development of the mode-space approximation in modeling the triple heterojunction TFET is also documented.

In addition to the TFETs, quantum computing is an emerging field that utilizes quantum phenomena to facilitate information processing. An extra chapter is devoted to the electronic structure calculations of the Si:P $\delta$-doped layer, using the empirical tight-binding method. The calculations agree with angle-resolved photoemission spectroscopy (ARPES) measurements. The Si:P $\delta$-doped layer is extensively used as contacts in the Phosphorus donor-based quantum computing systems. Understanding its electronic structure paves the way towards the scaling of Phosphorus donor-based quantum computing devices in the future.

# 1. A PROMISING CANDIDATE FOR LOW POWER COMPUTATIONS: TUNNELING FIELD-EFFECT TRANSISTORS

## 1.1 Power consumption of a transistor

The power consumption of a conventional transistor has two parts; the static power consumption $(P_{static})$ and the dynamic power consumption $(P_{dynamic})$:

$$P_{static} = I_{off} \, V_{DD}, \tag{1.1}$$

$$P_{dynamic} = f \, C_g \, V_{DD}^2, \tag{1.2}$$

where $V_{DD}$ is the supply voltage, $I_{off}$ is the leakage current at the OFF-state. $C_g$ is the transistor's gate capacitance and $f$ is the operating frequency [1–4].

Reducing the supply voltage $(V_{DD})$ is the most efficient way to reduce both the static power consumption and dynamic power consumption. However, the supply voltage of the conventional Si-based metal-oxide-semiconductor field-effect transistor (MOSFET) appears to have been nearly saturated since the beginning of the millennium. Fig. 1.1 shows the scaling of the supply voltage $(V_{DD})$ and the feature size of the MOSFET over the years, since 1990 [5]. While, the feature size scales by $\frac{1}{\sqrt{2}}$ every two years leading to doubling the density of the transistors in a chip, the supply voltage slows down after 2000 [3, 6, 7].

The supply voltage scaling of a MOSFET is inhibited by the fundamental limitation of its switching speed. Unlike MOSFETs, the tunneling field-effect transistors (TFETs) are not bound by this limit to the switching speed and can operate at a significantly lower voltage [7, 10–19]. This makes TFETs an appealing alternative to MOSFETs for low power applications [20, 21]. In the following section, the working
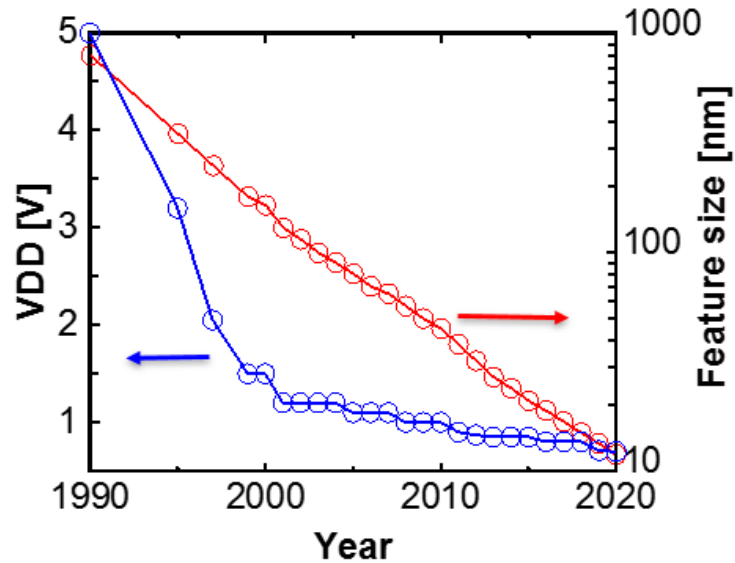
Fig. 1.1.: The scaling of the supply voltage ($V_{DD}$) and feature size of MOSFET over four decades. The data is extracted from ITRS's road-map [5, 8, 9].

principles of MOSFET and TFET are introduced, and the challenges of TFETs will also be discussed.

## 1.2 MOSFET's working principle and its fundamental limit

Fig. 1.2 (a) shows the schematic of an N-channel MOSFET with four terminals to apply different voltage bias: drain, source, gate, and body. The gate terminal is separated from the body by an oxide layer and a metal layer. The source and drain terminals are connected to highly N-doped regions while the body terminal is connected to an intrinsic or lightly P-doped substrate.

The switching speed of a MOSFET is determined from its transfer-characteristics ($\text{Log}_{10}(I_D)$-$V_G$ curve), as shown in Fig. 1.2 (b). The source and body terminals are grounded ($V_S = V_B = 0$ V). The voltage applied to the drain terminal is the supply voltage ($V_D = V_{DD}$). The voltage applied at the gate terminal ($V_G$) controls the

channel resistance and regulates the drain current ($I_D$). The maximum voltage that can be applied to $V_G$ is the supply voltage ($V_G < V_{DD}$).

The switching speed is quantified through the metric called sub-threshold swing (SS), which is defined as $[\frac{\partial Log_{10}(I_D)}{\partial V_G}]^{-1}$ in the sub-threshold regime. A transistor with a high sub-threshold swing requires a high $V_G$ to switch the transistor from OFF state to ON state, and therefore, a large supply voltage is needed to operate the device.
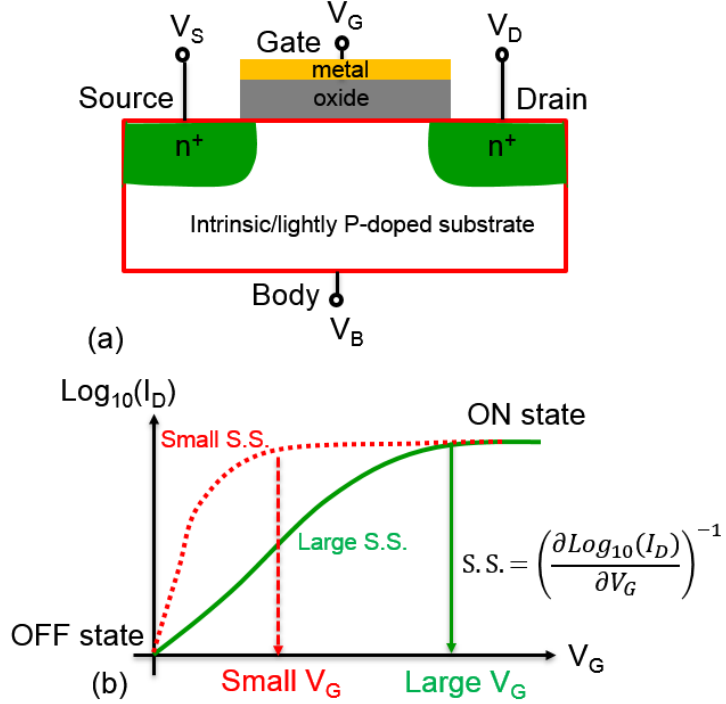


Fig. 1.2.: (a) The schematic of an N-channel metal-oxide-semiconductor field-effect transistor (MOSFET). $V_D$, $V_G$, $V_S$, and $V_B$ are the voltages applied to the drain, the gate, the source, and the body terminals, respectively. (b) The transfer-characteristics ($Log_{10}(I_D) - V_G$ curve) of an N-channel MOSFET. A smaller sub-threshold swing (S.S.) requires a smaller $V_G$ to switch the device from OFF state to ON state.

For decades, the semiconductor industry has explored various technologies and device designs to reduce the sub-threshold swing. However, the sub-threshold swing of a MOSFET is fundamentally limited to 60 mV/dec. Therefore, the supply voltage

can not be lower than 0.6 V in order to obtain a sufficient ON/OFF current ratio ($I_{ON}/I_{OFF}$). For example, an advanced 14 nm FinFET can not be operated with a supply voltage lower than 0.6 V [10].
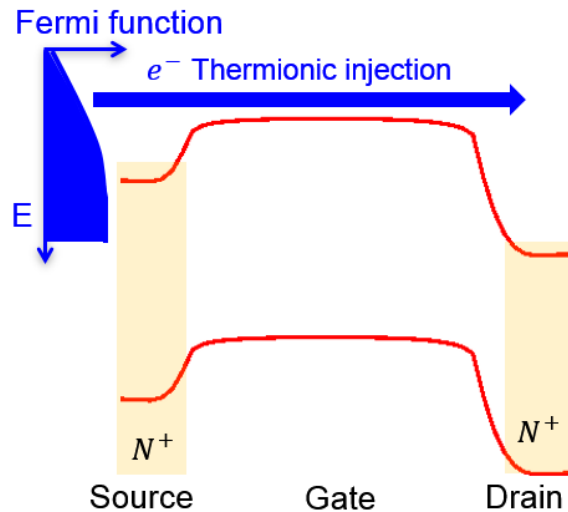


Fig. 1.3.: MOSFETs utilize the gate barrier to control the thermionic injection from the source region to the drain region. At room temperature, the sub-threshold swing is limited by the tail of the Fermi function such that the sub-threshold swing can not be smaller than 60mV/dec.

This limit to the sub-threshold swing is related to the Fermi function [22]. Fig. 1.3 shows the energy band diagram of an N-channel MOSFET along the channel. Since the source terminal is grounded while the drain terminal is connected to the supply voltage, the electron potential energy in the drain region is lower than the source region. The electrons tend to flow from the source region to the drain region. The voltage applied at the gate terminal controls the potential barrier in the channel and controls the electron thermionic injection from source to drain.

The electrons in the source and drain region are in thermal equilibrium, and the Fermi function determines the probability that a state at energy "E" is occupied:

$$f_{fermi}(E) = \frac{1}{(1 + e^{(E-E_f)/kT})} \qquad (1.3)$$

Where $E_f$ is the Fermi energy. At room temperature, the Fermi function has a tail, which indicates that the electrons can occupy an energy level higher than the channel potential barrier. These high energy electrons can thermally inject into the channel that increases the OFF-state leakage current and the sub-threshold swing. As a result, the limit of the sub-threshold swing comes from this tail of the Fermi function, which is 60mV/dec ($= \frac{kT}{e} \times log(10)$).

## 1.3   TFET's working principle

TFET is operated by the band-to-band tunneling mechanism, instead of the thermionic injection. The sub-threshold swing is then not limited by the tail of the Fermi function [16–21]. Fig. 1.4 shows the energy band diagram of an N-channel TFET. Unlike the N-channel MOSFET, where the source region is N-type, the source of an N-channel TFET is doped to P-type.

When TFET operates in the ON-state, the positive gate bias pulls down the potential in the channel such that the conduction band in the channel is lower than the valence band in the source. The electrons in the source can tunnel to the channel and conduct current. When the device operates in the OFF state, the tail of the Fermi function is filtered by the bandgap ($E_g$). The tail of the Fermi function does not contribute to the leakage current, and the sub-threshold swing can be steeper than 60 mV/dec. As a result, TFETs can operate with a significantly lower supply voltage [16–21].

## 1.4   TFET's problem: low ON-current

However, TFET has has a challenge - its ON-current is limited by the low transmission probability of the band-to-band tunneling mechanism. Many proposals are presented to improve low ON-current issue of the TFET; for example, 1) use of atom-
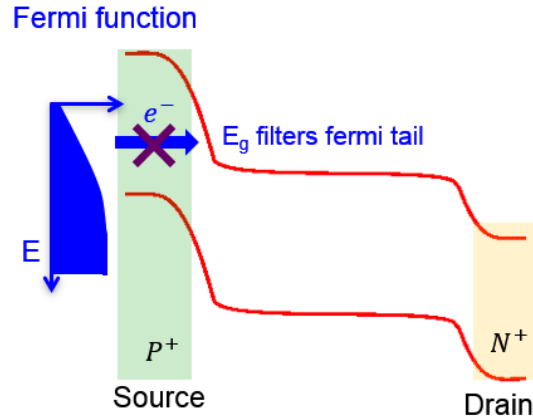
Fig. 1.4.: TFET utilizes the band-to-band tunneling (BTBT) mechanism to operate the device. The tail of the Fermi function is filtered by the bandgap ($E_g$). As a result, the sub-threshold swing is not limited by the tail of the Fermi function and can be smaller than 60mV/dec.

ically thin 2D materials as channel material to have an improved gate control [23–26], 2) optimize the electrostatic gating design to reduce the tunneling distance [27–29], and 3) use broken-gap or staggered-gap heterojunction designs to increase the transmission probability [10–14, 30].

In this thesis, two methods are proposed to increase the ON-current of TFETs; one for the 2D material TFETs, and another for the III-V heterojunction TFETs. For the 2D material TFETs, a compact model analysis for the optimum channel thickness is proposed towards maximizing the ON-current. For III-V heterojunction TFETs, a new doping profile is proposed for the triple heterojunction TFET. The ON-current reaches 325 $\mu$A/$\mu$m with a low supply voltage of 0.3 V. The device design is optimized by atomistic quantum transport simulations for a body thickness of 12 nm, which is possible to be realized experimentally.

## 1.5 Channel thickness optimization for ultrathin and 2-D chemically doped TFETs

2D material based tunnel FETs are among the most promising candidates for low power electronic applications, since they offer ultimate gate control and high current drives that are achievable through small tunneling distances ($\Lambda$) during the device operation. The ideal device is characterized by a minimized $\Lambda$. However, devices with the thinnest possible body do not necessarily provide the best performance. For example, reducing the channel thickness ($T_{ch}$) increases the depletion width in the source which can be a significant part of the total $\Lambda$. Hence, it is important to determine the optimum $T_{ch}$ for each channel material individually. In chapter 2, the optimum $T_{ch}$ for three channel materials: $WSe_2$, Black Phosphorus (BP), and InAs is studied, using full-band self-consistent quantum transport simulations. To identify the ideal $T_{ch}$ for each material at a specific doping density, a new analytic model is proposed and benchmarked against the numerical simulations.

## 1.6 Model III-V triple heterojunction double-gated TFET modeled with atomistic mode-space approximation

The triple heterojunction TFET has been proposed to increase the ON-current by forming two quantum wells in the tunnel junction to decrease tunneling distance and introduce resonant-enhanced tunneling [31, 32]. [33] used quantum transport simulations to optimize the triple heterojunction TFETs and reported a design with a high ON-current of 392 $\mu A/\mu m$. The design avoids using Aluminium (Al) or Antimony (Sb) alloys in the channel since no dielectric material on these alloys has shown low interface-trap density.

However, this design is optimized for a channel thickness of 4 nm. Such a thin channel thickness is difficult to fabricate. To understand the triple heterojunction TFET's performance with a realistic dimension, we need to extend the channel thickness up to 10 nm [11, 34–38].

Also, the carrier transport in such devices is complex due to the presence of quantum wells and strong scattering. The full band atomistic non-equilibrium Green's function approach, including scattering, is required to model the carrier transport accurately. However, such simulations are computationally not feasible. To mitigate this issue, an empirical tight-binding mode-space approximation has been employed to simulate triple heterojunction TFETs with a body thickness of 12 nm. In chapter 3, the triple heterojunction TFET design is evaluated using this model and shows a sub-60mV/dec transfer-characteristic under realistic scattering conditions.

## 1.7   Engineering doping profile of triple heterojunction TFETs

When the triple heterojunction TFET's channel thickness exceeds 10 nm, the steep transfer characteristic degrades due to a weak gate control. In chapter 4, a new device design is proposed to improve the sub-threshold swing and the ON-current for the triple heterojunction TFET with a 12 nm channel thickness.

The traditional TFET consists of a P-doped source, an intrinsic channel, and an N-doped drain. In the proposed design, 1) the intrinsic channel quantum well is doped to N-type, and 2) the rest of the intrinsic channel is doped to P-type. The proposed triple heterojunction TFET design is shown in Fig. 1.5. The design is tailored for vertical Fin-TFET experiments such that the transport direction can be the crystal growth direction [36, 39]. The proposed design consists of a P-doped $In_{0.53}Ga_{0.47}As$ and $GaAs_{0.5}Sb_{0.5}$ source, N-doped InAs channel, P-doped InP channel, and an N-doped InP drain.

The P-doped $In_{0.53}Ga_{0.47}As$ and $Ga_{0.48}As_{0.51}Sb$ source have the doping density of $N_a = 5 \times 10^{19}$ $cm^{-3}$. The N-doped InAs quantum well has the doping density of $N_d = 2 \times 10^{19}$ $cm^{-3}$. The P-doped InP channel has the doping density of $N_a = 5 \times 10^{18}$ $cm^{-3}$. The N-doped InP drain has the doping density of $N_d = 2 \times 10^{19}$ $cm^{-3}$.

The proposed device has an ON-current of 325 $\mu A/\mu m$ and a sub-threshold swing of 35~ 40 mV/dec. It muse be noted that the details of the design, such as the body
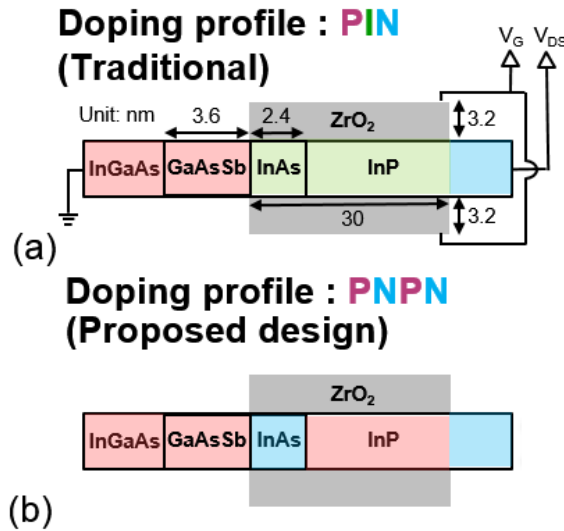
Fig. 1.5.: Triple heterojunction TFETs with (a) the traditional doping profile and (b) the proposed doping profile. In the proposed design, the InAs channel quantum well is doped to N-type while the rest of the InP channel is doped to P-type. When the channel thickness exceeds 10 nm, the proposed doping profile shows a better performance than the traditional doping profile.

thickness, the crystal growth direction, the choice of the material, the thickness of the quantum wells, and the doping density are carefully evaluated by the experimentalists to make sure that it is possible to fabricate the design.

# 2. CHANNEL THICKNESS OPTIMIZATION FOR ULTRATHIN AND 2-D CHEMICALLY DOPED TFETS

## 2.1 Abstract

2D material based TFETs are among the most promising candidates for low power electronics applications, since they offer ultimate gate control and high current drives that are achievable through small tunneling distances ($\Lambda$) during the device operation. The ideal device is characterized by a minimized $\Lambda$. However, devices with the thinnest possible body do not necessarily provide the best performance. For example, reducing the channel thickness ($T_{ch}$) increases the depletion width in the source which can be a significant part of the total $\Lambda$. Hence, it is important to determine the optimum $T_{ch}$ for each channel material individually. In this work, we study the optimum $T_{ch}$ for three channel materials: $WSe_2$, Black Phosphorus (BP), and InAs using full-band self-consistent quantum transport simulations. To identify the ideal $T_{ch}$ for each material at a specific doping density, a new analytic model is proposed and benchmarked against the numerical simulations.

## 2.2 Introduction

The tunneling field-effect transistor's ON current $(I_{ON})$ is proportional to the band-to-band tunneling transmission probability $(T_{BTBT})$ which can be expressed in terms of both electrostatics and material properties [40] as

$$I_{ON} \propto T_{BTBT} \propto e^{-\Lambda\sqrt{m^*E_g}}, \tag{2.1}$$

where in the simplest picture $m^*$ is the reduced effective mass along the transport direction $(\frac{1}{m^*} = \frac{1}{m_e^*} + \frac{1}{m_h^*})$. $E_g$ is the band gap of the channel material and $\Lambda$ is the tunneling distance at the junction. Reducing $\Lambda\sqrt{m^*E_g}$ increases $T_{BTBT}$ and $I_{ON}$ exponentially.

For a chemically doped TFET, the total tunneling distance $(\Lambda)$ has two contributions [40, 41]: the depletion width $(W_D)$ in the doped source region and the scaling length $(\lambda)$ in the channel as shown in Fig. 2.1.
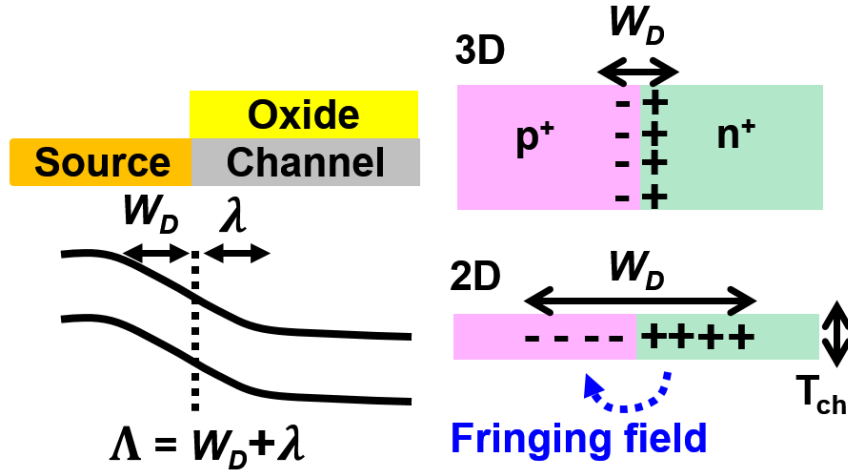


Fig. 2.1.: TFET's tunneling distance $(\Lambda)$ contains a depletion width $(W_D)$ in the source region and the scaling length $(\lambda)$ in the channel. $W_D$ of the 2D PN junction is larger than $W_D$ of the 3D PN junction due to the presence of fringing fields [42–45].

Reducing the channel thickness $(T_{ch})$ is beneficial in terms of electrostatics and may translate into a smaller $\Lambda$ [21] if for example $W_D$ does not depend on $T_{ch}$. In

reality, however, $W_D$ is thickness dependent in a low dimensional system (i.e. 2D material). This has been demonstrated experimentally [43], numerically, and analytically [42–45] where $W_D$ is larger in a 2D compared to a 3D PN junction.

Fig. 2.2 shows that $\lambda$ and $W_D$ respond to $T_{ch}$ in the opposite fashion as illustrated in the band diagrams extracted from atomistic simulations of a mono-layer (1ML) and a 5ML WSe$_2$ TFETs. When $T_{ch}$ is reduced from 5ML to 1ML, $\lambda$ is reduced due to the tighter gate control while $W_D$ increases. As a result, the thinnest possible $T_{ch}$ may not minimize $\Lambda$ as shown in Fig. 2.3.
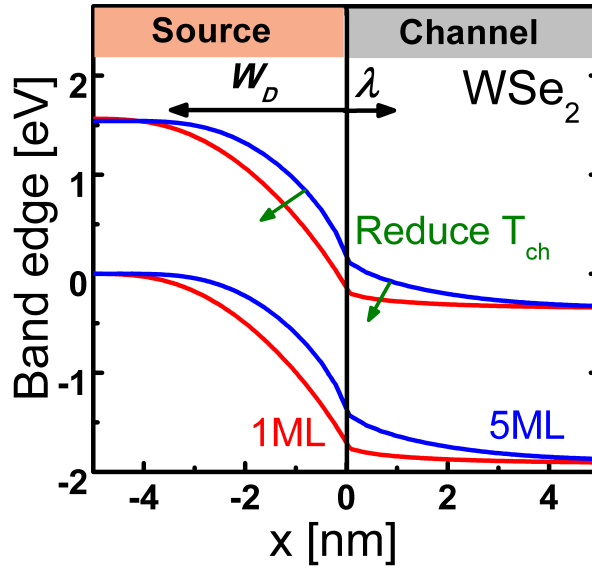


Fig. 2.2.: Band diagrams of a mono-layer and a 5ML WSe$_2$ TFET extracted from atomistic quantum transport simulations.

Moreover, the channel thickness $(T_{ch})$ that minimizes the total tunneling distance $(\Lambda)$ is not necessarily the best $T_{ch}$ overall since material parameters might change also with $T_{ch}$. To obtain the highest $I_{ON}$, the optimum $T_{ch}$ should minimize the entire expression $\Lambda\sqrt{m^*E_g}$. In this work, a compact model to optimize $T_{ch}$ for the ON state $(T_{ch.opt})$ is introduced, and the model is benchmarked with state-of-the-art atomistic quantum transport simulations.
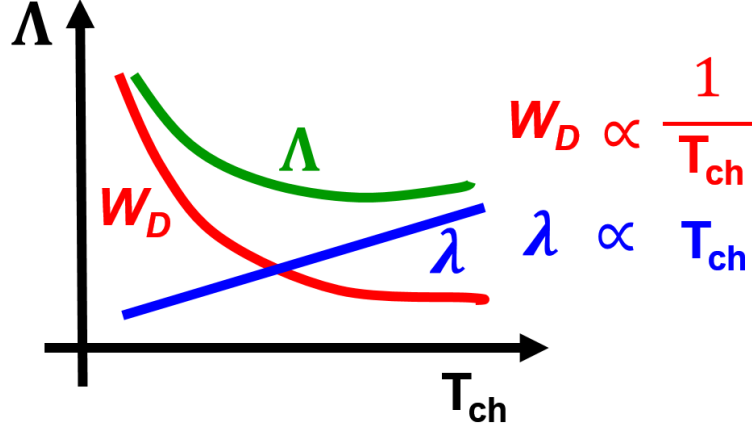
Fig. 2.3.: Scaling length ($\lambda$) is proportional to $T_{ch}$ while depletion width ($W_D$) is inversely proportional to $T_{ch}$. As a result, the thinnest possible $T_{ch}$ does not guarantee the smallest $\Lambda$.

Materials considered in this article can be classified depending on how their band gap changes with $T_{ch}$. As illustrated in Fig. 2.4, we define class I materials as those that do not show a dependence of $E_g$ on $T_{ch}$, which, as will be discussed below, results in thinner $T_{ch.opt}$ for optimum ON-state performance. On the other hand, class II materials, according to our definition, exhibit an increase of $E_g$ with decreasing $T_{ch}$. As a result, an optimum design is achieved with a relatively thicker $T_{ch.opt}$. Details are described later.

In sections III and IV, the impact of the body thickness on material properties and tunneling distance are discussed. Section V shows the optimized $T_{ch}$ for the ON-state obtained from an analytic analysis and atomistic quantum transport simulations. Section VI shows the upper limit of $T_{ch}$ in a TFET. Last, section VII summarizes the $T_{ch}$ design rules for a TFET.
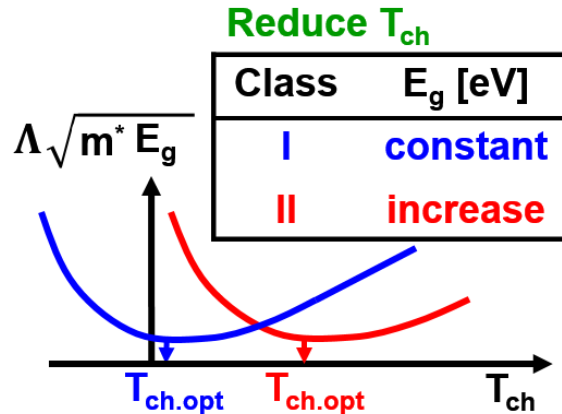
Fig. 2.4.: An optimum channel thickness $(T_{ch.opt})$ exists that minimizes $\Lambda\sqrt{m^*E_g}$. Depending on whether or not $E_g$ changes with the channel thickness $(T_{ch})$, the optimum body thickness $(T_{ch.opt})$ occurs at smaller or larger $T_{ch}$ respectively.

## 2.3  Device geometry

A schematic structure of the simulated double gated chemically doped TFET is shown in Fig. 2.5. The channel is 15 nm with the supply voltage $(V_{DD} = 0.5V)$ following the ITRS 15nm technology node [5]. The oxide is assumed to be HfO$_2$ with $\varepsilon_r = 25$ and an EOT of 0.5 nm. The source is heavily doped with density $10^{20}\ cm^{-3}$. An abrupt doping profile is assumed.
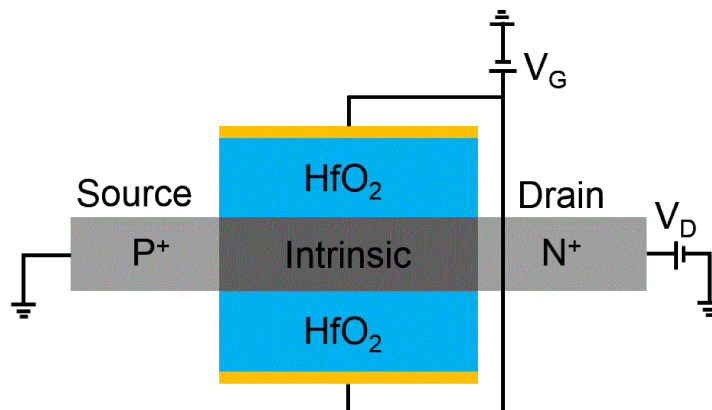


Fig. 2.5.: The simulated structure for the double-gated chemically doped TFETs.

## 2.4 The impact of $T_{ch}$ on $E_g$ and $m^*$

Three channel materials are considered in this work: WSe$_2$, BP, and InAs. BP and InAs are chosen, because their small direct $E_g$ is promising for TFET applications [23, 46–48]. Note that in the case of InAs, body thicknesses beyond what has been experimentally achieved were considered, and that in general transport in channels with $T_{ch}$ below 5 nm is strongly impacted by surface scattering [49, 50], while our model assumes that ballistic transport conditions prevail. WSe$_2$ is chosen as a case study, since its direct band gap ($E_g$) barely changes with $T_{ch}$. Moreover, WSe$_2$ based TFETs are expected to show the best performance among semiconducting transition metal dichalcogenides (TMDs) [24, 51, 52].

Fig. 2.6 shows $E_g$ and the tunneling mass $m^*$ of WSe$_2$, BP, and InAs extracted from atomistic tight binding simulations. The Slater-Koster tight binding parameters [53] of WSe$_2$ are derived from the band structure calculated by density function theory (DFT) with generalized gradient approximation (GGA) [51, 54]. Note that $E_g$ is not exactly the same as reported in some transport experiments [26], but is comparable.

$E_g$ and $m^*$ typically increase with stronger confinement achieved by reducing $T_{ch}$. The dependence of $E_g$ and $m^*$ on $T_{ch}$ can be expressed as $E_g = E_{g.bulk} + \frac{\alpha}{T_{ch}}$ and $m^* = m^*_{bulk} + \frac{\alpha'}{T_{ch}}$. $\alpha$ and $\alpha'$ are fitted to data in Fig. 2.6. The parameter $\alpha$ for the case of WSe$_2$ is significantly smaller than in the case of BP and InAs due to weak inter-layer coupling [55, 56].

## 2.5 The impact of $T_{ch}$ on the tunneling distance

In a 2D PN junction, $W_D$ is inversely proportional to the thickness [42].

$$W_D = \frac{\pi \varepsilon \Delta V}{q N T_{ch}} \tag{2.2}$$

where $N$ is the doping density and $\Delta V$ is the built-in potential. $\varepsilon$ is a regular averaged dielectric constant of the channel material and the dielectric surrounding the source.

Table 2.1.: Parameters $E_{g.bulk}$, $m^*_{bulk}$, $\alpha$, and $\alpha'$ for WSe$_2$, BP, and InAs.

| channel | $E_{g.bulk}$ | $\alpha$ | $m^*_{bulk}$ | $\alpha'$ |
|---------|--------------|----------|--------------|-----------|
|         | [eV]         | [eV.nm]  | $[m_0]$      | $[m_0.nm]$ |
| WSe$_2$ | 1.535        | 0.02     | 0.2          | 0.01      |
| BP      | 0.28         | 0.52     | 0.055        | 0.02      |
| InAs    | 0.35         | 1.5      | 0.025        | 0.035     |
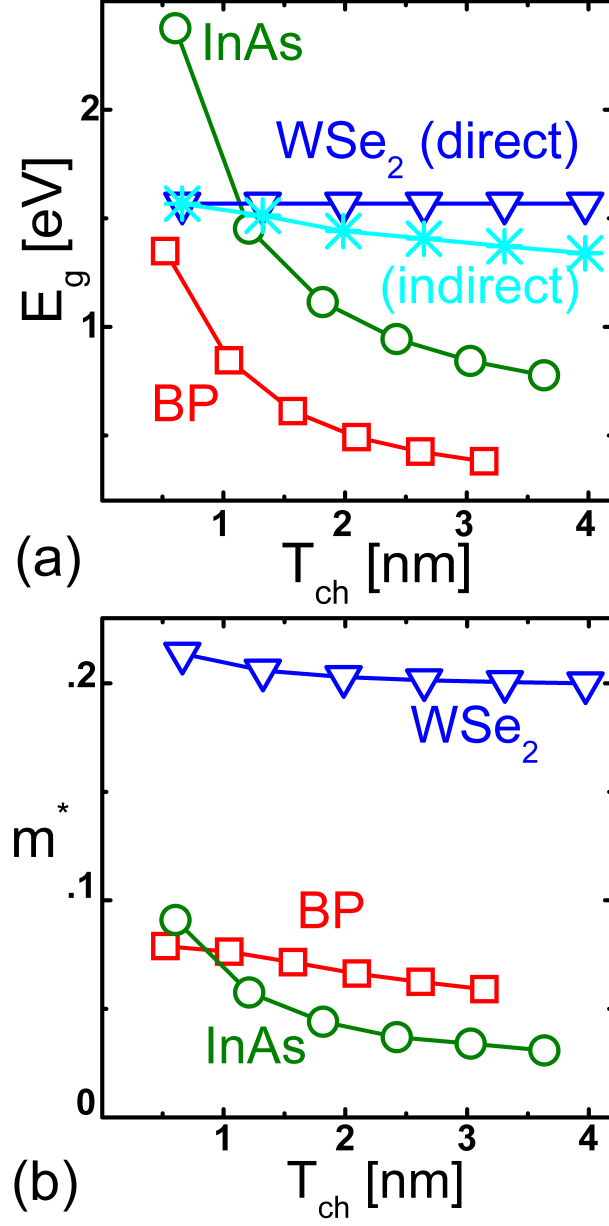
Fig. 2.6.: (a) and (b) show three studied channel materials' $E_g$ and tunneling mass $m^*$ as a function of $T_{ch}$ extracted from atomistic tight binding simulations, which are calibrated against density function theory (DFT).

The details of $\varepsilon$ are described in Appendix III. $\lambda$ for a chemically doped double gated 2D TFET [28] can be approximated as

$$\lambda = \frac{\varepsilon}{\varepsilon_{ox}} \left[ \gamma_1 T_{ch} + \gamma_2 T_{ox} \right] \qquad (2.3)$$

where $\varepsilon_{ox}$ and $T_{ox}$ are the dielectric constant and the thickness of the gate oxide, respectively. $\gamma_1$ and $\gamma_2$ are fitting parameters, since the expression without $\gamma_1$ and $\gamma_2$ was derived for an electrostatically doped 2D TFET [28,57].
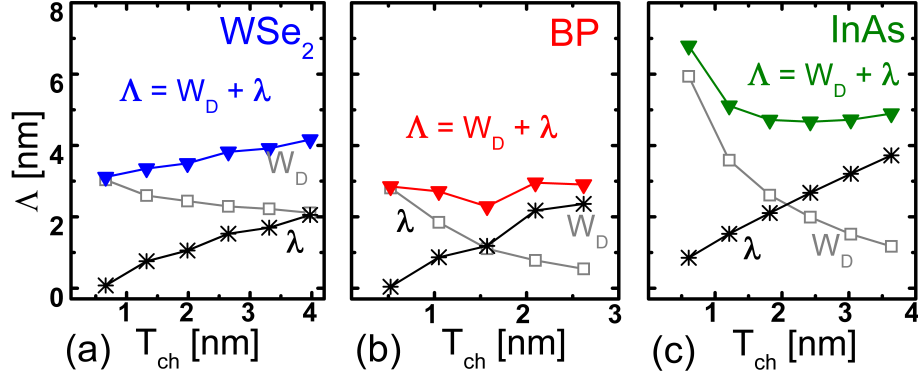


Fig. 2.7.: (a), (b), and (c) Dependence of $\Lambda$, $\lambda$, and $W_D$ on $T_{ch}$ for WSe$_2$, BP, and InAs TFETs, respectively.

WSe$_2$, BP, and InAs 2D TFETs' $\lambda$, $W_D$, and $\Lambda$ are shown in Fig. 2.7 (a), (b), and (c). The source doping density (N) is $10^{20}$ $cm^{-3}$. All simulated materials show that $\lambda$ is proportional to $T_{ch}$ while $W_D$ is inversely proportional to $T_{ch}$. The data are extracted from atomistic quantum transport simulations. The details of the simulation method is described in Appendix II. $W_D$ in the ON-state is proportional to the potential drop ($\Delta V$) across the depletion layer in the source, which is of the order of $E_g$. BP and InAs have a stronger dependence on $T_{ch}$ compared to WSe$_2$, their $E_g$ also shows a stronger dependence on $T_{ch}$.

## 2.6 The optimum $T_{ch}$ for ON-state ($T_{ch.opt}$)

The optimum $T_{ch}$ ($T_{ch.opt}$) for the ON-state minimizes $\Lambda\sqrt{m^*E_g}$ and is expected to maximize $I_{ON}$. The dependence of $\Lambda$, $m^*$, and $E_g$ on $T_{ch}$ has been discussed in

section III and IV. All of them can be expressed as a function of $T_{ch}$. As a result, $\Lambda\sqrt{m^*E_g}$ can also be expressed as a function of $T_{ch}$ and is given by

$$
\begin{aligned}
\Lambda&\sqrt{m^*E_g} \\
&= (\lambda + W_D)\sqrt{m^*E_g} \\
&= \left(c_0 T_{ch} + c_1 + c_2\frac{1}{T_{ch}} + c_3\frac{1}{T_{ch}^2}\right)c_4\sqrt{1 + c5\frac{1}{T_{ch}}}
\end{aligned}
\tag{2.4}
$$

parameters $c_0 \sim c_5$ are described in Appendix III in detail. Finding $T_{ch.opt}$ that minimizes $\Lambda\sqrt{m^*E_g}$ can be accomplished analytically or numerically. An exact analytic $T_{ch.opt}$ solved by $\frac{d\Lambda\sqrt{m^*E_g}}{dT_{ch}} = 0$ is complicated to interpret. Therefore, we will focus in the following on the numerical results by calculating $\Lambda\sqrt{m^*E_g}$ at different $T_{ch}$ and find $T_{ch.opt}$ as the minimum of those plots. Fig. 2.8 (a) shows $\Lambda\sqrt{m^*E_g}$ for WSe$_2$, BP, and InAs TFETs calculated form eq. (2.4), corresponding well with the results from atomistic quantum simulations.

It is apparent that WSe$_2$ as a class I material exhibits a smaller $T_{ch.opt}$ as mentioned before, since $\frac{\alpha}{E_{g.bulk}} << 0.5$ nm which is a single atomic layer's thickness. The body thicknesses of a single layer BP, InAs, and WSe$_2$ are 0.52 nm, 0.60 nm, and 0.66 nm, respectively. For a class II material like BP or InAs, $\frac{\alpha}{E_{g.bulk}}$ is larger than a monolayer's thickness which implies a larger $T_{ch.opt}$. Moreover, $T_{ch.opt}$ increases when the source doping density (N) decreases as apparent from Fig. 2.8(b), since $W_D$ inversely proportionally depends on N as stated above.

Table 2.2.: Classification of WSe$_2$, BP, and InAs.

| | WSe$_2$ | BP | InAs |
|---|---|---|---|
| $\alpha/E_{g.bulk}$ [nm] | 0.01 | 1.8 | 4.3 |
| Class | I | II | II |
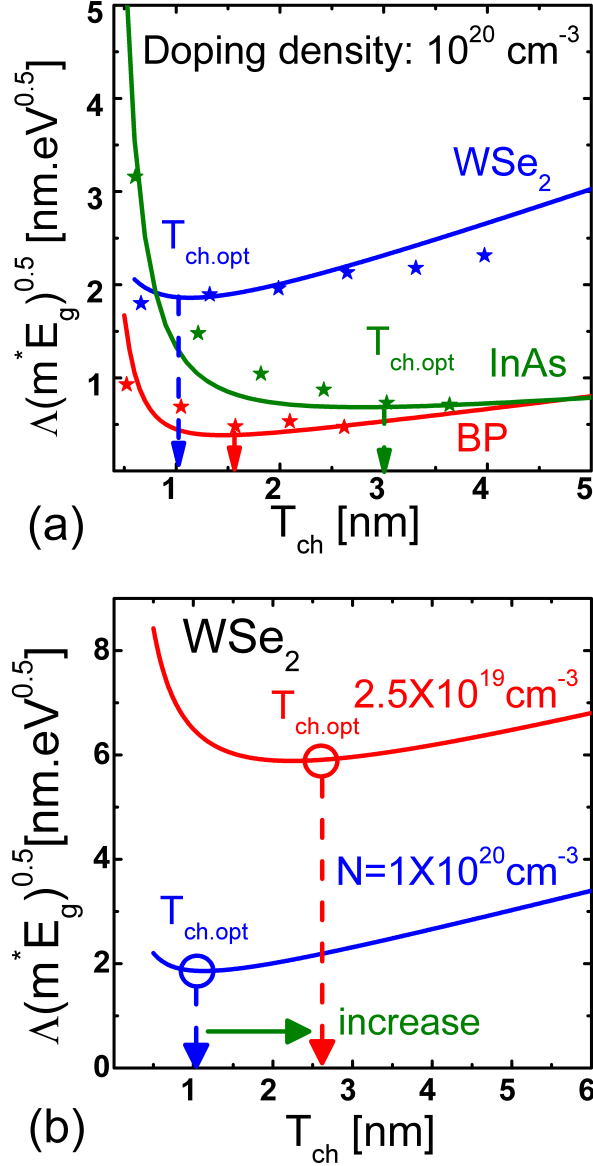
Fig. 2.8.: (a) $\Lambda\sqrt{m^*E_g}$ for WSe$_2$, BP, and InAs TFETs at a source doping density of $10^{20}cm^{-3}$. The solid lines are calculated from eq. (2.4) with parameters $c_0 \sim c_5$ as listed in Appendix III. The stars are extracted from atomistic quantum transport simulations. (b) $\Lambda\sqrt{m^*E_g}$ of WSe$_2$ TFETs for two different source doping densities calculated from eq. (2.4). $T_{ch.opt}$ increases as the doping density is reduced.

## 2.7 An upper limit of $T_{ch}$ defined by the OFF-state $(T_{ch.OFF})$

A thicker channel with a smaller bandgap may increase $I_{OFF}$ and deteriorate the ON/OFF current ratio. An upper limit on $T_{ch}$ can be deduced by considering the maximum permissible OFF current $(I_{OFF})$. Fig. 2.9(a), (b), and (c) show the $I_{OFF}$, $I_{ON}$, and ON/OFF current ratio extracted from the $I_D - V_G$ curves as calculated from atomistic quantum transport simulations. The supply voltage $(V_{DD})$ is 0.5V, and $I_{OFF}$ is chosen to be $10^{-3}\mu A/\mu m$ or the minimum possible current above this value if the leakage is high following the ITRS roadmap [6]. $I_{ON}$ is extracted at $V_G = V_D = 0.5V$ after shifting the $I_D - V_G$ curve to have $I_{OFF}$ at $V_G = 0V$. $I_{OFF}$ for BP and InAs is substantial when $T_{ch}$ is above 1 nm and 3 nm, respectively. This is because $E_g$ in this case is too small to block the tunneling current in the OFF-state as shown in the Fig. 2.9(d).

The ON/OFF current ratio suffers from significant degradation if the device cannot be turned off effectively as shown in Fig. 2.9(c). This would occur if $E_g < qV_{DS} + dE_{fp} + dE_{fn}$. $dE_{fp}$ and $dE_{fn}$ are the difference between the Fermi level and the band edge in the degenerately doped source and drain region, respectively. There exist a $T_{ch.OFF}$ below which $E_g$ is large enough to suppress the OFF current. Given that, $E_g = E_{g.bulk} + \dfrac{\alpha}{T_{ch}}$, $T_{ch.OFF}$ can be expressed as

$$T_{ch.OFF} < |\frac{\alpha}{qV_{DS} - E_{g.bulk} + dE_{fp} + dE_{fn}}| \tag{2.5}$$

$dE_{fn}$ and $dE_{fp}$ reduces as the doping density decreases, which results in a larger $T_{ch.OFF}$.

To optimize a TFET's ON/OFF current ratio, $T_{ch.opt}$ or $T_{ch.OFF}$ whichever is smaller should be used. Fig. 2.10 (a) and (b) show how $T_{ch.opt}$ and $T_{ch.OFF}$ for BP and InAs change as a function of the source doping density. Both $T_{ch.opt}$ and $T_{ch.OFF}$ increase as the source doping density is reduced.
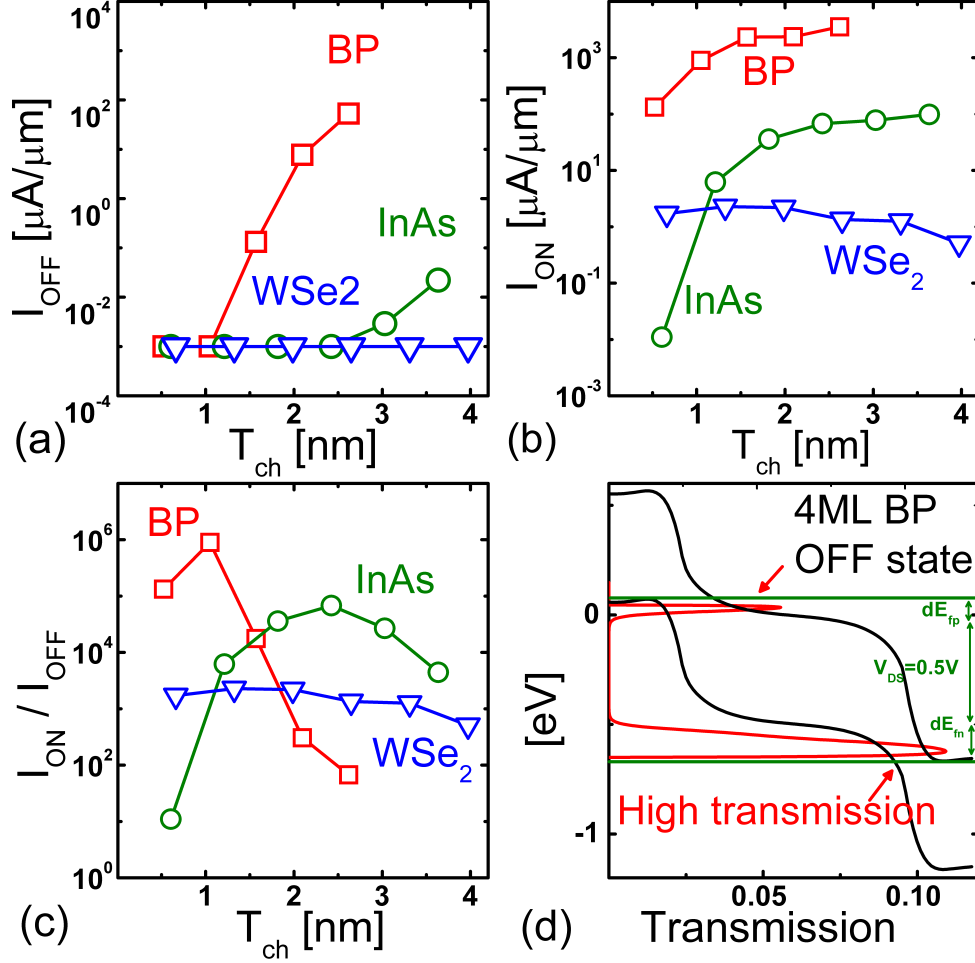
Fig. 2.9.: (a), (b), and (c) Dependence of $I_{OFF}$, $I_{ON}$, and the ON/OFF current ratio on $T_{ch}$. (d) OFF-state transmission for a BP 4ML TFET. A significant source to drain leakage in thick $T_{ch}$ BP (and InAs) TFETs is due to the small $E_g$.

## 2.8    Summary

Optimizing the channel thickness of a 2D TFET can significantly improve its performance. The choice of the channel thickness affects both the material properties and the electrostatics. There exists a channel thickness that minimizes the tunneling distance. However, the ON-state channel thickness ($T_{ch.opt}$) should optimize the product of the band gap, reduced effective mass and square of the tunneling distance. Interestingly, the mono-layer channels do not necessarily provide the optimum per-
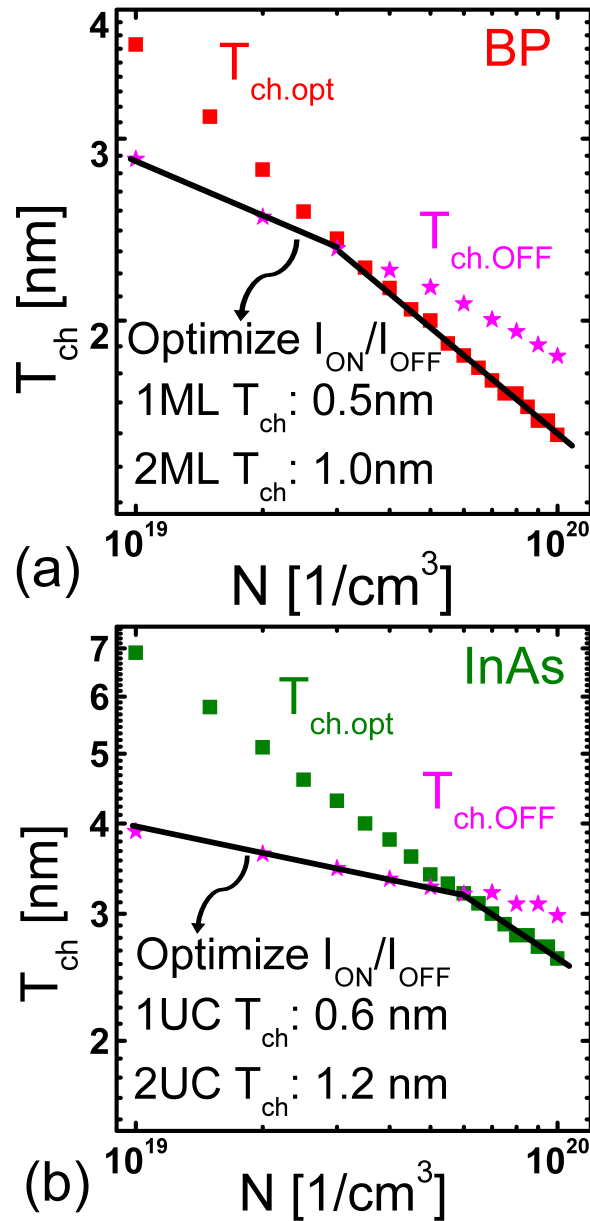
Fig. 2.10.: (a) and (b) $T_{ch.opt}$ and $T_{ch.OFF}$ for different source doping densities on a log-log scale. The channel thickness that optimizes the ON/OFF current ratio is $T_{ch.opt}$ or $T_{ch.OFF}$ whichever is smaller; $min(T_{ch.opt}, T_{ch.OFF})$. Note that $T_{ch.OFF}$ is obtained from atomistic quantum transport simulations for $V_{DS}$=0.5V. ML and UC are the abbreviations for mono-layer and unit cell.

formance despite of their excellent gate control. Moreover, a maximum permissible channel thickness $(T_{ch.OFF})$ is needed to reach acceptable OFF-currents. In this work, compact models were introduced to describe these two important channel thicknesses. A 2D TFET exhibits the highest ON/OFF current ratio when the channel thickness is chosen to be the smaller of $T_{ch.opt}$ and $T_{ch.OFF}$.

**Appendix I How descriptive is $I_{ON} \propto e^{-\Lambda\sqrt{m^*E_g}}$ ?**
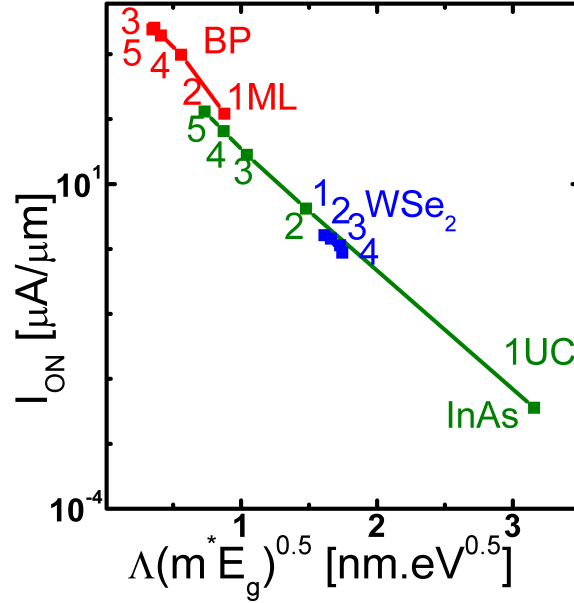


Fig. 2.11.: $I_{ON}$ and its corresponding $\Lambda\sqrt{m^*E_g}$ are extracted from atomistic simulations. $I_{ON}$ is proportional to $e^{-\Lambda\sqrt{m^*E_g}}$. ML and UC are the abbreviations for mono-layer and unit cell, respectively.

Knowing how descriptive is $I_{ON} \propto e^{-\Lambda\sqrt{m^*E_g}}$ compared to sophisticated quantum transport simulations is critical before optimizing $T_{ch}$ by minimizing $\Lambda\sqrt{m^*E_g}$. Fig. 2.11 shows $I_{ON}$ and its corresponding $\Lambda\sqrt{m^*E_g}$ from full band self consistent atomistic simulations.

This compact equation quantitatively represents the trend of sophisticated atomistic simulations, although it assumes a simple potential distribution and a simple

$m^*$ [40], different materials that have the same $\Lambda\sqrt{m^*E_g}$ are expected to provide $I_{ON}$ within the same order of magnitude. However, we found minor deviations between different materials because this compact equation approximates complex band structures by a single band reduced effective mass.

**Appendix II Simulation Details**

The numerical simulations are performed self-consistently by coupling quantum transmitting boundary method (QTBM) and 3D-Poisson equation [58]. 3D finite-difference method is used to calculate the carrier density ($\rho$). The anisotropic dielectric constant can be considered in the Poisson equation as shown in eq. (2.6) InAs has isotropic dielectric constants such that $\varepsilon_{in} = \varepsilon_{out} = 12$ [59]. BP and WSe$_2$ have an-isotropic dielectric constants such that $\varepsilon_{in}$ and $\varepsilon_{out}$ are not the same [60,61].

$$\frac{d}{dx}\left(\varepsilon_{in}\frac{dV}{dx}\right) + \frac{d}{dy}\left(\varepsilon_{in}\frac{dV}{dy}\right) + \frac{d}{dz}\left(\varepsilon_{out}\frac{dV}{dz}\right) = -\rho \qquad (2.6)$$

where $\varepsilon_{in}$ and $\varepsilon_{out}$ are the in-plane and out-of-plane dielectric constants. The value of $\varepsilon_{in}$ and $\varepsilon_{out}$ for the three channel materials are listed in TABLE 2.3.

The QTBM method is equivalent to the nonequilibrium Green's function approach without scattering but is more computationally efficient [51]. The open boundary Schr$\ddot{o}$dinder equation is solved in the following form:

$$(EI - H - \Sigma)\psi = S \qquad (2.7)$$

where $E$, $I$, $H$, and $\Sigma$ are energy, identity matrix, device Hamiltonian, and the total self-energy due to the open boundaries condition. $\psi$ and $S$ are the wave function in the device and the strengh of the carrier injection from contacts respectively. The Hamiltonian is constructed with the second nearest neighbor tight binding method. The simulation is performed by the Nanoelectronics Modeling tool: NEMO5. [62,63] More simulation details can be found in [23] and [64]. Since ballistic quantum transport is assumed, the indirect band to band tunneling and the trap-assisted tunneling

Table 2.3.: The $\varepsilon_{in}$ and $\varepsilon_{out}$ for WSe$_2$, BP, and InAs in the simulation. $\varepsilon_0 = 8.854 \times 10^{-12}$ C/(V.m).

| $\varepsilon_{in}/\varepsilon_{out}$ (unit: $\varepsilon_0$ ) | WSe$_2$ | BP | InAs |
|---|---|---|---|
| 1ML(1UC) | 4.5/2.9 | 4.2/1.4 | 12/12 |
| 2ML(2UC) | 6.3/4.3 | 6.2/1.5 | 12/12 |
| 3ML(3UC) | 7.2/5.1 | 7.5/1.8 | 12/12 |
| 4ML(4UC) | 8.0/5.8 | 8.1/2.0 | 12/12 |
| 5ML(5UC) | 8.5/6.2 | 8.8/2.3 | 12/12 |
| 6ML(6UC) | 9.0/6.5 | | 12/12 |

are not considered. However, the indirect tunneling will mostly influence multilayer WSe$_2$ TFETs. It will not affect the results for the direct band gap materials significantly [65].

### Appendix III Analytical expression for $\Lambda\sqrt{m^*E_g}$

$\Lambda\sqrt{m^*E_g}$ can be expressed as a function of $T_{ch}$ as

$$\Lambda\sqrt{m^*E_g} = (\lambda + W_D)\sqrt{m^*E_g} \tag{2.8}$$

$$= \left(c_0 T_{ch} + c_1 + c_2\frac{1}{T_{ch}} + c_3\frac{1}{T_{ch}^2}\right) c_4\sqrt{1 + c5\frac{1}{T_{ch}}} \tag{2.9}$$

where $c_0 \sim c_5$ are obtained after expressing $\lambda$, $W_D$, $m^*$, and $E_g$ as a function of $T_{ch}$. The dependence of $m^*$ and $E_g$ on $T_{ch}$ has been discussed in Section II.

$W_D$ for a 2D PN-junction is given by

$$W_D = \frac{\pi\varepsilon\Delta V}{ln(4)qNT_{ch}} \tag{2.10}$$

$$\sim \frac{\pi\varepsilon E_g}{ln(4)qNT_{ch}} \tag{2.11}$$

$$\sim \frac{\pi (e_1 T_{ch} + e_2)\left(E_{g.bulk} + \dfrac{\alpha}{T_{ch}}\right)}{ln(4)qNT_{ch}} \tag{2.12}$$

which can be expressed as a function of $T_{ch}$ explicitly. $\Delta V$ is of the order of $E_g$ which can be expressed as $E_g = E_{g.bulk} + \dfrac{\alpha}{T_{ch}}$. $\varepsilon$ is assumed as a homogeneous dielectric constant for simplicity, which is estimated as a weighted average based on the semiconductor ($\varepsilon_r = 5 \sim 15$) and the surrounding spacer (air; $\varepsilon_r = 1$). $\varepsilon$ increases with $T_{ch}$ due to the changes in the electrostatic environment and can be expressed as $\varepsilon \sim e_1 T_{ch} + e_2$. In this work, $e_1$ and $e_2$ are obtained by fitting $W_D$ shown in Fig. 2.7(a), (b), and (c). $e_1$ and $e_2$ for the three studied materials are listed in TABLE 2.4. $e_1$ has the unit of $\varepsilon_0/nm$ and $e_2$ has the unit of $\varepsilon_0$.

The chemically doped TFET's scaling length ($\lambda$) is given by

$$\lambda = \frac{\varepsilon}{\pi\varepsilon_{ox}}\left[\gamma_1 T_{ch} + \gamma_2 T_{ox}\right] \tag{2.13}$$

$$= L_1 T_{ch} + L_2. \tag{2.14}$$

Table 2.4.: Parameters $e_1$ and $e_2$ for WSe$_2$, BP, and InAs's $\varepsilon$ $(= e_1 T_{ch} + e_2)$. $\varepsilon_0 = 8.854 \times 10^{-12}$ C/(V.m).

| channel | $e_1$ $[\varepsilon_0/nm]$ | $e_2$ $[\varepsilon_0]$ |
|---------|------|------|
| WSe$_2$ | 0.43 | 0.99 |
| BP      | 0.62 | 0.91 |
| InAs    | 0.83 | 1.28 |

which is a modified version of the electrically doped TFETs' $\lambda$ [28,57]. $L_1$ and $L_2$ can be obtained by fitting $\lambda$ shown in Fig. 2.7 (a), (b), and (c). $L_1$ and $L_2$ for the three studied materials are listed in TABLE 2.5.

Table 2.5.: Parameters $L_1$ and $L_2$ for WSe$_2$, BP, and InAs.

| channel | $L_1$ [cons.] | $L_2$ [nm] |
|---------|---------------|------------|
| WSe$_2$ | 0.7 | 0.12 |
| BP | 1.13 | -0.46 |
| InAs | 0.94 | 0.35 |

After substituting $W_D$, $\lambda$, $E_g$, and $m^*$, $\Lambda\sqrt{m^*E_g}$ can be rearranged as

$$\Lambda\sqrt{m^*E_g} = (\lambda + W_D)\sqrt{m^*E_g}$$

$$= \left( L_1 T_{ch} + L_2 + \frac{\pi\left(e_1 T_{ch} + e_2\right)\left(E_{g.bulk} + \dfrac{\alpha}{T_{ch}}\right)}{ln(4)qNT_{ch}} \right)$$

$$\sqrt{m^*\left(E_{g.bulk} + \frac{\alpha}{T_{ch}}\right)}$$

$$= \left( c_0 T_{ch} + c_1 + c_2\frac{1}{T_{ch}} + c_3\frac{1}{T_{ch}^2} \right) c_4\sqrt{1 + c5\frac{1}{T_{ch}}} \qquad (2.15)$$

where $c_1$ to $c_5$ are

$$c_0 = L_1 \tag{2.16}$$

$$c_1 = L_2 + \beta_1 E_{g.bulk} \tag{2.17}$$

$$c_2 = \beta_2 E_{g.bulk} + \beta_1 \alpha \tag{2.18}$$

$$c_3 = \beta_2 \alpha \tag{2.19}$$

$$c_4 = \sqrt{m^* E_{g.bulk}} \tag{2.20}$$

$$c_5 = \frac{\alpha}{E_{g.bulk}} \tag{2.21}$$

$$\beta_1 = \frac{\pi e_1}{ln(4)qN} \tag{2.22}$$

$$\beta_2 = \frac{\pi e_2}{ln(4)qN} \tag{2.23}$$

$c_1$ to $c_5$ for the three channel materials are listed in the Table 2.6.

Table 2.6.: Parameters $c_1$ to $c_5$ for $WSe_2$, BP, and InAs.

| channel | $c_0$ | $c_1$ | $c_2$ | $c_3$ | $c_4$ | $c_5$ | $\beta 1$ | $\beta 2$ |
|---------|-------|-------|-------|-------|-------|-------|-----------|-----------|
| $WSe_2$ | 0.7 | 1.78 | 0.85 | 0.01 | 0.554 | 0.01 | 1.24 | 0.54 |
| BP | 1.14 | -0.24 | 0.71 | 0.57 | 0.12 | 1.79 | 0.78 | 1.14 |
| InAs | 0.94 | 0.91 | 2.77 | 1.56 | 0.09 | 4.28 | 1.60 | 1.04 |

The same methodology can also be used to calculate the optimum $T_{ch}$ for electrically doped TFETs (ED-TFETs). The tunneling distance $\Lambda$ of an ED-TFET consist of two scaling lengths ($\lambda$) beneath the electrostatic gates and the spacing between two electrostatic gates [28, 57].

**Appendix IV the subthreshold swing (SS)**

Fig. 2.12 shows the subthreshold swing (SS) extracted at the OFF current $(10^{-3}\mu A/\mu m)$. SS has a similar dependence on the channel thickness to $I_{ON}$ .
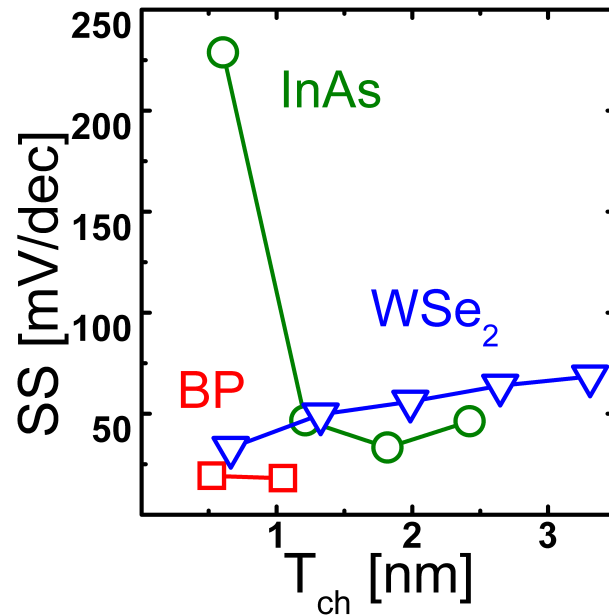


Fig. 2.12.: SS for BP, InAs, and WSe$_2$ TFETs at the OFF current $(10^{-3}\mu A/\mu m)$.

**Appendix V Current extracted at SS = 60mV/dec**

Current extracted at SS = 60mV/dec $(I_{60})$ is a figure of merit to compare different steep transistors and their ability to scale down the supply voltage [66]. Fig. 2.13 shows $I_{60}$ for BP, InAs, and WSe$_2$ TFETs. $I_{60}$ of BP TFETs is significantly higher than the other TFETs.
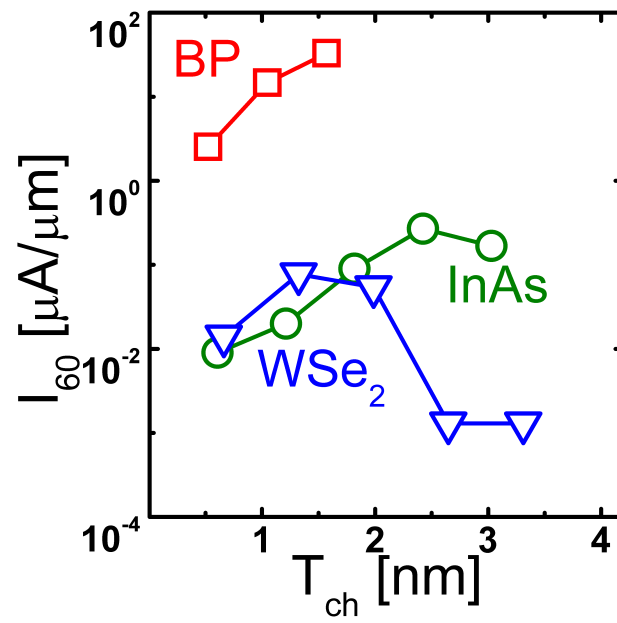
Fig. 2.13.: $I_{60}$ for BP, InAs, and WSe$_2$ TFETs.

# 3. IMPACT OF BODY THICKNESS AND SCATTERING ON III-V TRIPLE HETEROJUNCTION DOUBLE-GATED TFET MODELED WITH ATOMISTIC MODE-SPACE APPROXIMATION

## 3.1    Abstract

The triple heterojunction TFET has been originally proposed to resolve TFET's low ON-current challenge. The carrier transport in such devices is complicated due to the presence of quantum wells and strong scattering. Hence, the full band atomistic NEGF approach, including scattering, is required to model the carrier transport accurately. However, such simulations for devices with realistic dimensions are computationally unfeasible. To mitigate this issue, we have employed the empirical tight-binding mode space approximation to simulate triple heterojunction TFETs with the body thickness up to 12 nm. The triple heterojunction TFET design is optimized using the model to achieve a sub-60mV/dec transfer characteristic under realistic scattering conditions.

## 3.2 Introduction

The triple heterojunction TFET has been proposed to increase the ON-current by forming two quantum wells in the tunnel junction to decrease tunneling distance and introduce resonant-enhanced tunneling [31, 32].

The carrier transport in such devices depends on three factors: 1) the interaction between confined states in quantum wells and propagating states in conduction and valence bands, 2) the BTBT process of confined states in quantum wells, and 3) the scattering effects that thermalize carriers within the quantum well [67, 68]. Therefore, the accurate atomistic quantum transport simulation, including scattering mechanisms, is the fundamental approach to model such devices [69–71]. The quantum transport simulation is usually conducted by quantum transmitting boundary method (QTBM) [72, 73] or non-equilibrium Green's function (NEGF) [74, 75] using the recursive Green's function (RGF) algorithm [76].

Both methods are capable of capturing the quantum mechanical effects in nanodevices. However, QTBM cannot capture inelastic scattering. Fig. 3.1 (a) shows the schematics of QTBM and RGF. For QTBM, one has to compute the wave functions of an open system. The wave functions are obtained as solutions of the linear system with the size equal to the Hamiltonian matrix dimension. The method is numerically efficient because it computes only a few wave functions per energy, namely, for the states of particles that are injected into the device from the propagating modes in the leads [72, 73]. Since the method is based on the wave function formalism, it cannot describe incoherent processes such as inelastic scattering. For RGF, the device is partitioned into thin slabs, and its Green's function is solved recursively. Since the calculation of Green's function requires matrix inversion, RGF is usually slower than QTBM. However, since RGF is capable of including scattering mechanisms, in this work, RGF is chosen to study the triple heterojunction TFET.

The computation cost of RGF is $O(N^3 N_s)$ where $N_s$ is the number of the slab in the device, and $N$ is the matrix size of each slab. $N$ is proportional to the number of
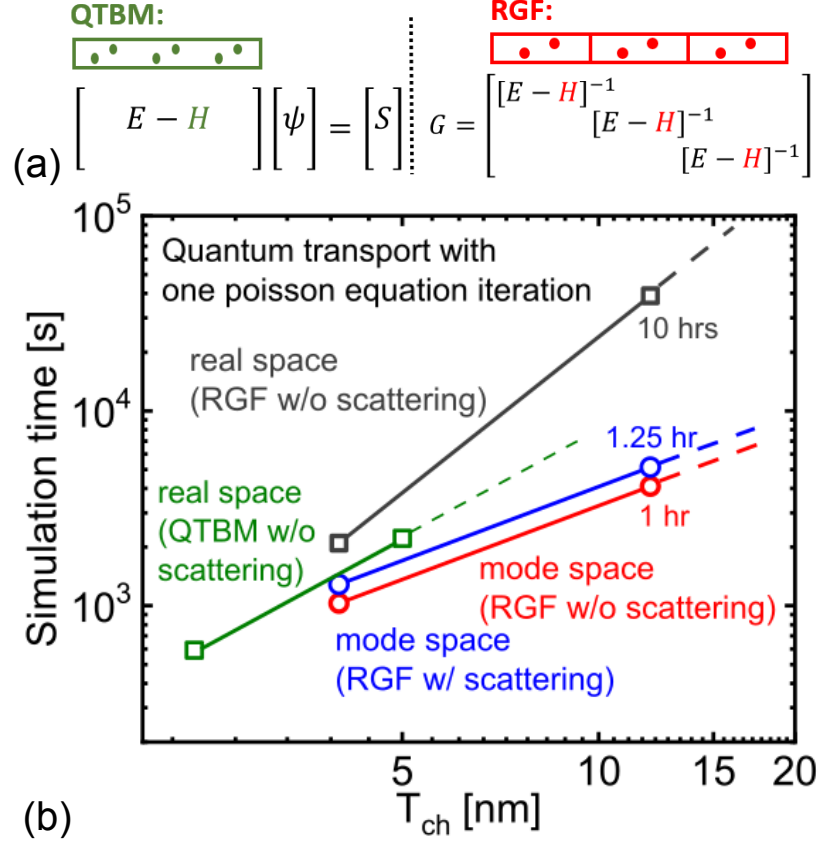
Fig. 3.1.: (a) The time-consuming part of the two quantum transport algorithms: QTBM and RGF. $H$ and $E$ are the Hamiltonian and energy. $\psi$ and $S$ are the wave function and the strength of the carrier injection from contacts. (b) The quantum transport simulation time for different body thicknesses using the empirical tight-binding basis in the real space and the mode space. The simulations are performed in Nanoelectronics Modeling tool NEMO5 [62, 63] by 36 Intel Xeon Gold "Sky Lake" processors.

atoms per slab times the number of the orbitals per atom [32]. Since the number of the atoms grows with the device dimension, the computation becomes too expensive for the realistic body thicknesses (i.e. $> 8$ nm) [11, 34–38, 77, 78]. Fig. 3.1 (b) shows how the simulation time of an ultra-thin body (UTB) TFET grows with body thickness. RGF simulation time for 12 nm thick devices using the empirical tight-

binding $sp^3d^5s^*$ basis in real space is 10 hours per Poisson equation iteration. 1000 hours are needed to obtain the transfer characteristic of a transistor, considering the number of required iterations and bias points, which is prohibitively time-consuming for device optimization.

The mode-space (MS) approximation [32, 79] that compresses the basis to reduce the simulation time becomes necessary to enable device research for the body thickness exceeding 10 nm. With the MS approximation, the RGF simulation time for a 12 nm thick device is reduced to one hour, which allows studying the device characteristics in detail.

Previously, the MS approximation has been used to simulate nanowire MOSFETs and homojunction UTB TFETs [32, 80]. In this work, we expand the method to simulate UTB heterojunction TFETs. To describe the scattering of carriers in quantum wells, an efficient thermalization model, that showed to match experimental data, has been incorporated into the MS approximation [69, 70]. The simulation time of a device with 12 nm body thickness increases by 25% if the scattering is included, which is practically acceptable.

This chapter is divided into four sections. In section II, we present the transferable transformation matrix for different transverse wave vectors in UTB applications. In section III, the working principle of the triple heterojunction TFET is discussed. The full empirical tight-binding basis in real space and the mode space are benchmarked for transfer characteristics and local density of states (LDOS). In section IV and V, the performance of the triple heterojunction TFETs with a body thickness of 12 nm is evaluated in the ballistic limit, and the impact of scattering is analyzed.

## 3.3  Transferable transformation matrix

For the MS approximation, the Hamiltonian size is reduced by the transformation:

$$h(k_\parallel)_{n \times n} = U^T_{n \times N} H(k_\parallel)_{N \times N} U_{N \times n} \qquad (3.1)$$

where $H$ is full basis Hamiltonian constructed by the empirical tight-binding (ETB) method and $h$ is the reduced-size mode-space Hamiltonian capturing the modes near the band edges, which contribute significantly to electronic transport. The accuracy of the sub-bands far from the band edges is sacrificed to reduce the representation such that $n$ is significantly smaller than $N$ [32, 79]. $U$ is the transformation matrix generated by the mode-space algorithm by optimizing the modes near the band edges [79]. Our numerical experiments showed that the original algorithm proposed by Mil'nikov [79] could not remove the unphysical bands in all cases. To minimize the trial-and-error effort, a robust scheme that reliably removes all the unphysical bands has been developed [32] and is employed in this work.

The electronic transport in a UTB system requires sampling multiple transverse wave vectors ($k_\parallel$) along the periodic direction. Traditionally, the reduced-size Hamiltonians at each sampled $k_\parallel$ are supposed to be generated by different transformation matrices because the modes contributing to electronic transport are different for different $k_\parallel$. However, generating the transformation matrix for each sampled $k_\parallel$ is a time-consuming process due to the basis optimization [70, 79]. In this work, we find out that generating the transformation matrix for each sampled $k_\parallel$ is not necessary since the matrix is transferable within a sizable range of $k_\parallel$.

Fig. 3.2(a) is the electronic structures of a 4 nm InAs UTB grown along the [100] direction and confined along the [011] direction. The transformation matrix is generated for $k_\parallel = 0.025 \frac{2\pi}{a_0}$. It can be used to reduce the basis size while capturing the modes near the band edges for $k_\parallel$ in the range $(0, 0.05) \frac{2\pi}{a_0}$. However, for $k_\parallel$ that is larger than $0.05 \frac{2\pi}{a_0}$, it can not capture the modes near the band edges since the modes are too different from those of $k_\parallel = 0.025 \frac{2\pi}{a_0}$. The transformation matrix generated for $k_\parallel = 0.025 \frac{2\pi}{a_0}$ works for the range $(0, 0.05) \frac{2\pi}{a_0}$. Considering these facts, one can divide the whole $k_\parallel$ space into several segments with the size of $0.05 \frac{2\pi}{a_0}$ and use the same transformation matrix to generate the reduced-size Hamiltonian within each segment. This feature is critical for applying the MS approximation in a UTB system because it avoids the efforts to generate redundant transformation matrices.

**Un-strained**



**3.4% bi-axial compress strain**
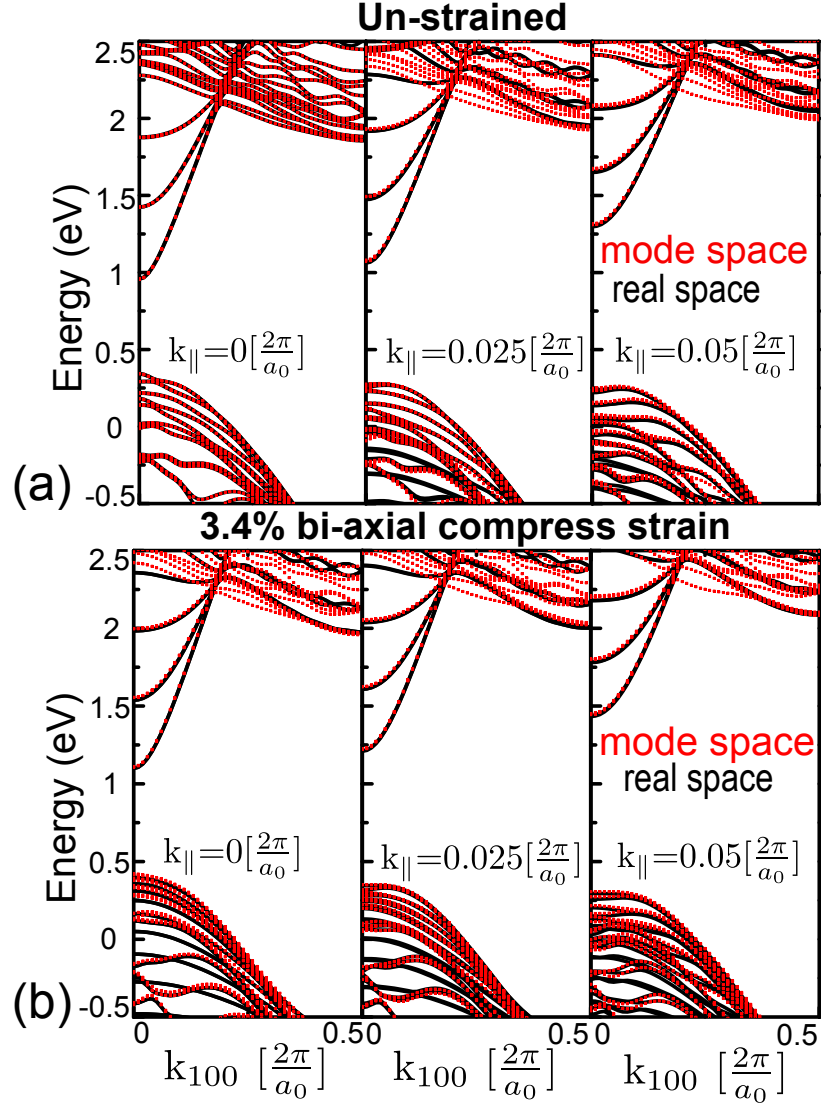


Fig. 3.2.: Electronic band structure for a 4 nm InAs UTB computed using both empirical tight-binding basis in the real space and the mode space with (a) zero strain and (b) 3.4% bi-axial compressive strain. The zero strain transformation matrix generated at $k_{\parallel} = 0.025\ \frac{2\pi}{a_0}$ is used to obtain the above mode space basis. The basis reduction ratio ($n/N$) is 178/800.

In this work, the strained InAs layer is utilized in the triple heterojunction desgin. We found the transformation matrix for InAs is transferable both for different $k_{\parallel}$ and for different strain conditions as shown in Fig. 3.2 and Fig. 3.3. For heterojunction

devices, the strain is a critical and inherent factor that affects material properties such as the effective mass and the bandgap. Fig. 3.2 (b) shows the electronic structure of a 4 nm InAs UTB with 3.4 % bi-axial compressive strain, which will be used in the triple heterojunction TFET studied later in this work. In Fig. 3.2(b), the same transformation matrix has been used as the one in Fig. 3.2(a).

Fig. 3.3 shows the electronic structures for 4 nm thick InAs UTBs under different bi-axial compressive strain. The mode-space basis electronic structures in Fig. 3.3 for different strain values are generated by the zero-strain transformation matrix. The transformation matrix is transferable for different strain values from zero to 3.4% within the basis optimization energy window. Since the transformation matrix is transferable for different strains, one can easily use MS approximation for devices with different strain conditions.

## 3.4   Method validation

In this section, the MS approximation is validated for the $In_{0.53}Ga_{0.47}As$ homojunction (homo-) and the triple heterojunction (hetero-) TFETs. The double-gate UTB schematics are shown in Fig. 4.1 (a). The body thickness of 4 nm is chosen since using the full basis to simulate a complete I-V curve is computationally expensive as the body thickness increases further. The triple heterojunction TFET design consists of a P-doped $In_{0.53}Ga_{0.47}As$ and $GaAs_{0.5}Sb_{0.5}$ source with $N_a = 5 \times 10^{19}\ cm^{-3}$, an intrinsic InAs and InP channel, and an N-doped InP drain with $N_d = 2 \times 10^{19}$ $cm^{-3}$. The confinement direction is along the [011] direction, and the transport direction is along the [100] direction. The crystal growth direction is along the transport direction to simulate the vertical Fin-TFET structure [36]. The substrate is assumed to be InP such that InAs is under 3.41% bi-axial compressive strain while the rest of the materials are not under strain. The gate dielectric is a 3.2 nm thick $ZrO_2$ with the relative dielectric constant of 15. The source to drain bias ($V_{DS}$) is 0.3 V.

$$k_\| = 0.025 \left[\tfrac{2\pi}{a_0}\right]$$
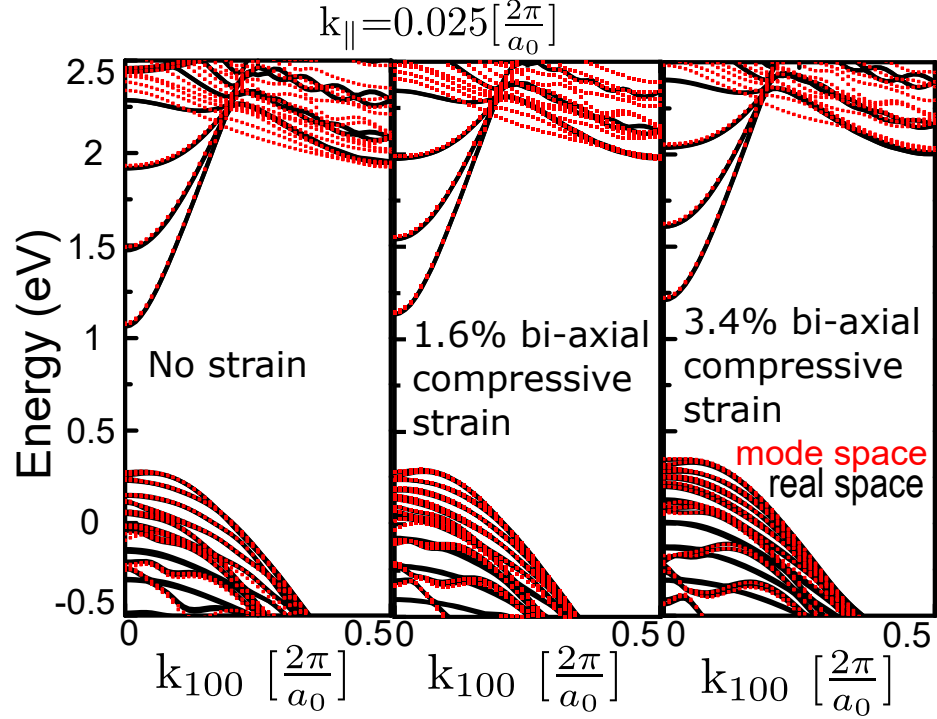
Fig. 3.3.: Electronic band structure for a 4 nm InAs UTB computed using the empirical tight-binding basis in the real space and the mode space with (a) zero-strain, (b) 1.6 %, and (c) 3.4 % bi-axial compressive strain. The zero strain transformation matrix is used to obtain the mode-space basis.

In order to model the electric field in the device, the Poisson equation is solved on a domain that includes source, drain, channel, and oxide. The oxide is assumed to be a perfect insulator, so the electron transport equations are not solved in the oxide area. The Ohmic contact model is assumed for the source and drain contacts, so the normal electric field component is set to zero at the corresponding device boundaries. The applied voltages at the source/drain contacts define the Fermi level for electrons in the source/drain leads, respectively. For the gate contact, the Schottky-Mott model is used, so a constant potential value is set at the gate metal/oxide interface. Such boundary conditions for the Poisson equation allow getting convergent results for the relevant applied bias range for both ballistic simulations and simulations with scattering.
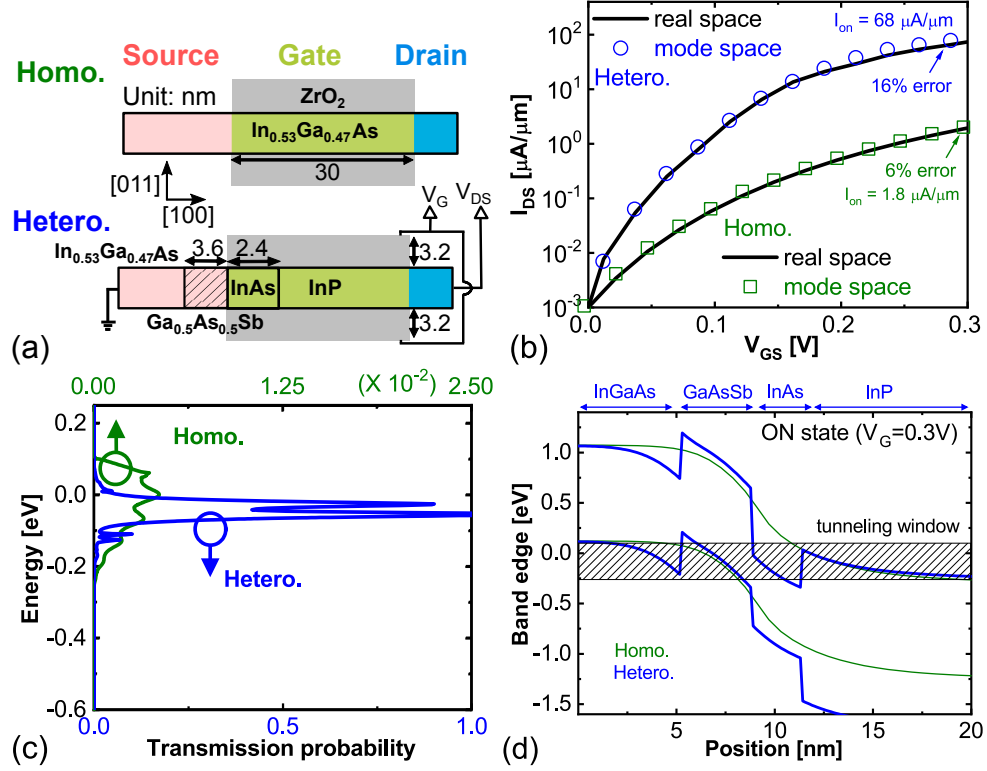
Fig. 3.4.: (a) Device schematics, (b) transfer IV characteristic, (c) transmission probability at $V_{GS} = 0.3$ V, and (d) band diagram at $V_{GS} = 0.3$ V of double-gate InGaAs homojunction and triple heterojunction TFET with 4 nm body thickness. The transfer IV characteristic is computed using the empirical tight-binding basis in both the real space and the mode space.

The InGaAs homojunction and triple heterojunction TFET's transfer IV characteristic ($I_{DS}$-$V_{GS}$) are shown in Fig. 4.1 (b). The IV curves are shifted to have a fixed OFF-current value of $10^{-3}$ $\mu A/\mu m$ at $V_{GS} = 0$ V. The current obtained from the MS approximation agrees with the current calculated by the full ETB basis. The error introduced by the MS approximation is quantified through the expression $\Delta I_{err} = |I_{full} - I_{MS}|/I_{full}$. At the ON-state, where $V_G = 0.3$ V, the triple heterojunction TFET's $\Delta I_{err}$ is 16%, which is slightly higher than the InGaAs homojunciton TFET's $\Delta I_{err}$ which is 6%. The higher error in the heterojunction case is expected

due to the presence of junction interfaces, and more transformation matrices are used (one for each material).

The ON-current ($I_{ON}$) of the triple heterojunction TFET is 68 $\mu A/\mu m$, which is much higher than the InGaAs homojunction TFET's $I_{ON}$ 1.8 $\mu A/\mu m$. The reason is that the triple heterojunction TFET's tunneling distance is smaller than the In-GaAs homojunction TFET's tunneling distance due to the staggered-heterojunction (GaAsSb/InAs) used in BTBT tunneling region as shown in Fig. 4.1 (d). Since In-GaAs and InP are present in the source and the channel, two quantum wells are formed in the tunneling junction. The quantum well states introduce resonant-enhanced tunneling that boosts the transmission probability close to 1, as shown in Fig. 4.1 (c).

To gain a better understanding of the MS approximation, the local density of states (LDOS) of the InGaAs homojunction and triple heterojunction TFET at the ON-state ($V_{GS}$= 0.3 V) are shown in Fig. 3.5. In (a) and (b), the InGaAs homojunction TFET's LDOS computed from the real space and the mode space are almost the same. While in (c) and (d), the triple heterojunction TFET's LDOS computed from the real space and mode space has some differences. Aside from the aligned resonant states that introduce the resonant-enhanced tunneling, some extra un-physical states at the heterojunction interfaces are visible in the LDOS computed by the mode space. The resonant states and the un-physical states are marked with black dashed circles.

The coupling Hamiltonian block at the heterojunction interface is not the same as the interior Hamiltonian blocks. In this work, the mode-space Hamiltonian at the heterojunction interface is generated using two different transformation matrices. For example, the mode-space Hamiltonian block at GaAsSb/InAs interface ($h_{\mathrm{GaAsSb/InAs}}$) is generated by the following transformation:

$$h_{\mathrm{GaAsSb/InAs}} = U^T_{\mathrm{GaAsSb}} \cdot H_{\mathrm{GaAsSb/InAs}} \cdot U_{\mathrm{InAs}} \tag{3.2}$$

where $U_{\mathrm{GaAsSb}}$ and $U_{\mathrm{InAs}}$ are the transformation matrices for GaAsSb and InAs, $H_{\mathrm{GaAsSb/InAs}}$ and $h_{\mathrm{GaAsSb/InAs}}$ are the full basis and the mode-space Hamiltonian block at GaAsSb/InAs interface. Since the mode-space approach is based on the band structure of periodic blocks, the non-periodic junction interface requires this special
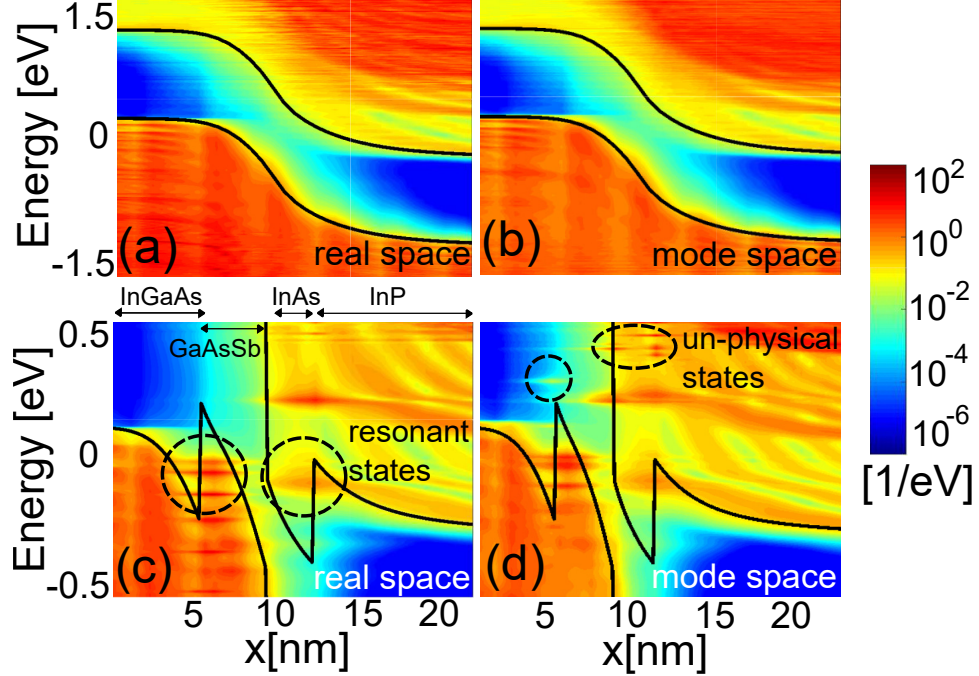
Fig. 3.5.: LDOS of (a),(b) the InGaAs homojunction TFET and (c),(d) the triple heterojunction TFET at the ON-state ($V_{GS} = 0.3$ V) along the channel computed using the empirical tight-binding basis in both the real space and the mode space.

treatment. Therefore, unphysical states at the heterojunction interfaces may appear in the mode-space approximation.

The material interface needs extra attention in the MS approximation since the coupling Hamiltonian at the interface is multiplied with the transformation matrices of both materials. That's why we see the un-physical localized states near the interfaces. These un-physical localized states are part of the reason why the triple heterojunction TFET's $\Delta I_{err}$ is higher than the InGaAs homojunction TFET's $\Delta I_{err}$.

The energy window of the MS basis for materials used in the tunneling junction (GaAsSb and InAs) should be increased to reduce triple heterojunction TFET's $\Delta I_{err}$. Fig. 3.6 shows the basis optimization with different energy windows for the 4 nm GaAsSb UTB used in the triple heterojunction TFET. GaAsSb basis #1 has the energy window that covers the valence band ($\Delta E_V$) for 100 meV, which is used

to obtain the results shown previously in Fig. 4.1. GaAsSb basis #2's $\Delta E_V$ is 500 meV, which is larger than the quantum well depth of 420 meV in the triple heterojunction TFET. When GaAsSb basis #1 is replaced with GaAsSb basis #2, the error is reduced from 16 % to 6%. Since the accuracy of the confined states is critical to electronic transport in the triple heterojunction TFET, the MS approximation for such applications requires a large enough energy window, which covers the depth of the quantum well.
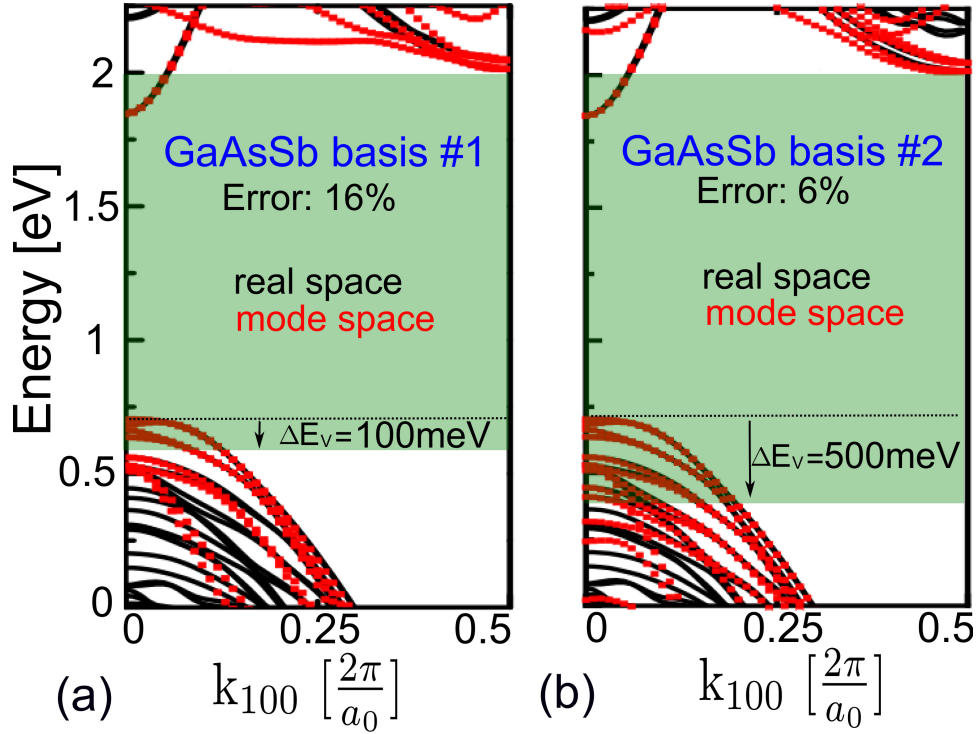


Fig. 3.6.: Electronic structure of a 4 nm GaAsSb UTB with the energy window that covers the valence band ($\Delta E_V$) with (a) 100 meV and (b) 500 meV. The shading shows the energy window used for the bases optimization. The basis reduction ratios (n/N) are (a) 125/800 and (b) 200/800.

## 3.5   12 nm body thickness triple heterojunction TFETs

The reported triple heterojunction TFET designs in the references [31, 32] were optimized for the body thickness of 4 nm due to the computational limits. However, devices with such a thin body are difficult to be realized in experiments. With the MS approximation, we can increase the simulated body thickness to 12 nm, which is the thinnest possible body thickness for III-V materials Fin-TFET structure [38].
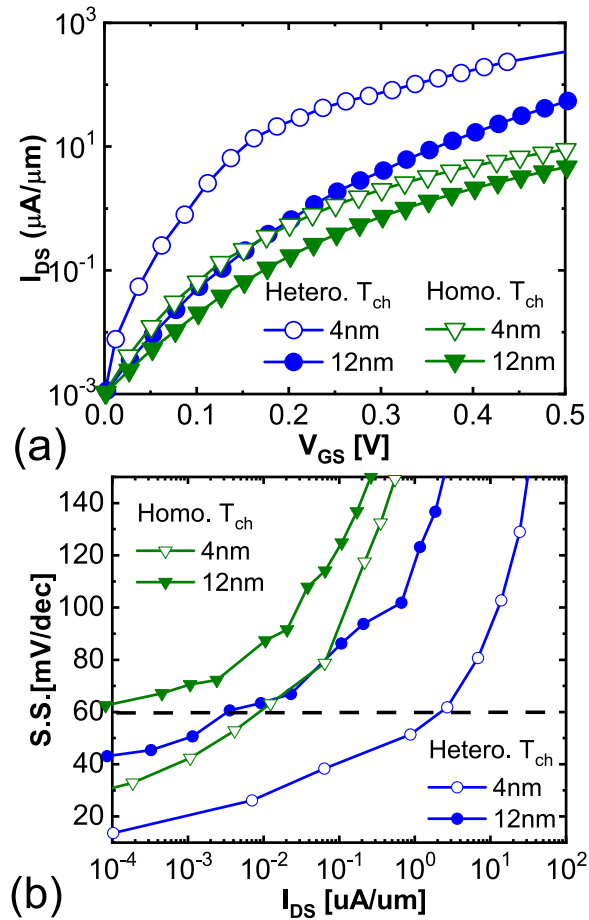


Fig. 3.7.: (a) Transfer IV characteristic and (b) sub-threshold swing (S.S.) for InGaAs homojunction and triple heterojunction TFET with the body thickness ($T_{ch}$) of 4 nm and 12 nm.

The transfer characteristics and the extracted sub-threshold swing (S.S.) of the triple heterojunction TFET with the body thickness of 12 nm are shown in Fig. 3.7 (a) and (b). The InGaAs homojunction TFET's simulation results are also displayed as a reference. When the body thickness increases, the triple heterojunction TFET's $I_{ON}$ decreases significantly while the InGaAs homojunction TFET's $I_{ON}$ does not. Nevertheless, the triple heterojunction TFET's sub-threshold swing retains sub-60mV/dec which is still better than the InGaAs homojunction TFET.

The triple heterojunction TFET's $I_{ON}$ depends on the alignment of the resonant states in the quantum wells. Table. 3.1 summarizes $I_{ON}$ of the InGaAs homojunction and triple heterojunction TFET with 12 nm body thickness at $V_{GS} = 0.3$ V and 0.5 V. For the InGaAs homojunction TFET, $I_{ON}$ at $V_{GS} = 0.3$ V or 0.5 V are of the same order. The impact of the gate bias is limited due to the weak gate control and, consequently, a large scaling length [64, 77]. In contract with the InGaAs homojunction TFET, the triple heterojunction TFET has the resonant enhanced tunneling that compensates the enlarged tunneling distance due to the loose gate control. Once $V_{GS}$ is large enough to achieve the resonant enhanced tunneling condition, $I_{ON}$ increases from 3.9 $\mu$A/$\mu$m to 50 $\mu$A/$\mu$m. Fig. 3.8 (a) and (b) show the LDOS of the triple heterojunction TFET with 12 nm body thickness computed at $V_{GS} = 0.3$ and 0.5 V.
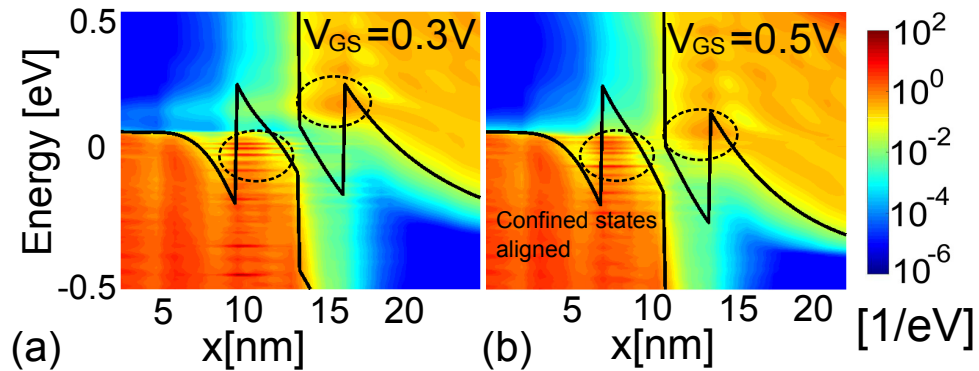


Fig. 3.8.: LDOS along the channel of triple heterojunction TFET with a body thickness of 12 nm at (a) $V_{GS} = 0.3$ V and (b) $V_{GS} = 0.5$ V. The quasi-bound states of the quantum states are indicated by the dashed lines.

Table 3.1.: The $I_{ON}$ for InGaAs homojunction (Homo.) and triple heterojunction (Hetero.) TFETs.

| $I_{ON}$ $[\mu A/\mu m]$ | | | | |
|---|---|---|---|---|
| $V_{GS}$ | Homo. | Hetero. | Hetero. | ref. [13] |
| $[\mu A/\mu m]$ | (12nm) | (12 nm) | (4 nm) | |
| 0.3 V | 0.7 | 3.9 | 68 | 10 |
| 0.5 V | 4 | 50 | 335 | 92 |

For $V_{GS} = 0.5$ V, the two resonant states are aligned to achieve the resonant enhanced tunneling condition such that the $I_{ON}$ increases up to 50 $\mu$A/$\mu$m.

In Table. 3.1, $I_{ON}$ of the InGaAs homojunction TFET and the triple heterojunction TFETs are listed. The 4 nm triple heterojunction TFET has an exceptional $I_{ON}$ of 335 $\mu$A/$\mu$m. While for the 12 nm thick triple heterojunction TFET, $I_{ON}$ decreases to 50 $\mu$A/$\mu$m, which is similar to the published III-V heterojunction nanowire TFET experimental results with similar dimensions [13].

## 3.6  Efficient scattering model

The strong scattering and thermalization in the highly doped source and drain regions have a significant impact on the transport properties of tunneling devices [67,81–86]. Different mechanisms such as electron-electron scattering [87,88], electron-phonon scattering, electron-ion scattering, plasmon scattering, etc. contribute to the strong scattering and thermal ionization. Including all of these scattering mechanism, especially electron-electron scattering, into RGF is computationally unfeasible for realistic devices. Hence, an effective carrier thermalization method is needed. An effective thermalization approach for tunneling devices has been developed for
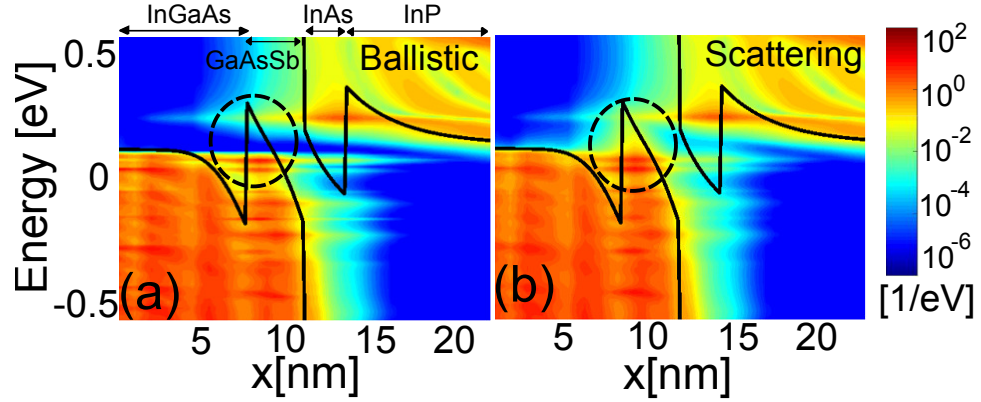
Fig. 3.9.: LDOS for the triple heterojunction TFET with 4 nm body thickness at the OFF-state (a) with and (b) without scattering effects. The dashed line marks a quantum well region filled by electrons due to the scattering.

resonant-enhanced tunneling diodes [81] and has been shown to match experimental data on Nitride tunneling devices for a wide range of bias conditions [69]. In this work, a combination of the mode-space approximation and the thermalization approach is used to include thermalization into atomistic simulation of devices with large and realistic dimensions.

Thermalization of carriers in source and drain contacts, has two main impacts which significantly distort the transport properties: 1) filling quantum well states near the source region, 2) widening the resonance energies inside the well. Including scattering accurately is crucial, since the states in the quantum well contribute to a significant part of the channel leakage.

In this work, the effective scattering rate in the source and the drain is estimated from the mobility, that empirically represents the strength of the scattering. Since the mobility ($\mu$) of the highly doped III-V materials ranges from $10^2$ to $10^3$ $cm^2/(V.s)$ [89–91] with the effective mass ($m^*$) of $0.001 \sim 0.01$, the reasonable energy broadening ($\eta \sim \frac{q\hbar}{2m^*\mu}$) is about $1 \sim 10$ meV. In this work, the broadening factor of 10 meV is used to explore the worst-case scenario [69]. The momentum relaxation time is 32 fs ($\tau = \frac{\hbar}{2\eta}$).

For triple heterojunction TFET, the quantum well states in the tunneling junction contribute to the OFF-state leakage current. The OFF-state LDOS of the triple heterojunction TFET with 4 nm body thickness, computed by the ballistic and the scattering model, is shown in Fig. 3.9 (a) and (b). The deep quantum well states are marked with the black circle. In the ballistic simulation, the deep quantum well states are slightly occupied by the carriers injected from the contacts. While for the scattering model, the quantum well states are populated by the scattering thermalized carriers, which is close to the real situation when devices operate at room temperature.
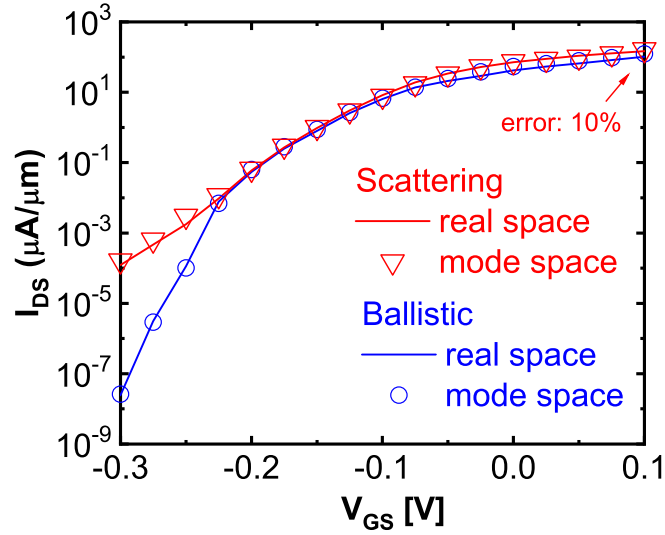


Fig. 3.10.: Transfer IV characteristics of a triple heterojunction TFET with 4 nm body thickness computed with and without scattering effects considered.

The thermalized quantum well states introduce the leakage path and increase the sub-threshold leakage. Fig. 3.10 compares the 4 nm thick triple heterojunction TFET's transfer IV characteristics with and without scattering. With scattering, the sub-threshold current at $V_{GS}$ = -0.3 V is $10^3$ times higher than the results of the ballistic simulation. The MS approximation is also applied to the scattering simulation, and it introduces a small $\Delta I_{err}$ of 10%.

The effect of energy broadening is shown in Fig. 3.11. The transfer IV characteristics of the triple heterojunction TFET with 4 nm body thickness is computed for different energy broadening ($\eta$), ranging from 0 to 10 meV. At the OFF-state, the leakage current significantly depends on the energy broadening. In Fig. 3.11 (a), the OFF leakage at $V_{GS} = $ -0.2 V increases by an order of three when the energy broadening increases from 0 meV to 10 meV. However, if the gate work function is adjusted to have $I_{DS} = 10^{-3}$ $\mu$A/$\mu$m fixed at $V_{GS} = 0$ V as shown in Fig. 3.11 (b), the energy broadening increases the sub-threshold swing when $V_{GS} < 0.2$ V but it does not affect the ON current at $V_{GS} = 0.3$ V.
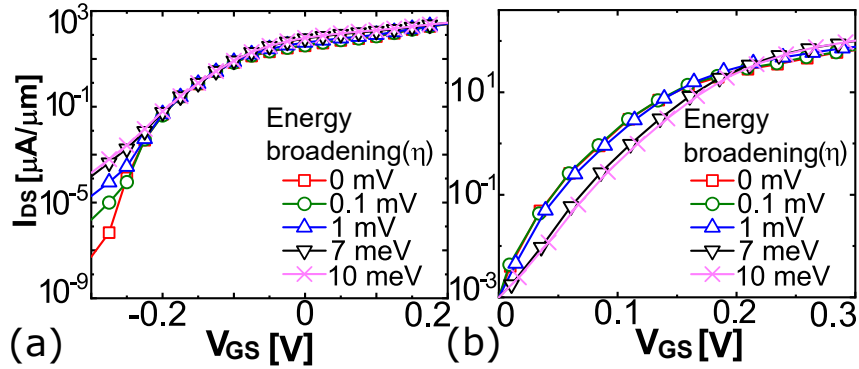


Fig. 3.11.: Transfer IV characteristics of 4 nm thick triple heterojunction TFETs computed with different energy broadening ($\eta$), ranging from from $\eta = 0$ mV to $\eta = 10$ mV. (a) is computed assuming a fixed gate metal work function while (b) is computed with an adjusted gate metal work function to impose a fixed OFF current of $10^{-3}$ $\mu$A/$\mu$m at $V_{GS} = 0$ V.

The results of the scattering model for the 12 nm thick triple heterojunction TFET are shown in Fig. 3.12, where (a) are the transfer IV characteristics, and (b) are the extracted sub-threshold swings. Both the ballistic and the scattering results are plotted to show the introduced degradation from scattering. Contrary to the 4 nm thickness case, for the 12 nm thickness case, the scattering and the ballistic simulations give very similar results. The reason is that the thermalized quantum well states in the 12 nm thick device have a long tunneling distance in the channel
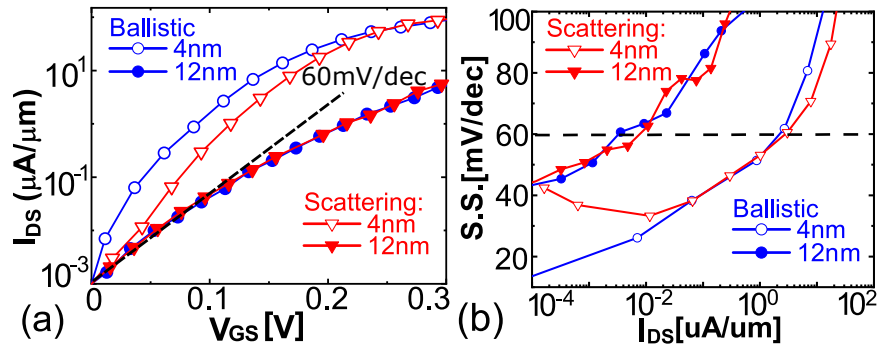
Fig. 3.12.: (a) Transfer IV characteristics and (b) sub-threshold swing computed with and without scattering effects for triple heterojunction TFET with the body thickness of 4 nm and 12 nm.
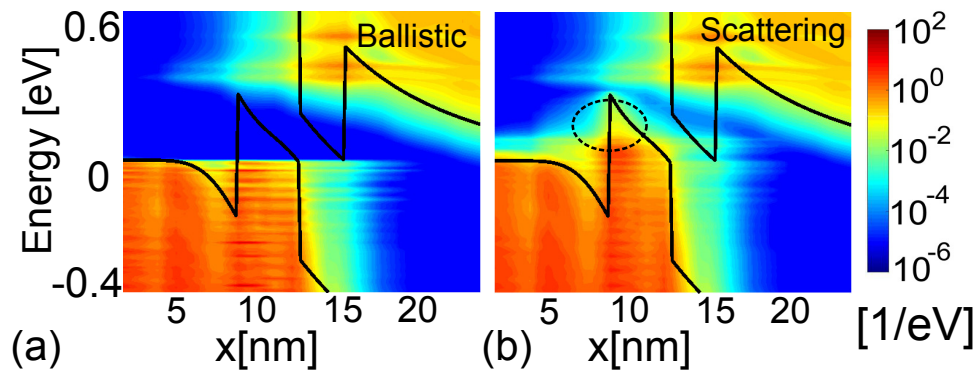


Fig. 3.13.: LDOS for a triple heterojunction TFET with the body thickness of 12 nm at OFF-state ($V_{GS}$ = -0.3 V) computed from (a) ballistic simulation and (b) simulation with scattering effects. The LDOS contributions due to the scattering effects are indicated with the dashed lines.

to tunnel through, which leads to a low transmission probability. Fig. 3.13 (a) and (b) are the 12 nm thick triple heterojunction TFET's OFF-state LDOS computed by the ballistic model and the scattering model. The marked thermalized quantum well states have a negligible contribution to the OFF leakage due to the long tunneling distance toward the drain. For the triple heterojunction devices, the scattering effects in the quantum wells, that couples states in the quantum wells, is the main contributor

for the leakage current at the OFF state. The influence of the band-tail is a second-order effect. Therefore, we expect that the Urbach tails have a minor impact on the 12 nm thick triple heterojunction TFET.

## 3.7 Summary

In this work, the triple heterojunction tunneling FinFET with the body thickness of 12 nm is studied using the mode space approximation. The sub-threshold swing retains sub-60 mV/dec value, and the degradation due to the scattering is negligible. The transformation matrix that generates the mode space basis is found transferable for different strains and transverse wave vectors, which is a convenient feature for the mode space UTB simulations. When the mode space approximation is applied in the heterojunction devices, un-physical states at the heterojunction interface can be introduced if the mode space energy window is chosen too small. However, the error can be reduced by increasing the mode space basis's energy window to cover the depth of the quantum well. Overall, the combination of the mode space approximation and the empirical scatting model made the analysis of TFET with a realistic dimension possible.

# 4. DOPING PROFILE ENGINEERED TRIPLE HETEROJUNCTION TFETS WITH 12 NM BODY THICKNESS

## 4.1 introduction

Power consumption in CPUs has impacted Moore's law significantly [7,10]. An obvious solution to reduce the power supply is to replace the metal-oxide-semiconductor field-effect transistors (MOSFETs), which is limited by the Boltzmann tyranny, with new devices like the tunneling field-effect transistors (TFETs) [11–17, 19, 21] and negative-capacitance field-effect transistors (NC-FETs) [92,93]. However, these steep sub-threshold slope devices come with challenges that hinder their wide-spread applications. The primary challenge of TFETs is its low ON-current. TFETs are shown to suffer from low ON-current issue since the quantum tunneling probability is usually much lower than one [20].

The tunneling probability depends on several factors, such as tunneling distance, electric field, resonance conditions, and effective tunneling mass. Several approaches have been introduced to increase the tunneling probability based on optimizing these four factors. For example, in GaN-based heterojunction TFETs, the tunneling distance is reduced by engineering the band-diagram [94]; in a dielectric engineered TFET, the electric field at the tunneling junction is increased by using two different dielectrics [28]; in a resonance-TFET, quantum resonance is used to increase the tunneling probability close to one [95]; in a Phosphorene-based TFET, low effective tunneling mass increases the tunneling probability [96].

A triple heterojunction (THJ-) TFET based on III-V materials allows an advantage in optimizing all of the factors mentioned above. A triple heterojunction reduces the tunneling distance with band diagram engineering. It also uses resonance tun-

neling to improve the tunneling probability in the ON-state and provides low enough effective tunneling mass with the use of right III-V materials [31, 85, 86, 97].

Despite the benefits of THJ-TFETs, the fabrication constraints such as device dimensions and material combinations limit the performance of a THJ-TFET. For example, a 4nm thick THJ-TFET with a conventional PIN doping profile shown in Fig. 4.1(a) predicts an excellent performance; however, as the body thickness ($T_{ch}$) approaches a realistic value of 12 nm, the performance degrades. In order to address these issues in designing THJ-TFETs, considering fabrication constraints, the doping profile is engineered, as shown in Fig. 4.1(b).

In this paper, the THJ-TFET design considerate of the fabrication technology constraints is proposed. The constraints include the limitation of the doping density in each material, the width of the strained quantum well, the crystal growth direction, and the choice of the channel material to have a high-quality oxide interface. The proposed design shows the sub-threshold swing of 40 mV/dec over four orders of drain current. The high ON-current of 325 uA/um is achieved with a low supply voltage ($V_{DD}$) of 0.3 V.

The device design optimization is performed using Nanoelectronics Modeling tool: NEMO5 [62, 63]. The atomistic tight-binding method with ten orbitals $sp^3d^5s^*$ basis is used [98, 99]. Carrier transport in THJ-TFETs is complicated due to the presence of quantum wells in the tunneling region. The quantum mechanics of the system includes the thermalization of carriers in these quantum wells, tunneling process at multiple interfaces, and quantum confinement effects. In order to capture these mechanisms, atomistic quantum transport simulation, including effective thermalization [69, 70], is necessary to evaluate the device performance. Since atomistic simulation is computationally challenging for devices with a large dimension, the tight-binding mode-space approach developed in [100] is applied in this work.

The paper is organized into four sections. The THJ-TFET device structure considering fabrication constraints is displayed in section II. The design rules and the issue of THJ-TFET with the body thickness of 12 nm are discussed in section III. In

section IV, we demonstrate the performance of the proposed THJ-TFET. And, the impact of the channel doping density is further discussed in section V.

## 4.2 THJ-TFET device structure

Fig. 4.1 shows the double-gated ultra-thin-body (UTB) THJ-TFET studied in this work. Fig. 4.1(a) is the THJ-TFET with a conventional PIN doping profile. It consists of a P-doped source, an intrinsic channel, and an N-doped drain. In the P-doped source, $In_{0.53}Ga_{0.47}As$ and $GaAs_{0.51}Sb_{0.49}$ have the doping density of $N_a = 5 \times 10^{19}$ cm$^{-3}$. InAs and InP channel are intrinsic. In the N-doped drain, InP has the doping density of $N_d = 2 \times 10^{19}$ cm$^{-3}$.

The UTB confinement direction is along $\langle 011 \rangle$. The electron transport direction is along $\langle 100 \rangle$. The electron transport direction is the same as the crystal growth direction to simulate the device structure fabricated by the vertical Fin-TFET technology [36]. The choice of the materials in the heterojunction has considered current crystal growth technology limitations. The substrate is assumed to be InP such that InAs quantum well is under 3.41% bi-axial compressive strain. While $In_{0.53}Ga_{0.47}As$ and $GaAs_{0.51}Sb_{0.49}$ are not strained since they are lattice-matched to InP substrate. The technology of growing $In_{0.53}Ga_{0.47}As$, $GaAs_{0.51}Sb_{0.49}$, and InAs on InP(100) substrate through molecular beam epitaxy (MBE) are all well-developed [101–103]. The width of $GaAs_{0.51}Sb_{0.49}$ source quantum well is 3.6 nm. The width of strained InAs channel quantum well is 2.4 nm, which is less than the critical thickness of 4 nm [104, 105]. The gate length is 30 nm, and the oxide thickness is 3.2 nm. The oxide material is assumed to be $ZrO_2$ with a relative dielectric constant of 15. The source is grounded. The drain is applied the supply voltage ($V_{DD} = 0.3$ V). The source to drain bias ($V_{DS}$) is 0.3 V. The spacer in this work is assumed to be air with the dielectric constant of 1.

Fig. 4.1(b) is the proposed design with the same device structure as Fig. 4.1(a) while the doping is engineered to PNPN doping profile. In the optimized PNPN
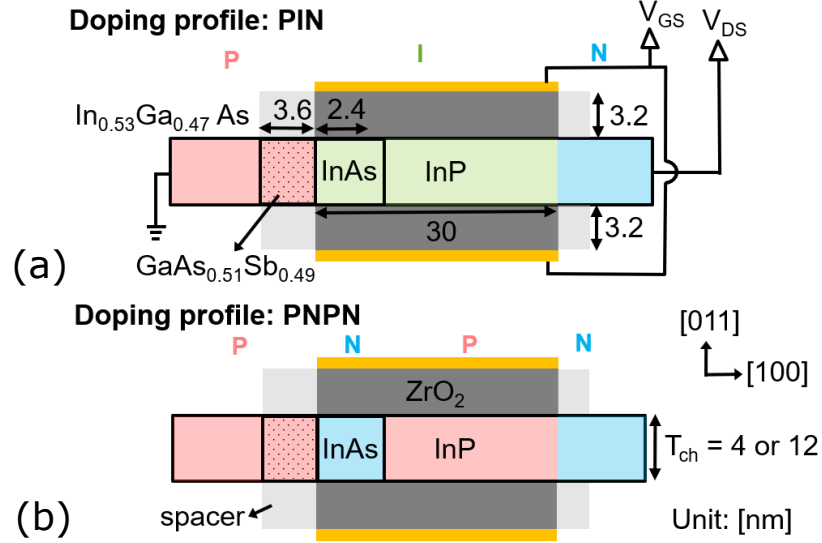
Fig. 4.1.: Device design of a triple heterojunction TFET with (a) conventional doping profile (PIN) and (b) an optimized doping profile (PNPN).

doping profile, InAs channel quantum well is doped to N-type with $N_d = 2 \times 10^{19}$ cm$^{-3}$ . InP channel is doped to P-type with $N_a = 2 \times 10^{19}$ cm$^{-3}$.

## 4.3 THJ-TFET design principles

Before analyzing PNPN-doped THJ-TFET, the design principle of THJ-TFETs is introduced in this section. The energy-resolved local density of states (LDOS) and transmission probability for the THJ-TFET with different body thicknesses ($T_{ch}$) are shown in Fig. 4.2. The doping profile is a conventional PIN doping profile shown in Fig. 4.1(a). The LDOS in Fig. 4.2 is calculated when the device is operated in the ON-state, where the gate to source bias ($V_{GS}$) is 0.3 V. In Fig. 4.2(a), the alignment of the resonant states in the GaAsSb and InAs quantum wells results in the enhanced resonant tunneling such that the transmission probability is close to 1. On the other hand, in Fig. 4.2(b), when the body thickness increases to 12 nm, the resonant states are not aligned due to the worse electrostatic. The transmission, therefore, reduces 1~2 orders compared to the case of 4 nm body thickness.
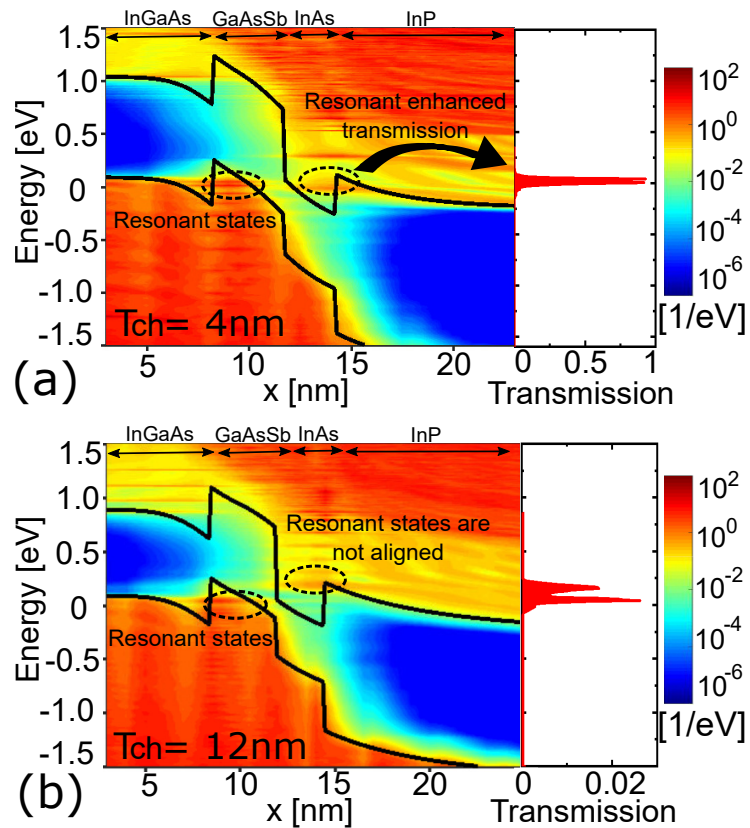
Fig. 4.2.: Energy-resolved local density of states and transmission for the (a) 4 nm and (b) 12 nm thick triple heterojunction TFET when the device is operated in the ON-state where $V_{GS} = 0.3$ V.

The key design rule of THJ-TFETs is to align the resonant states of two quantum wells in the tunneling junction and to introduce the resonant enhanced transmission. In the next section, the performance of 12 nm thick THJ-TFET is improved by aligning the resonant states through the proposed PNPN doping profile shown in Fig. 4.1(b).

## 4.4   THJ-TFET with PNPN doping profile

In this section, the performance of THJ-TFET with the PNPN doping profile is demonstrated. Although, the PNPN doping profile was originally proposed for

homojunction TFETs to improve electric field in the tunneling region [106–109], it plays a more significant role in THJ-TFETs with thick body thickness. The PNPN doping profile can be engineered in THJ-TFETs not only to increase the electric field, but also to help aligning the resonant states that introduces the resonance tunneling.

Fig. 4.3(a) compares the transfer characteristics of THJ-TFETs with 4 nm and 12 nm body thicknesses for different doping profiles. The gate to source bias ($V_{GS}$) are shifted to have a fixed OFF-current value of $10^{-3}$ $\mu A/\mu m$ at $V_{GS} = 0$ V. For THJ-TFET with the PIN doping profile, when the body thickness increases from 4 nm to 12 nm, the gate control degradation dominates the performance such that the ON-current ($I_{ON}$) decreases by a factor of $\sim$16.

However, for THJ-TFET with the optimized PNPN doping profile, the same thickness increment is shown to improve the ON-current by $\sim$30%. The reason is that, when the body thickness increases from 4 nm to 12 nm, the engineered built-in electric field in tunneling junction alleviates the effect of gate control degradation by a better doping profile design. At the same time, the decrease of the confined materials' bandgaps ($E_g$) enhances the ON-current [77]. The bandgaps of the materials used

Table 4.1.: The confined bandgap ($E_g$) and valence band off-set ($\Delta E_V$) of the heterojunction materials used in the design. The UTB's confinement direction is along $\langle 110 \rangle$. The atomistic tight-binding parameters used in this work is from [98].

| $T_{ch}$ | | InGaAs | GaAsSb | InAs | GaAsSb |
|---|---|---|---|---|---|
| 4 nm | $E_g$ [eV] | 0.9517 | 0.9871 | 0.7016 | 1.504 |
| | $\Delta E_v$ [eV] | 0 | 0.4238 | 0.0456 | -0.3796 |
| 12 nm | $E_g$ [eV] | 0.7993 | 0.8456 | 0.5010 | 1.3822 |
| | $\Delta E_v$ [eV] | 0 | 0.4273 | 0.0670 | -0.3902 |
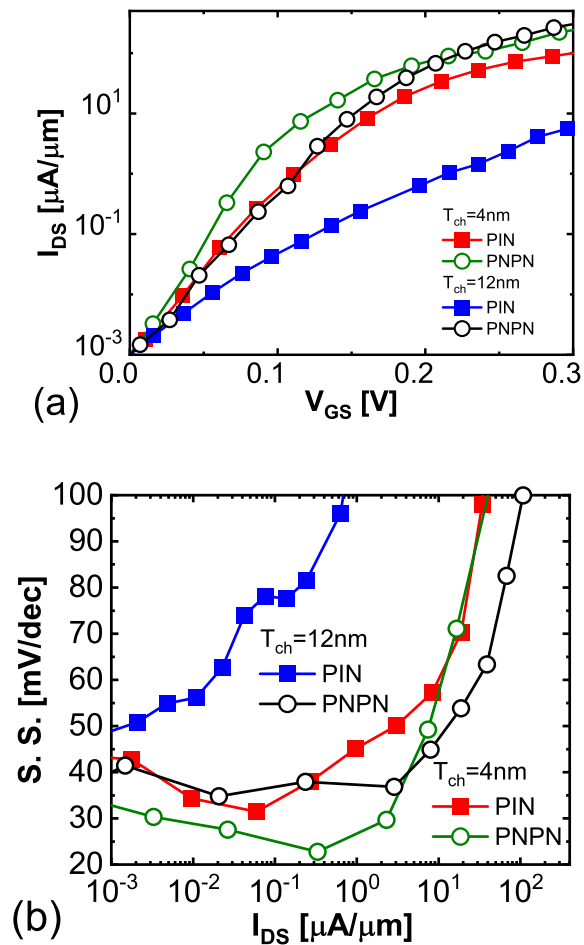
Fig. 4.3.: (a) Transfer characteristics and (b) the S.S - $I_{DS}$ curve of a triple hetero-junction TFET with a conventional doping profile (PIN) and the optimized doping profile (PNPN) for different body thicknesses ($T_{ch}$) of 4 nm and 12 nm.

in the heterojunctions for different body thicknesses are listed in TABLE 4.1. The ON-current of the THJ-TFET with different body thicknesses and the doping profiles is summarized in TABLE 4.2.

The sub-threshold swing (S.S.)-$I_{DS}$ curve for the THJ-TFETs with the PIN doping profile and the optimized PNPN doping profile for 4 nm and 12 nm thick THJ-TFETs are demonstrated in Fig. 4.3(b). For a body thickness of 4 nm, the sub-threshold swing for the conventional PIN doping profile and the optimized PNPN

Table 4.2.: The ON-current ($I_{ON}$) of the triple heterojunction TFET with body thicknesses of 4 nm and 12nm for both - conventional PIN doping profile and the PNPN doping profile - are listed. The $I_{ON}$ is extracted at $V_{GS} = 0.3$V.

| $T_{ch}$ | 4 nm | 12 nm | 4 nm | 12nm |
|---|---|---|---|---|
| Doping profile | (PIN) | (PIN) | (PNPN) | (PNPN) |
| $I_{ON}$ [$\mu A/\mu m$] | 98 | 6 | 248 | 325 |

doping profile does not have much difference. Both doping profiles exhibit decent performance. However, as the body thickness increases to 12 nm, the optimized PNPN doping profile retains its high performance, whereas the conventional PIN doping profile degrades drastically.

To further understand why THJ-TFET with the optimized PNPN doping profile has a better performance comparing to the case of the traditional PIN doping profile, the local density of states (LDOS) at $V_{GS} = 0.3$ V for different body thicknesses and different doping profiles are shown in Fig. 4.4.

When the channel thickness of the PIN-doped THJ-TFET increases from 4 nm to 12 nm, the quantum well states are misaligned, as shown in Fig. 4.4(a) and (c). The resonant states in the InAs channel quantum well are outside the tunneling window. The lack of resonance tunneling leads to significant degradation of the transmission probability and the ON-current. On the other hand, the optimized PNPN doping profile helps to retain the alignment of GaAsSb and InAs quantum well states in the 12 nm thick THJ-TFET, as shown in Fig. 4.4(d). The performance of 12 nm thick THJ-TFETs with the optimized PNPN doping profile is, therefore, similar to the case of a thinner channel thickness.

The tunneling distance is determined by the electric field in TFET's tunneling region. Generally, the tunneling distance of a TFET with a conventional PIN doping
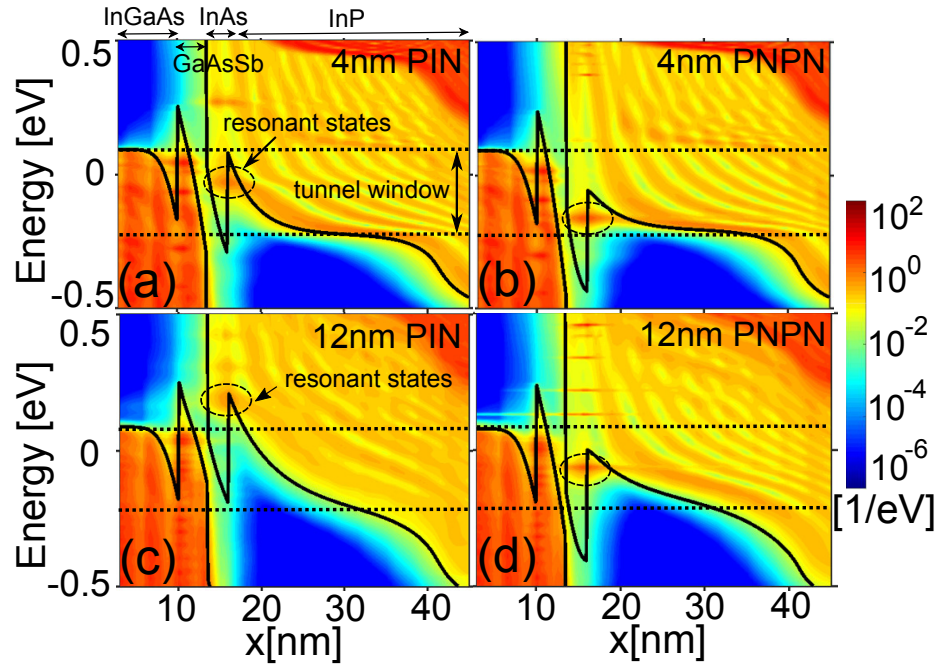
Fig. 4.4.: Local density of states (LDOS) of the triple heterojunction TFETs with the body thickness/doping profile of (a) 4 nm / PIN, (b) 4 nm / PNPN, (c) 12 nm / PIN, and (d) 12 nm / PNPN. LDOS is calculated in the ON-state where $V_{GS} = 0.3$ V.

profile is highly sensitive to the body thickness; a thinner device has a stronger gate control that leads to a smaller natural scaling length and hence a smaller tunneling distance [100, 110, 111]. Since the device with an optimized PNPN doping profile has no intrinsic region in the channel, the scaling lengths are dominated by the depletion width corresponding to the doping profile [111]. As a result, the optimized PNPN doping profile is not just engineered to increase the electric field in the tunneling junction; it also reduces the sensitivity of the performance to the body thickness. Fig. 4.5 shows the impact of doping profile and body thickness on the electric field along the channel. The peak electric field in PNPN doped THJ-TFETs has less dependence on the body thickness compared to the conventional PIN doped THJ-TFETs.
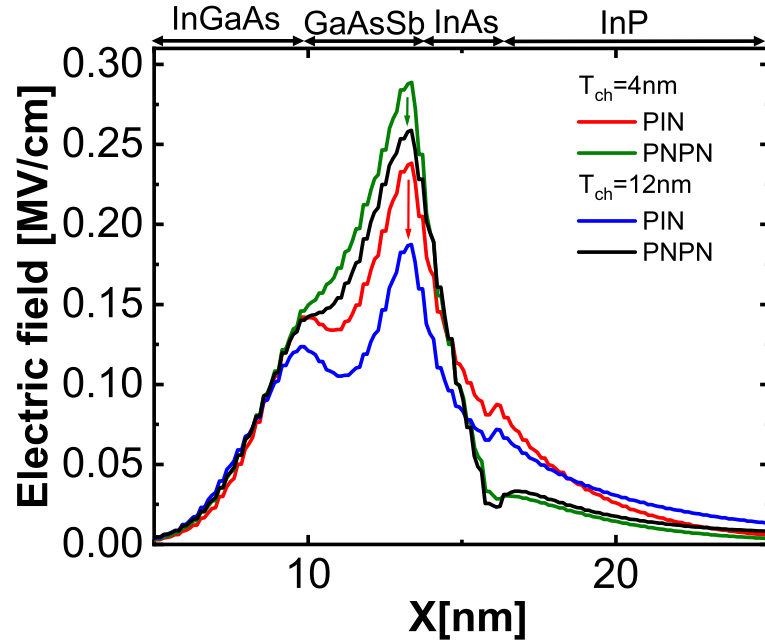
Fig. 4.5.: Electric field along the channel for 4 nm and 12 nm thick triple hetero-junction TFETs with conventional PIN doping profile and optimzed PNPN doping profile. The electric field is obtained when the device is operated in the ON-state where $V_{GS} = 0.3$ V.

Table 4.3.: $I_{ON}$ at $V_{GS} = 0.3$ V of the 12 nm thick THJ-TFET with different doping profile - conventional PIN doping profile and the PNPN doping profile - are listed.

| Doping profile | PIN | PNPN | PNPN | PNPN |
|---|---|---|---|---|
| P-InP channel doping | - | $1 \times 10^{16}$ | $5 \times 10^{18}$ | $2 \times 10^{19}$ |
| $I_{ON}$ $[\mu A/\mu m]$ | 6 | 50 | 78 | 325 |
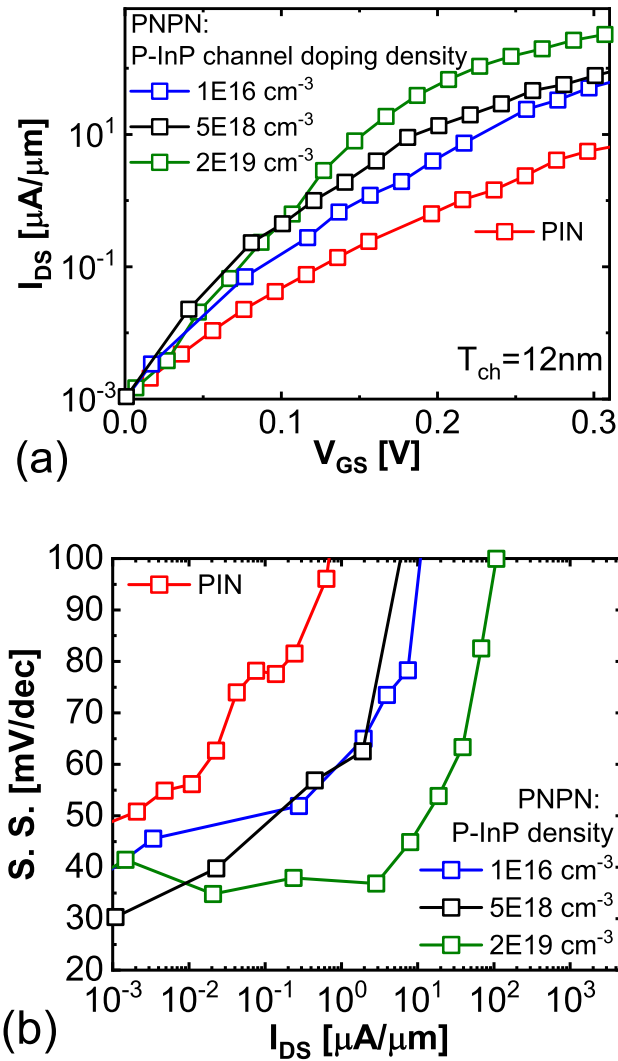
Fig. 4.6.: (a) Transfer characteristics and (b) S.S. - $I_{DS}$ curve of the 12 nm thick triple heterojunction TFETs with the PIN and PNPN doping profile. The PNPN-doped TFET with different P-InP channel doping density are demonstrated.

## 4.5   P-doped InP channel doping density

The benefit of having a P-N junction in the tunneling region is intuitive and is well-studied [106–109]. The electric field in the tunneling region is enhanced by P-N junction's built-in potential and therefore leads to a smaller tunneling distance and a

larger transmission probability. The design rule of the P-N junction in the tunneling region is to maximize the doping density to achieve the maximum build-in potential. However, the role of the P-doped channel in the PNPN-doped THJ-TFET is not yet well understood. In this section, the doping density of the P-doped InP channel is studied.

The transfer characteristics and S.S. - $I_{DS}$ curve of PNPN-doped THJ-TFET with different P-InP channel doping density are shown in Fig. 4.6. The body thickness of the device is 12 nm. The ON-current at $V_{GS} = 0.3$ V is summarized in TABLE 4.3. The PNPN-doped THJ-TFET with P-InP channel doping density of $1 \times 10^{16}$ $cm^{-3}$ is the reference case to observe the improvement from applying the P-N junction in the tunneling region. The ON-current increases from 6 $\mu A/\mu m$ to 50 $\mu A/\mu m$ when the doping profile is replaced from PIN doping profile to PNPN doping profile with P-InP channel doping density of $1 \times 10^{16}$ $cm^{-3}$.

Interestingly, we found the performance of 12 nm thick THJ-TFET improves slightly when P-InP channel doping density increases from $1 \times 10^{16}$ $cm^{-3}$ to $5 \times 10^{18}$ $cm^{-3}$. The ON-current only increases from 50 $\mu A/\mu m$ to 78 $\mu A/\mu m$. The case with InP cahnnel doped to $5 \times 10^{18}$ $cm^{-3}$ shows sub-40 mV/dec S.S. for a limited range of drain current ($I_{DS}$). However, when P-InP channel doping density further increases to $2 \times 10^{19}$ $cm^{-3}$, the performance improves significantly. The ON-current of such case reaches 325 $\mu A/\mu m$. It exhibits an S.S. less than 40 mV/dec over four orders of magnitude in the drain current.

To further understand the impact of P-InP channel doping density, the ON-state local density of state (LDOS) and 2D-potential of the 12 nm thick THJ-TFETs with different doping profiles is compared in Fig. 4.7 and Fig. 4.8. In Fig. 4.7, the LDOS, and the band-diagram are extracted at 1 nm away from the edge of the channel, where the potential is significantly affected by the gate bias. The resonant states in InAs quantum well are outside of the tunneling window in the case of PIN doping profile. On the other hand, for the cases of PNPN-doped THJ-TFET, the resonant states are all located inside the tunneling window regardless of different P-InP channel doping
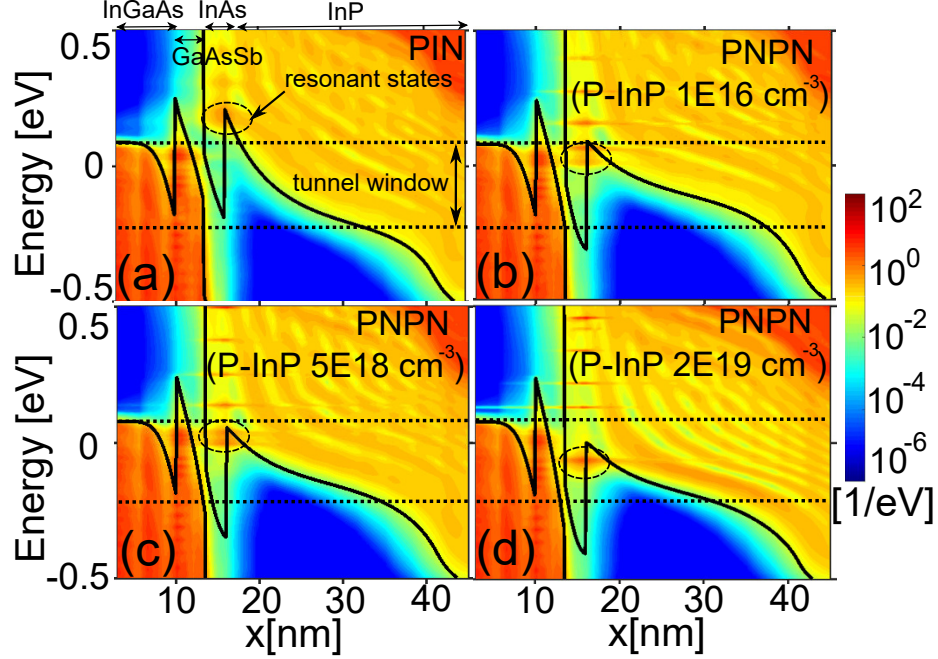
Fig. 4.7.: Local density of states of 12 thick THJ-TFET with (a) the PIN doping profile and (b), (c), (d) the PNPN doping profile. The P-InP channel doping density in (b), (c), and (d) are $1 \times 10^{16}$, $5 \times 10^{18}$, and $2 \times 10^{19}$ $cm^{-3}$, respectively. The local density of states are calculated in the ON-state when $V_{GS} = 0.3$ V.

density. Fig. 4.8 also shows that the horizontal field at the interface of the GaAsSb source quantum well and InAs channel quantum well increases when the PIN doping profile is replaced by the PNPN doping profile. The reason is that a P-N junction in the tunneling region has a larger built-in electric field than a P-I junction when other parameters are the same.

In the case of PNPN-doped THJ-TFET with P-InP channel doped to $2 \times 10^{19}$ $cm^{-3}$, we can see a clear difference in potential compared to the case of P-InP channel with less doping density. In Fig. 4.7(d), the channel potential barrier is much lower comparing to that in Fig. 4.7(b) and (c). This explains why PNPN-doped THJ-TFET with P-InP channel doped to $2 \times 10^{19}$ $cm^{-3}$ has a superior performance compare to the rest of the cases.

In Fig. 4.8(d), a stronger vertical electric field toward the gate/channel interface is observed. We further calculate the band diagram at the edge and the center of the channel and show in Fig. 4.9. Increasing P-InP channel doping density pushes up the valence band in the center of the channel, which increases the channel barrier. However, it also pushes down the valence band close to the channel-oxide interface (depleted region), which opens up a low resistant path for current to flow. The barrier
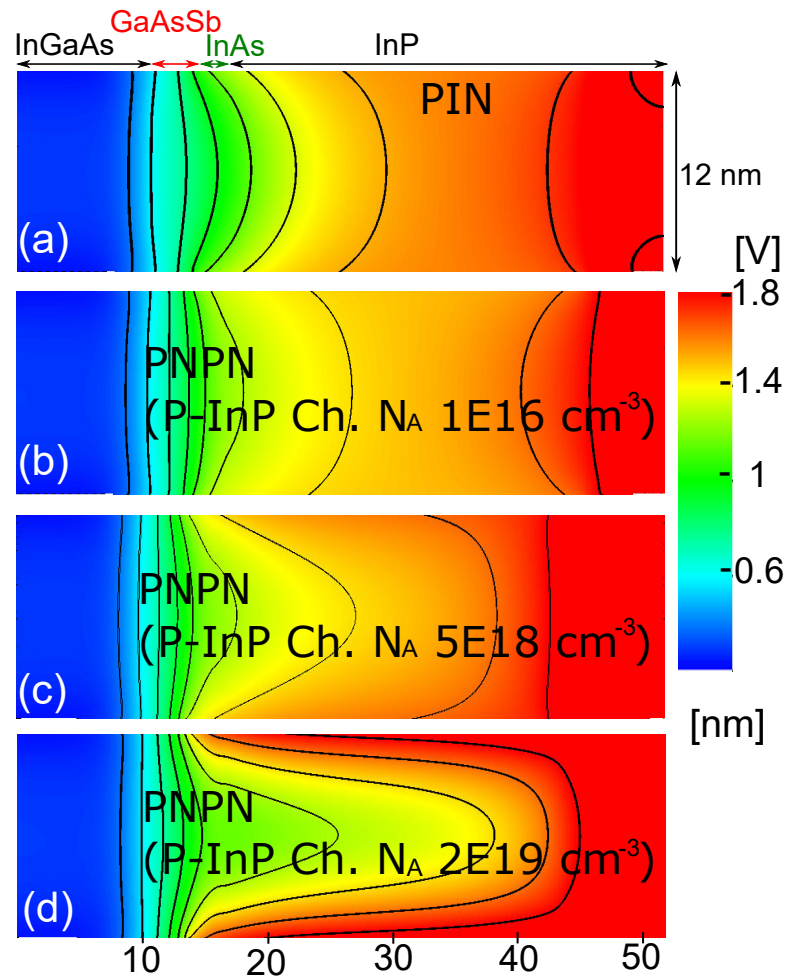


Fig. 4.8.: Channel potential of the (a) PIN and (b), (c), (d) PNPN doping profile. The P-InP channel doping density in (b), (c), and (d) are $1 \times 10^{16}$ $cm^{-3}$, $5 \times 10^{18}$ $cm^{-3}$, and $2 \times 10^{19}$ $cm^{-3}$, respectively. The potential are obtain in the ON-state when $V_{GS} = 0.3$ V.
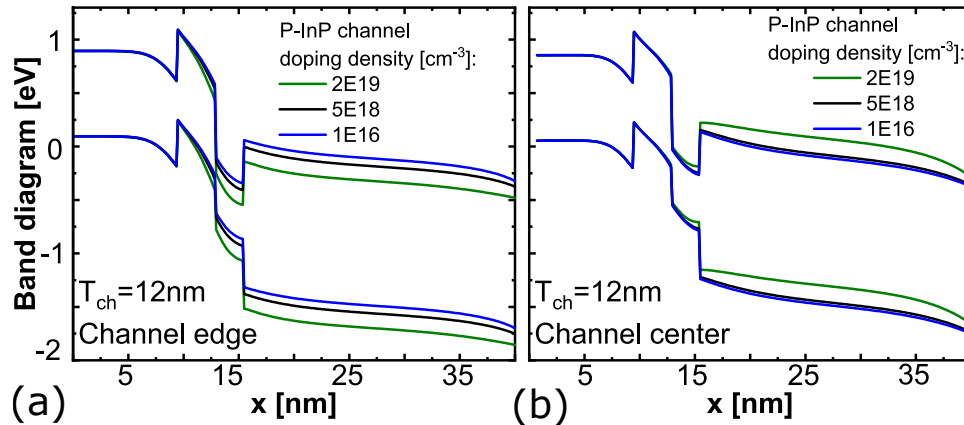
Fig. 4.9.: The ON-state band diagram calculated at (a) the edge and (b) the center of the channel.

lowering at the edge of the channel results in a higher ON-current as P-InP channel doping density increases.

## 4.6 Summary

In this work, a triple heterojunction TFET design is proposed, considering fabrication constraints such as the channel thickness and the limitation in doping density of the materials. Triple heterojunction TFET with a conventional PIN doping profile is shown to degrade in performance when the body thickness increases from 4 nm to 12 nm. The doping profile is engineered to increase the electric field in the tunneling junction and reduce the sensitivity of the performance to the body thickness. The ON-current of the optimized design reaches 325 $\mu A/\mu m$, and the S.S. is less than 40 mV/dec over four orders of magnitude in the drain current.

# 5. THE ELECTRONIC STRUCTURE OF SI:P $\delta$-DOPED LAYER

## 5.1    Abstract

Quantum computing architectures based on dopant atoms in Silicon use a single dopant atom precisely placed in a silicon lattice as a building block [112–117]. Scanning tunneling microscopy (STM) lithography and low-temperature Si molecular beam epitaxy (MBE) allow a Phosphorus atom to be placed in a bulk Silicon with an atomic-scale accuracy [118,119]. Si:P $\delta$-doped layer is a densely doped Phosphorus layer in the bulk Silicon fabricated using this technology. This is an essential step towards building scalable donor-based quantum computing systems. Fig. 5.1 shows an STM image of a donor-based quantum computing device [120]. Each quantum dot is formed by a donor cluster with one or two Phosphorus atoms. The source (S), drain (D), and gates (G1 and G2) are made of the Si:P $\delta$-doped layer.

Fig. 5.2 is the schematic of the Si:P $\delta$-doped layer. The red rectangular block is the bulk Silicon supercell. It is periodic along with the crystal directions [100] and [010]. The Si:P $\delta$-doped layer is marked with a blue square with dimensions 1.1 nm × 1.1 nm. This one-atom-thin layer of each supercell has two Phosphorus atoms and six Silicon atoms; the doping density is, therefore, 1/4 ML (ML: monolayer), which is equivalent to a 2D doping density of $10^{14}$ $cm^{-2}$. This extremely highly doped Si:P
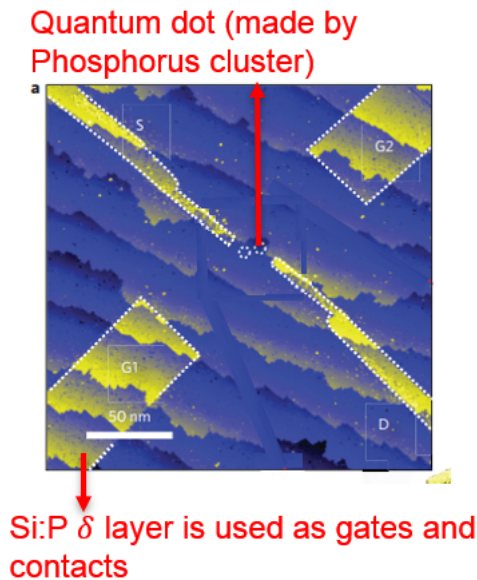
Fig. 5.1.: Scanning tunneling microscopy (STM) image of a donor-based quantum computing system. The yellow contacts (S, D, G1, and G2) are the Si:P $\delta$-doped layers [120]. Reprint with permission from Bent Weber, Y. H. Matthias Tan, Suddhasatta Mahapatra, Thomas F. Watson, Hoon Ryu et al., "Spin blockade and exchange in Coulomb-confined silicon double quantum dots.", Nature Nanotechnology. Copyright © 2014, Springer Nature.

$\delta$-doped layer is close to an ideal Ohmic contact and is extensively used as contacts in the Phosphorus donor-based quantum computing systems.

The electronic structure of the Si:P $\delta$-doped layer is measured with the high-resolution angular-resolved photoemission spectroscopy (ARPES). The ARPES measurements were conducted by Federico Mazzola and Justin W. Well from the Physics Department of the Norwegian University of Science and Technology. The details of the experimental set up can be found at [88].

In contrast to the previously published theoretical and experimental works, a third distinct sub-band is observed in the new ARPES experimental data. The possible origins of the third sub-band are investigated in this work, including the asymmetric doping profile, spin-orbit interaction, and electron-electron interaction. It is con-
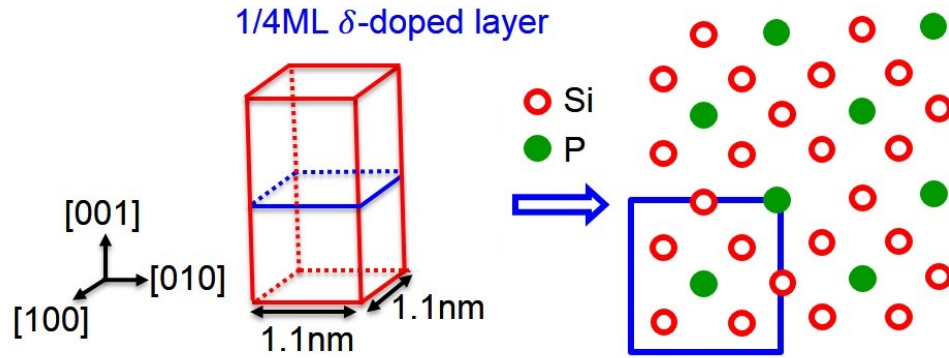
Fig. 5.2.: Schematic of the Si:P $\delta$-doped layer. The red rectangular block is the bulk Silicon supercell. It's periodic along the crystal directions [100] and [010]. The blue square marks the Si:P $\delta$-doped layer in the bulk Silicon. The blue square consists of two Phosphorus atoms and six Silicon atoms.

cluded that the dielectric constant $(\varepsilon_r)$ has been underestimated in previous publications [121]. [121] assumes the system's dielectric constant is similar to the bulk Silicon. However, due to the heavy doping of Silicon with the Phosphorus atoms, the dielectric constant should be doubled for the Si:P $\delta$-doped layer [122].

Once we consider this factor into the empirical tight-binding calculations, the band structure obtained from the simulation agrees with the ARPES experiments. Specifically, the simulations show the existence of the three sub-bands beneath the Fermi level $(E_f)$, the separation of the sub-bands, and the curvature of the sub-bands, correctly as observed in the experiments. This new understanding of the band structure has important implications for quantum proto-devices, which are built on the Si:P $\delta$-doped layer platform. The finding of the correct dielectric constant of the Si:P $\delta$-doped layer improves the electrostatic modeling's accuracy for the quantum proto-device.

## 5.2 Si:P $\delta$-doped layer electronic structure simulation method

In the ETB simulation, the Phosphorus donor in the Silicon is treated as a Hydrogen-liked Coulomb potential that is explicitly superimposed in the Silicon tight-binding Hamiltonian. This Coulomb potential was empirically bench-marked with the binding energy of an ionized Phosphorus donor [123, 124]. These parameters accurately predict various experiments such as the donor qubit's relaxation time [125,126], the hyperfine coupling [115, 127], and the donor cluster's multi-electron wave functions [128].

Since a heavily doped Si:P $\delta$-doped layer is a metal-like system, the screening effect, and the electron-electron interaction can not be ignored. The electron screening is included by solving the Poisson-Schroedinger equation and the electron-electron interaction with the local density approximation (LDA) that includes the exchange-correlation interaction. The simulation flow is shown in Fig. 5.3.

The electron distribution (n(r)) is calculated from the eigenfunction with its eigenenergy below the Fermi-energy ($E_F$). The number of electrons included in the system is the same as the number of Phosphorus donors to ensure a charge-neutral system.

It must be noted that the role of the dielectric constant ($\varepsilon_r$) in the Slater-Koster tight-binding method [129] is not the same as the ab-initio density function theory (DFT). In DFT, typically, the core and the valence electrons are considered, and n(r) is computed by populating all of these electronic states up to the $E_F$ through self-consistent iterations of the Kohn-Sham equations [130]. Hence, a $\varepsilon_r$ of vacuum ($\varepsilon_r = 1$) is used.

In this work, the Slater-Koster tight-binding method is used. Only the "donor electrons" are included for charge self-consistency (i.e., only the extra electron bound to the Phosphorus donor that does not participate in bonding with its neighboring Silicon atoms). The bonded electrons in the Silicon background are assumed frozen. Hence, the Poisson equation is solved with the material environment's $\varepsilon_r$, which is
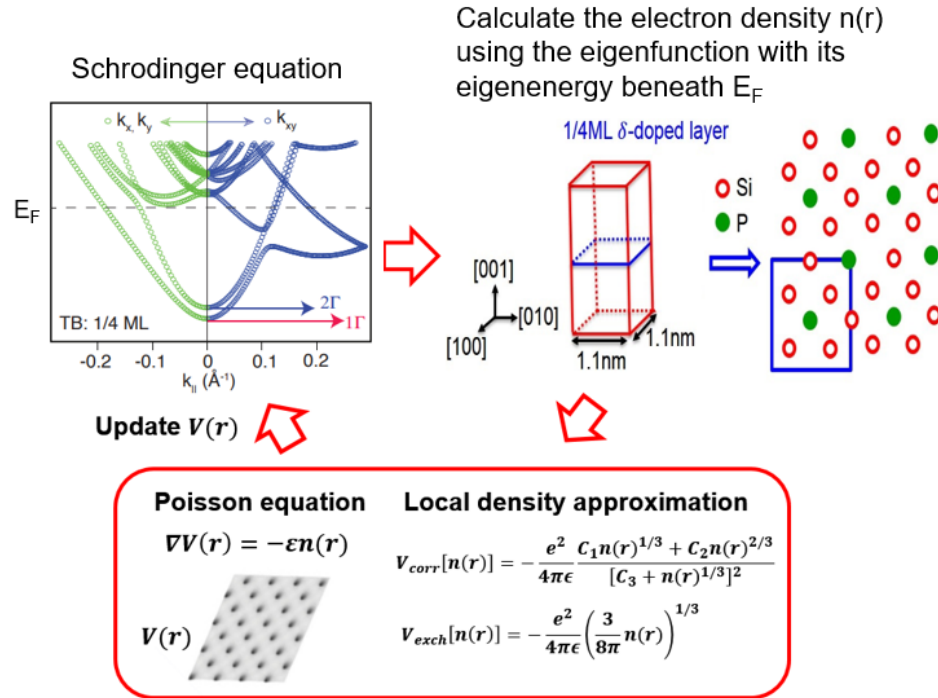
Fig. 5.3.: Methodology for electronic structure calculations of the Si:P $\delta$-doped layer [88, 121].

assumed to be Silicon ($\varepsilon_r = 11.9$) in this case. This is a standard technique for the empirical tight-binding method in atomistic device simulations where the Poisson and Schrodinger/Green's functions are solved self-consistently with the device material's $\varepsilon_r$ as an input [51, 77, 131].

## 5.3 Review Si:P $\delta$-doped layer electronic structure

### 5.3.1 overview

Fig. 5.4 shows the 2D electronic structure of Si:P $\delta$-doped layer. The simulation parameters are the same as the previous publication [121]. The electronic structure of the Si:P $\delta$-doped layer has three sub-bands beneath the Fermi-level ($E_F$), indicating its metal-like material properties. Two sub-bands marked with the red dash lines are

at the $\Gamma$ point and are denoted as 1$\Gamma$ and 2$\Gamma$. 1$\Gamma$ and 2$\Gamma$ sub-bands are the projection of the two Z-valleys from the 3D k-space of the bulk Silicon. On the other hand, one sub-band marked with the yellow dash line is at the $\Delta$ point and is denoted as 1$\Delta$. 1$\Delta$ sub-band is the projection of the X-valley.

The three sub-bands observed beneath $E_F$ come from the 1ML thin Si:P $\delta$-doped layer quantum well confinement potential, which is shown in Fig. 5.5. Since the Z-valley's confinement effective mass $(m_L^*)$ is lager than the X-valley's confinement effective mass $(m_t^*)$, the 1$\Gamma$ and 2$\Gamma$ sub-bands are lower in energy than 1$\Delta$ sub-band. The crystal direction along [100] ($k_{xy}$) can see 1$\Gamma$ and 2$\Gamma$ sub-bands and 1$\Delta$ sub-band. On the other hand, the crystal direction along [110]($k_x$ and $k_y$) can only see 1$\Gamma$ and 2$\Gamma$ sub-bands.
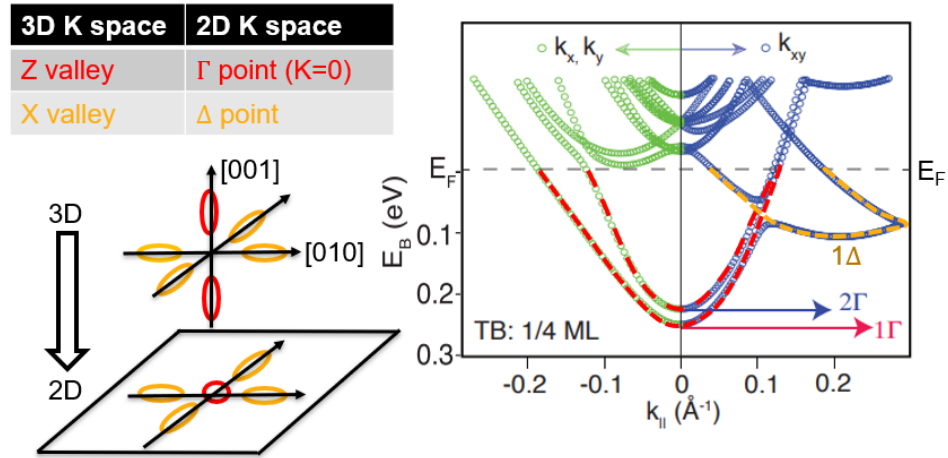


Fig. 5.4.: Electronic structure of Si:P $\delta$-doped layer. $k_{xy}$ represents the crystal direction along [100],[010],[-100], or [0-10]. $k_x$ or $k_y$ represent the crystal direction along [110], [-110], [1-10], or [-1-10]. The electronic structure is extracted from [88].
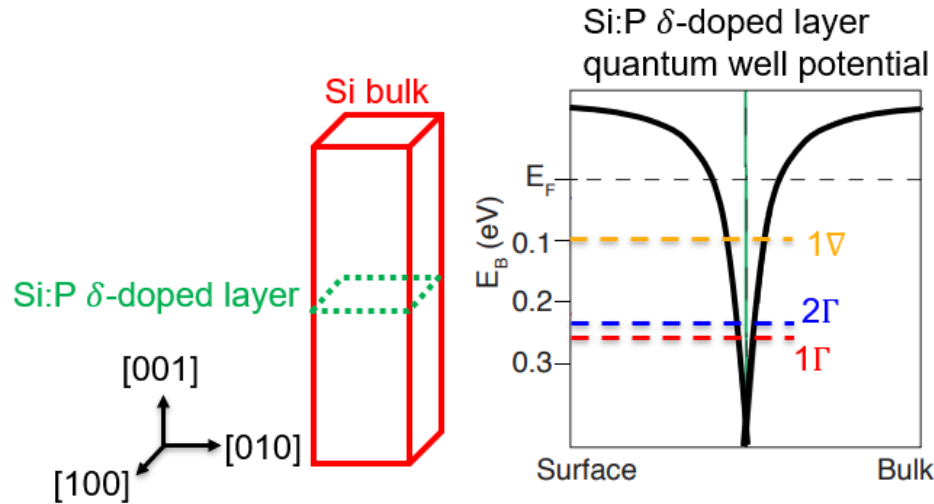
Fig. 5.5.: Schematic of the quantum well (QW) created by the Si:P $\delta$-doped layer. 1$\Gamma$, 2$\Gamma$, and 1$\Delta$ sub-bands are marked. The quantum well potential structure is extracted from [88].

### 5.3.2 Valley splitting $E_{2\Gamma} - E_{1\Gamma}$

For a Silicon ultra-thin body (UTB), if the confinement is not strong, the two $\Gamma$ sub-bands projected from the Z valleys have the same energy level and are degenerate. As the confinement increases, the interaction between the two Z valleys increases, such that the two $\Gamma$ sub-bands split. The energy difference between the two $\Gamma$ bands $(E_{2\Gamma} - E_{1\Gamma})$ is called the "valley splitting". The valley splitting is an important parameter in Silicon-based quantum computing applications. It can be used to build valley-qubit [132, 133] and is one of the dominant relaxation mechanisms [134].

Fig. 5.6 shows a schematic of the wavefunctions of the two Z valley states. The wave functions have the same envelope, but the phase is different [135]. In a strongly confined quantum well, the two valley states respond to the quantum well boundary differently. The valley splitting, therefore, varies with the width and the shape of the quantum well [136–138].
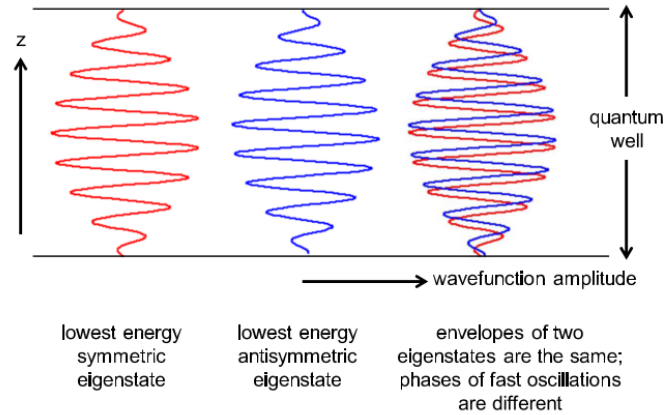
Fig. 5.6.: The two valley state wave functions projected on the Z valleys; one is symmetric and another one is asymmetric. The two wave functions have the same envelope but the phase is not the same [135]. Reprint with permission from Floris A. Zwanenburg et al., "Silicon quantum electronics", Reviews of Modern Physics. Copyright © 2013 American Physical Society.

The valley splitting in the Si:P $\delta$-doped layer is always an open question. In the empirical tight-binding simulation [121], the Si:P $\delta$-doped layer's valley splitting increases with the doping density and varies with the dopant disorder. The valley splitting calculated from the empirical tight-binding simulations varies from 5 meV to 30 meV. However, for the density-function theory (DFT) calculations, the valley splitting can be more than 100 meV and is strongly related to the choice of the function.

The first Si:P $\delta$-doped layer ARPES measurements [139, 140] reported two $\Gamma$ sub-bands beneath $E_F$. These two $\Gamma$ sub-bands were considered as two lowest $\Gamma$ sub-bands, and the valley splitting is of 132 meV. The DFT calculations using the generalized gradient approximation (GGA) explained the ARPES experiments by tuning the dopant disorder. Fig. 5.7 shows the ARPES experiments and the two DFT calculations with different dopant configurations. The valley splitting in DFT2 calculation matches

the ARPES experiment. Empirical tight-binding simulations do not show such large valley splitting.
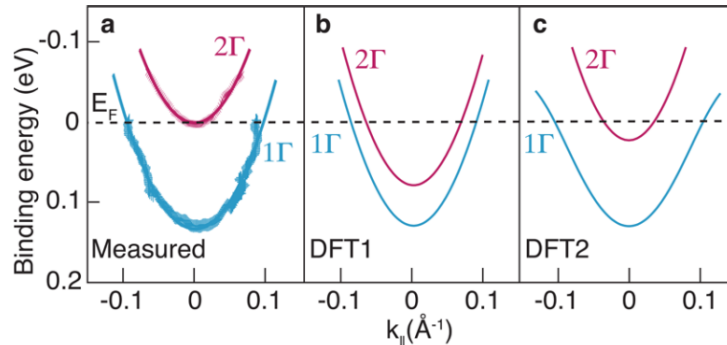


Fig. 5.7.: Previously, the ARPES experiments observed two $\Gamma$ sub-bands beneath the Fermi energy ($E_F$). The two $\Gamma$ sub-bands are considered as two valley states with the energy splitting of $\sim 132$ meV. The DFT simulation explained this large splitting by different dopant disorder where DFT1 and DFT2 are the two different dopant configurations [140]. Reprint with permission from Jill A. Miwa, Oliver Warschkow, Damien J. Carter, et al, "Valley Splitting in a Silicon Quantum Device Platform", Nano Letters. Copyright © 2014, American Chemical Society.

### 5.3.3 Orbital contribution of the $\Gamma$ sub-bands and the $\Delta$ sub-bands

In this subsection, the orbital analysis for the 1$\Gamma$ and 2$\Gamma$ sub-bands and the 1$\Delta$ sub-band of the Si:P $\delta$-doped layers is presented. The orbital contribution analysis technique is critical to understand the correlation between the simulation results and the ARPES measurements. Because, in the simulation, a large supercell needs to incorporate a correct doping density in the whole domain. This larger supercell leads to an artificial band-folding effect. While in the ARPES experiment, the electronic structure is not folded. With the orbital contribution analysis, we can distinguish whether the sub-bands at the $\Gamma$ point come from the $\Gamma$ sub-bands or the $\Delta$ sub-band.

The orbital contribution can be extracted from the eigenfunction, which consists of a ten-orbital basis (sp3d5s*). Each sub-band has the same orbital contribution unless there is the anti-crossing with other sub-bands. Fig. 5.8 shows an example of the orbital analysis on the two $\Gamma$ sub-bands and the $\Delta$ sub-band beneath $E_F$. The $1\Gamma$ and $2\Gamma$ sub-bands mainly consist of "$p_z$" and "s" orbitals while the $\Delta$ sub-band mainly consists of "$p_x$" and "s" orbitals.
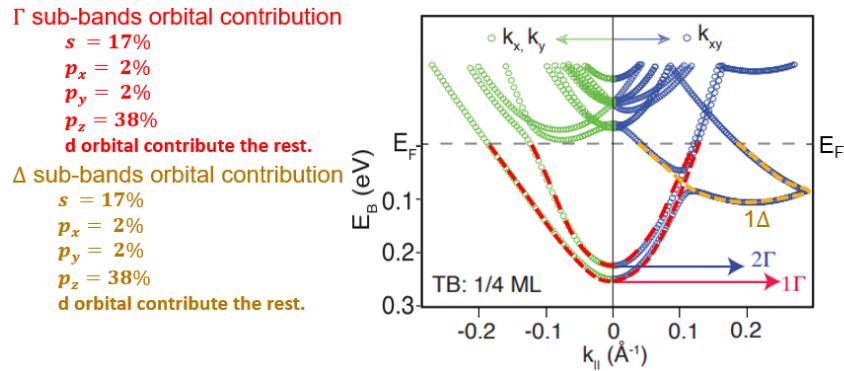


Fig. 5.8.: Orbital contribution analysis for the $\Gamma$ sub-bands and the $\Delta$ sub-band beneath $E_F$. The $\Gamma$ sub-bands have a higher percentage of $p_z$ orbitals, while the $\Delta$ sub-band has a higher percentage of $p_x$ orbital. The electronic structure is extracted from [88].

## 5.4   Third Γ sub-band in the new ARPES measurement

High-resolution angle-resolved photoemission spectroscopy (ARPES) is a commonly used technique to measure the electronic structure of a solid's surface. The high energy photon source (i.e., X-ray) is used to excite electrons out of the material's surface. Due to the law of momentum conservation, the electron density of states at different wave vectors can be measured by the electron detectors at different angles. The binding energy ($E_B$) of the electrons can also be derived from the measured kinetic energy.

In [88], the source of the photons in ARPES is improved. The resolution of the Si:P $\delta$-doped layer's electronic structure measured in [88] is better than the previous work in [139, 140]. The new measurements are shown in Fig. 5.9 where $E_B$ is the binding energy. $k_{xy}$ and $k_x/k_y$ are the high symmetry directions, which are along the crystal direction [100] and [$1\bar{1}0$]/[110], respectively. The 2D Brillouin zone projected from the bulk Silicon is shown in Fig. 5.10 where the $k_{xy}$ and $k_x/k_y$ are denoted.

In ARPES measurement shown in Fig. 5.9, the electronic structure along $k_{xy}$ has two Γ sub-bands, which is the same as the previous work [139, 140]. However, the electronic structure along $k_x/k_y$ direction has three Γ sub-bands, which is not the same as the previous ARPES experimental work [139, 140].

The previously published empirical tight-binding simulation [121] is also presented in Fig. 5.9. In the empirical tight-binding simulation, only two Γ sub-bands are observed beneath $E_F$ along the crystal directions $k_{xy}$ and $k_x/k_y$. In order to understand the third Γ sub-band observed in the new ARPES experiment data, many possible explanations have been investigated such as asymmetric doping profiles, the spin-orbit splitting, the electron-electron interactions (i.e., exchange-correlation interaction and electron screening), and the strain introduced by the Phosphorus atoms. It is found that the dielectric constant that determines the strength of the electron screening is underestimated in the published theory [121]. Once the correct dielectric constant is incorporated in the empirical tight-binding simulations, the third Γ sub-band

is observed. In the following sections, all the explored approaches listed above are detailed.
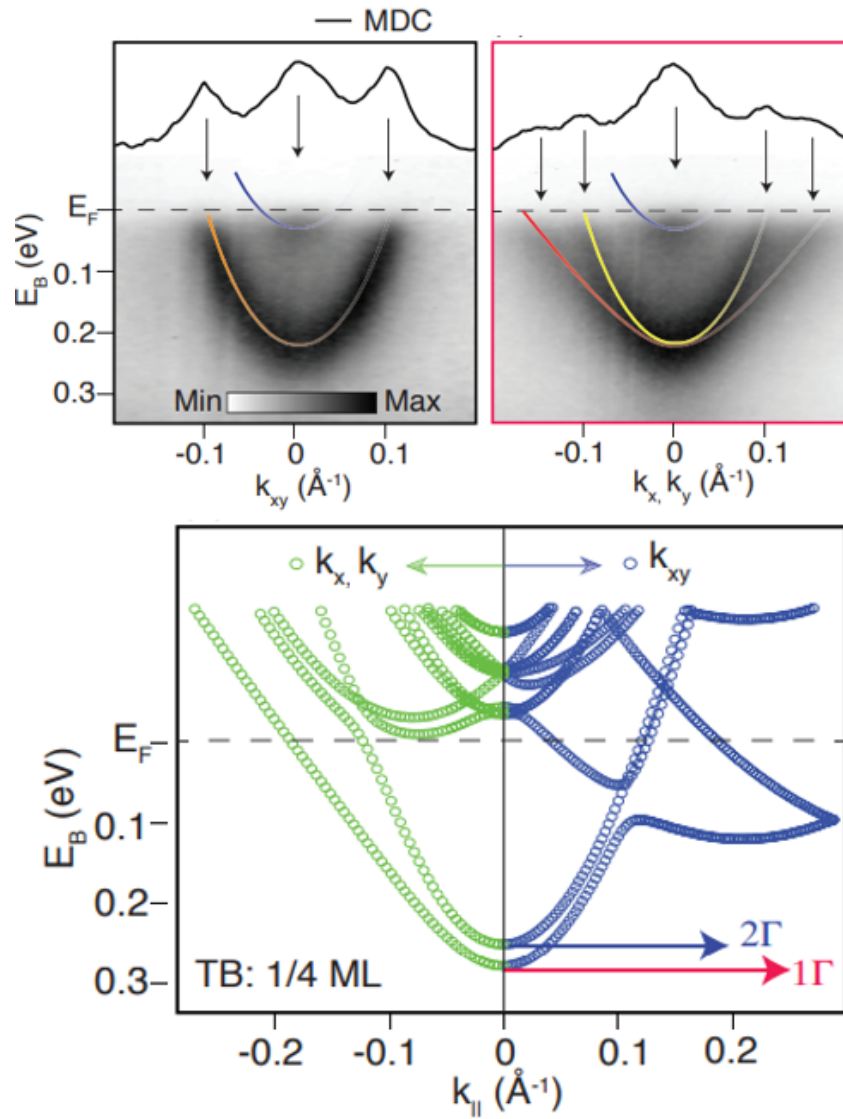


Fig. 5.9.: The most recent Si:P $\delta$-doped layer electronic structure measured by the ARPES experiment. The resolution is higher than the previous publications [139,140]. $k_{xy}$ and $k_x/k_y$ are the wave vectors along [100] and [$1\bar{1}0$]/[110], respectively. The empirical tight-binding simulation is also presented, which fails to explain the most recent ARPES experimental data. Both experimental result and the simulation result are from [88].
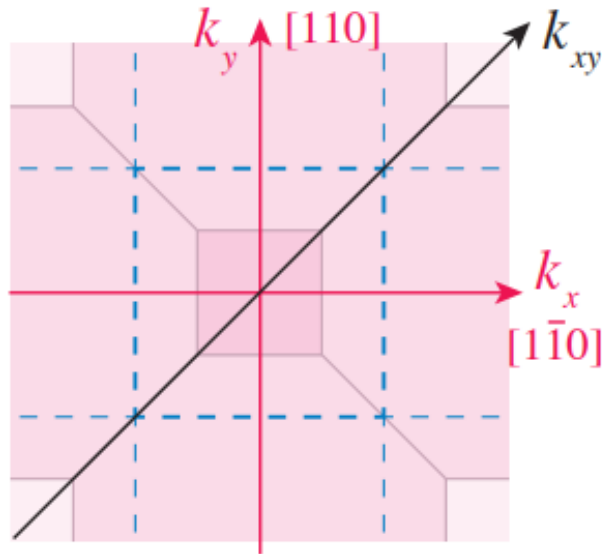
Fig. 5.10.: The 2D Brillouin zone projected from the bulk Silicon. $k_x$ and $k_y$ are along the crystal direction [110] and [1$\bar{1}$0], respectively. $k_{xy}$ is along the crystal direction [100]. The figure is extracted from [88].

## 5.5   Asymmetric doping profile

In realistic systems, Si:P $\delta$-doped layer sometimes is more than one monolayer (ML) due to process variations. The quantum well confinement of the overgrown Si:P $\delta$-doped layer is different from the ideal single monolayer Si:P $\delta$-doped layer. Such a non-ideal situation could have been one of the possible explanations for the appearance of the third $\Gamma$ sub-band. Fig. 5.11 compares the Si:P $\delta$-doped layer's electronic structure between the (a) symmetric and (b) asymmetric doping profiles. The $\Gamma$ sub-bands are identified by the orbital-contribution analysis described in Section 5.3.3. 1$\Gamma$, 2$\Gamma$, and 3$\Gamma$ sub-bands are marked with the red, blue, and black arrows, respectively. The $\Gamma$ sub-bands are projected from the Z valleys of the bulk Silicon such that the orbital-contribution is mainly the $p_z$ orbital. The other unmarked sub-bands are folded from higher wave vectors.

The asymmetric doping profile in Fig. 5.11 (b) has an extra 1/8 ML Si:P $\delta$-doped layer next to the 1/4 ML Si:P $\delta$-doped layer. The electronic structure of the asymmetric doping profile shows that $3\Gamma$ sub-band located at the energy much higher than the Fermi level ($E_F$). The reason is that although the width of the quantum well increases due to the asymmetric doping profile, the confinement increases as well due to the extra 1/8 ML Si:P $\delta$-doped layer. As a result, the asymmetric doping profile can not explain the new ARPES experimental data.
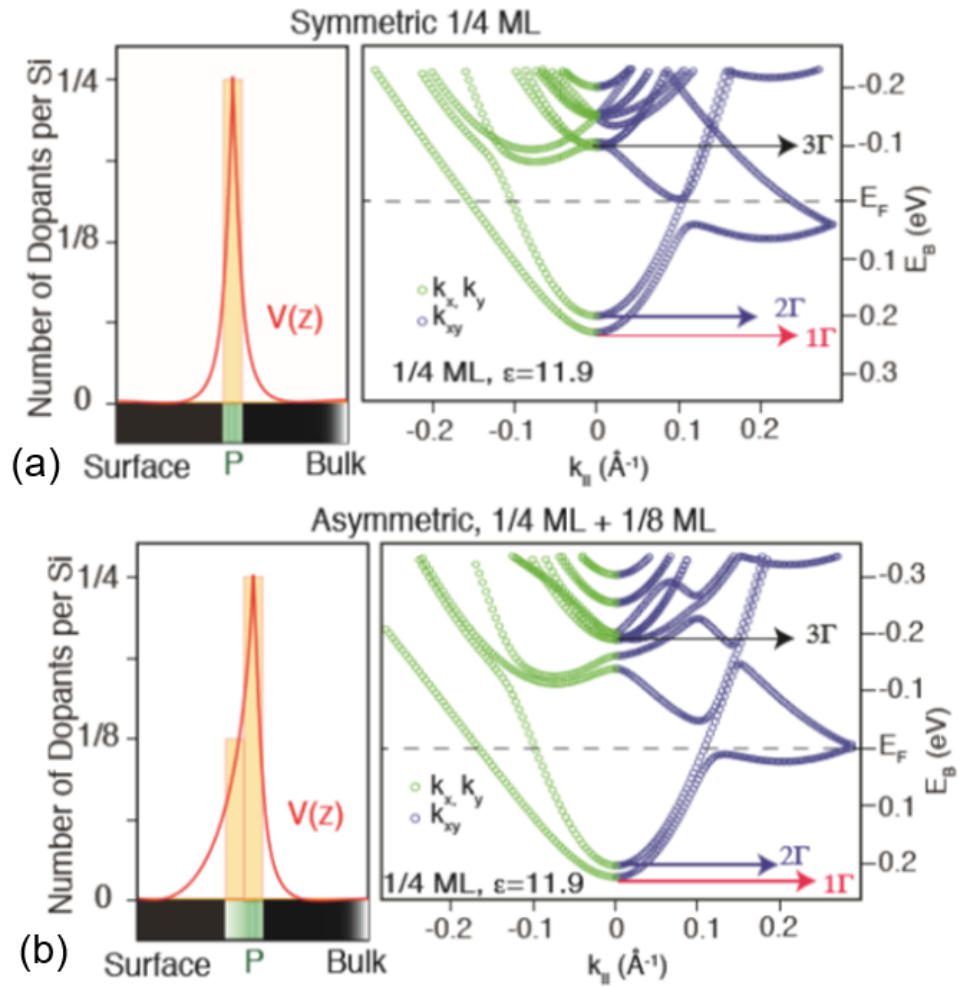
Fig. 5.11.: Si:P $\delta$-doped layer with (a) the ideal symmetric doping profile and (b) the non-ideal asymmetric doping profile. The asymmetric doping profile has a 1/8 ML Si:P $\delta$-doped layer next to a 1/4 ML Si:P $\delta$-doped layer. The figures are extracted from [88].

## 5.6 Spin splitting (Spin-orbit interaction)

For the Silicon Zincblend crystal structure, the inversion symmetry and the structural symmetry can be broken by the Si:P $\delta$-doped layer, which introduces a spin-orbit interaction. The strong spin-orbit interaction leads to a substantial spin splitting. In this section, the possibility of 1$\Gamma$ sub-band and 2$\Gamma$ sub-bands being the two spin states is investigated. The hypothetical scenario is that the spin splitting between 1$\Gamma$ and 2$\Gamma$ sub-bands is due to the strong spin-orbit interaction created by the Si:P $\delta$-doped layer. 3$\Gamma$ sub-band is the valley state of the 1$\Gamma$ sub-band and 2$\Gamma$ sub-bands.

Fig. 5.12 illustrates the hypothesis on the electronic structure measured by the ARPES experiment where (a) is along $k_{xy}$ direction while (b) is along $k_x$ or $k_y$ direction. In Fig. 5.12 (a), 1$\Gamma$ sub-band and 2$\Gamma$ sub-band along $k_{xy}$ direction are assumed on top of each other that can not be distinguished by the limit of experimental resolution. On the other hand, in Fig. 5.12 (b), 1$\Gamma$ sub-band and 2$\Gamma$ sub-band split as $k_x/k_y$ increases. This is well-known for the materials with a large spin-orbit interaction [138]. This hypothesis also suggests a large valley splitting (3$\Gamma$-1$\Gamma$) of $\sim$ 100 meV which is consistent with the previously published ARPES experimental data [139, 140].

For the effective mass model, the spin-orbit interaction is described by the Rashba spin-orbit coupling Hamiltonian [141] and the Dresselhaus spin-orbit coupling Hamiltonian [142]. The Rashba spin-orbit coupling is the result of breaking the structure inversion symmetry. On the other hand, the Dresselhaus spin-orbit coupling is the result of breaking the bulk inversion symmetry. In a Silicon quantum well, both the Rashba spin-orbit coupling and the Dresselhaus spin-orbit coupling exist [138]. The strength of the spin-orbit interaction can be described by two parameters: the Dresselhaus parameter ($\alpha$) and the Rashaba parameters ($\beta$). $\alpha$ and $\beta$ can be extracted from the spin splitting measured by experimental data or the spin splitting calculated by the atomistic simulations. The equation to extract $\alpha$ and $\beta$ are
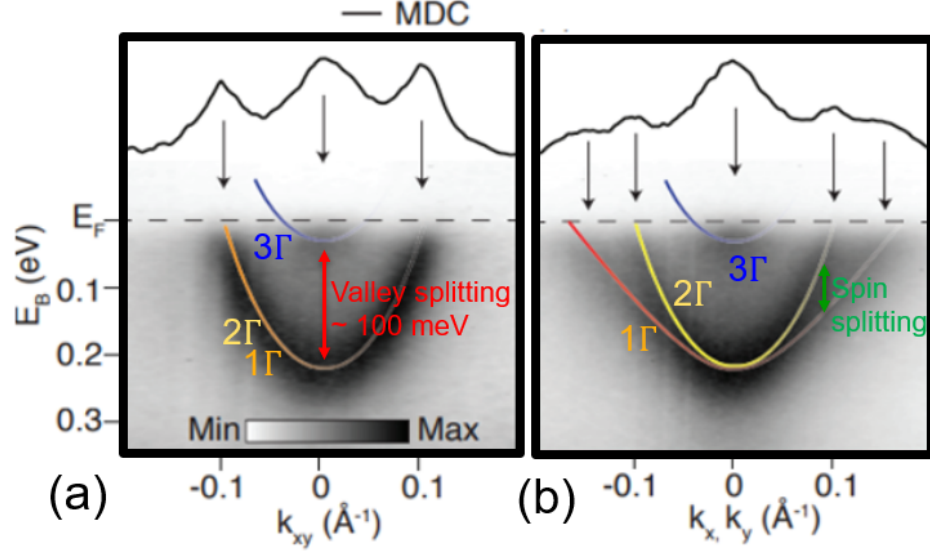
Fig. 5.12.: Electronic structure measured by APRES along (a) $k_{xy}$ and (b) $k_x k_y$ direction. The 1Γ, 2Γ, and 3Γ sub-bands are marked based on the assumption that 1Γ sub-band and 2Γ sub-band are two spin states while 3Γ sub-band is the valley state. The momentum distribution curve (MDC) along the Fermi surface is also displayed. The figure is extracted from [88].

$$\alpha = \lim_{k \to 0} \frac{\triangle_{SO}(k \parallel [110]) + \triangle_{SO}(k \parallel [1-10])}{4|k|}$$
$$\beta = \lim_{k \to 0} \frac{\triangle_{SO}(k \parallel [110]) - \triangle_{SO}(k \parallel [1-10])}{4|k|}$$

(5.1)

where $\triangle_{SO}(k \parallel [110])$ is the spin splitting at the wave vector k along the crystal direction [110] while $\triangle_{SO}(k \parallel [1-10])$ is the spin splitting at the wave vector k along the crystal direction [1-10] [138].

In the empirical atomistic tight-binding simulation, the spin-orbit interaction can be included by using the spin-resolved "sp3d5s*-so" 20-band basis. The Rashba spin-orbit coupling, the Dresselhaus spin-orbit coupling, and even higher-order spin-orbit coupling are all being considered in the simulation. Fig. 5.13 (a) is the spin splitting of the first sub-band along crystal directions of [110] and [1-10]. The spin splittings

in both crystal directions [110] and [1-10] are less than 1 meV. Furthermore, the spin splitting extracted along the crystal direction [100] is even smaller than the spin splitting extracted along the crystal direction [110] and [1-10] [138]. As a result, the hypothesis that 1Γ sub-band and 2Γ sub-band are spin splitting can not be true.

For future reference, the Rashba parameter and the Dresselhaus parameter for the Si:P $\delta$-doped layer are calculated using Eq. 5.1 and are shown in Fig. 5.13 (b). The Dresselhaus parameter ($\alpha$) is larger than the Rashba parameter ($\beta$) as suggested in [138].
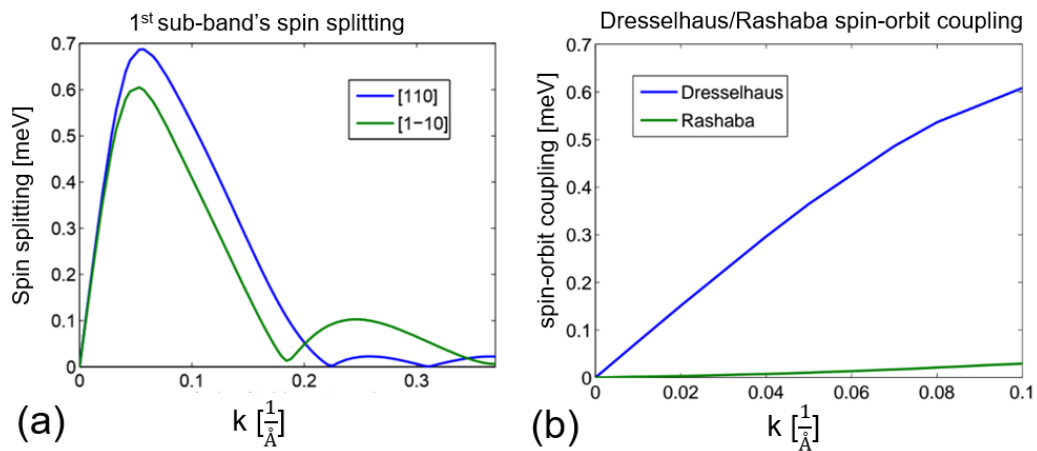


Fig. 5.13.: (a) The first sub-band's spin splitting and (b) the spin-orbit interaction parameters extracted from the Si:P $\delta$-doped layer's electronic structure calculated by the atomistic tight-binding simulations.

## 5.7 Electron-electron interaction

### 5.7.1 Overview

The doping density in the Si:P $\delta$-doped layer is in the order of $\sim 10^{14}\ cm^{-3}$, the electron density is therefore extremely high. A strong electron-electron interaction is anticipated in such a material system. In this section, another hypothesis assuming that 1Γ sub-band and 2Γ sub-band are the two valley states while the 3Γ sub-band is another sub-band at higher energy is investigated. It is assumed that the strength of the electron-electron interaction in the current empirical tight-binding simulation is not correct is could be the reason for the 3Γ sub-band to be missing from the simulation results. The hypothetical scenario is depicted in the ARPES experimental data shown in Fig. 5.14.
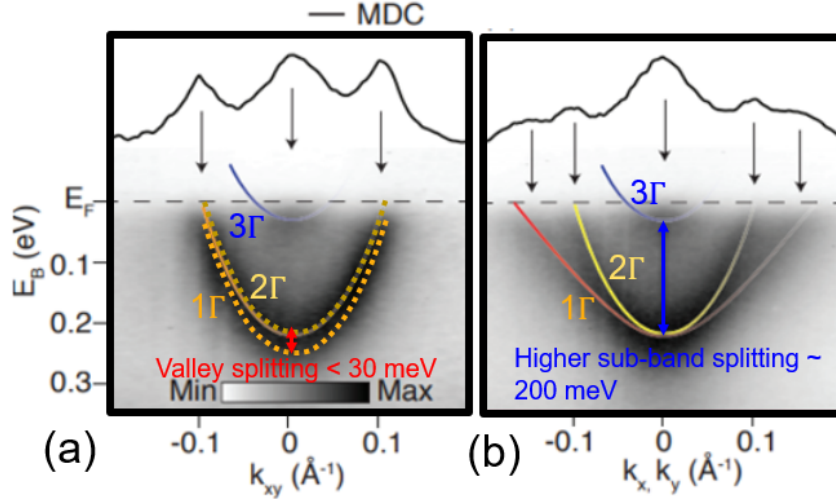


Fig. 5.14.: Electronic structure measured by APRES along (a) $k_{xy}$ and (b) $k_x k_y$ direction. The 1Γ, 2Γ, and 3Γ sub-bands are marked based on the assumption that 1Γ sub-band and 2Γ sub-band are two valley states while 3Γ sub-band is another sub-band at higher energy. The momentum distribution curve (MDC) along the Fermi surface is also marked. The figure is extracted from [88].

Fig. 5.14 (a) and (b) show the electronic structure measured in the ARPES experiment along $k_{xy}$ and $k_x k_y$ directions, respectively. The 1Γ, 2Γ, and 3Γ sub-bands are marked to illustrate the hypothetical scenario proposed in this section. For the electronic structure along $k_{xy}$ direction, the valley splitting between 1Γ sub-band and 2Γ sub-band is very small and can not be distinguished in the experimental data. The resolution of the current ARPES experiment is $\sim$ 30 meV. We assume the valley splitting between 1Γ sub-band and 2Γ sub-band is less than 30 meV. On the other hand, for the electronic structure along $k_x k_y$ direction, the energy splitting between 1Γ sub-band and 2Γ sub-band increases with $k_x k_y$. The 3Γ sub-band is at the same energy level in the electronic structures along both $k_{xy}$ and $k_x k_y$ directions. The energy splitting between 3Γ sub-band and 1Γ/2Γ sub-bands is 200 meV.

## 5.7.2   Simulation method overview

In the current empirical tight-binding calculation framework [34], the electron-electron interaction is considered by imposing an effective potential in the tight-binding Hamiltonian using the Hartree-Fock approximation [143].

$$\left(H_{TB} + V_{eff}(r; n)\right) \psi_i(r) = \epsilon_i \psi_i(r) \tag{5.2}$$

where $H_{TB}$ is the effective Hamiltonian constructed using the empirical tight-binding basis and $V_{eff}$ is the effective potential that describes the electron-electron interaction. $\psi_i(r)$ and $\epsilon_i$ are the eigenfunction and the eigenenergy at state "i". The effective potential ($V_{eff}$) consists of three terms: $V_{ext}$, $V_D$, and $V_{XC}$ as shown in Eq. 5.3.

$$V_{eff}(r; n) = V_{ext}(r) + V_D(r; n) + V_{XC}(r; n) \tag{5.3}$$

where $V_{ext}(r)$ is the external potential introduced by the ionized Phosphorus atoms with each Phosphorus atom assumed to be a Coulomb potential. $V_D(r; n)$ is the displacement field potential that describes the electron-electron Coulombic repulsion. $V_{XC}(r; n)$ is the potential introduced by the electron-electron exchange-correlation.

The displacement field potential $(V_D)$ is obtained from Eq. 5.4.

$$\nabla^2 V_D(r) = -e^2 \left[n(r) - n_0(r)\right]/\varepsilon_r \tag{5.4}$$

where $n_0(r)$ is the spatial distribution of the fixed charges in the system which is determined by the number of Phosphorus atoms and their location, $n(r)$ is the spatial distribution of the free electrons obtained from the eigenfunctions $(\psi_i(r))$. $e$ is the charge of an electron, and $\varepsilon_r$ is the dielectric constant of the host material, which is Silicon in the Si:P $\delta$-doped layer material system.

The system is assumed electrically neutral so that the number of the free electrons is the same as the number of the Phosphorus atoms. In this calculation, the Hartree-Fock theory is applied, and the multi-electron anti-symmetric wave function is approximated as a single Slater determinant. The Fermi-level $(E_F)$ is determined by filling up the density of states to reach the requirement on the number of the free electrons. The eigenfunction $(\psi_i(r))$ with it's eigenenergy $(\epsilon_i)$ below the Fermi-level $(E_F)$ is occupied by the free electrons. The spatial distribution of the free electrons $(n(r))$ can be obtained by Eq. 5.5.

$$n(r) = \sum_{i=0}^{N} |\psi_i(r)|^2,$$
$$where \ \epsilon_i < E_F \tag{5.5}$$

where $\psi_i(r)$ is the eigenfunction that is filled by the free electrons, and N is the total number of eigenfunctions $(\psi_i(r))$ with eigenenergies $(\epsilon_i)$ below the Fermi-level $(E_F)$.

On the other hand, the electron-electron exchange-correlation potential $(V_{XC})$ consists of two terms: (1) the potential introduced by the exchange interaction $(V_{exch})$ and (2) the potential introduced by the correlation $(V_{corr})$. The expression of $V_{XC}$ is shown in Eq. 5.6.

$$V_{XC}(n(r)) = \alpha \left[V_{exch}\left[n(r)\right] + V_{corr}\left[n(r)\right]\right], \tag{5.6}$$

where $\alpha$ is an empirical parameter to fine tune the strength of $V_{XC}$ to match experimental data. Both $V_{exch}$ and $V_{corr}$ are functions of free electron spatial distribution $(n(r))$. The empirical expression of $V_{exch}$ and $V_{corr}$ are shown in Eq. 5.7.

$$
\begin{aligned}
V_{exch}\left[n(r)\right] &= -\left(\frac{e^2}{4\pi\varepsilon_r}\right)\left(\frac{3n(r)}{8\pi}\right)^{1/3}, \\
V_{corr}\left[n(r)\right] &= -\left(\frac{e^2}{4\pi\varepsilon_r}\right)\frac{C_1 n(r)^{1/3} + C_2 n(r)^{2/3}}{\left[C_3 + n(r)^{1/3}\right]^2}
\end{aligned}
\tag{5.7}
$$

where $C_1$, $C_2$, and $C_3$ are $0.055/\text{Å}^2$, $0.104/\text{Å}$, and $0.339/\text{Å}$, respectively [143].

### 5.7.3 Exchange-correlation ($V_{XC}$)

The electronic structure of Si:P $\delta$-doped layer calculated with the empirical tight-binding simulation uses the Hartree-Fock method to include electron-electron interaction. The Coulombic interaction is considered with displacement field potential ($V_D$), and the exchange-correlation is considered with the exchange-correlation potential ($V_{XC}$). The local density approximation (LDA) is assumed to obtain the exchange-correlation interaction where the the exchange-correlation interaction is a function of electron spatial distribution [144].

The equation of the electron-electron exchange-correlation interaction is shown here again as a reminder:

$$
V_{XC}(n(r)) = \alpha\left[V_{exch}\left[n(r)\right] + V_{corr}\left[n(r)\right]\right],
\tag{5.8}
$$

In this section, the changes to the electronic structure of the Si:P $\delta$-doped layer with the emperical parameter ($\alpha$) for the electron-electron exchange-correlation interaction is explored.

Fig. 5.15 shows the electronic structure of Si:P $\delta$-doped layer calculated using different exchange-correlation empirical parameters ($\alpha$): (a) is $\alpha=0$, (b) is $\alpha=1$, (c) is $\alpha=1.5$, and (d) is $\alpha=5$. $1\Gamma$, $2\Gamma$, and $3\Gamma$ sub-bands are identified using the orbital analysis described in Sec. 5.3.3. Fig. 5.15 (a), (b), (c), and (d) all show that $3\Gamma$

sub-band is above the Fermi-level ($E_F$) that none of these electronic structures are able to explain the ARPES experimental data.

In Fig. 5.15 (a), when $\alpha$=0, 3$\Gamma$ sub-band is getting closer to the Fermi-level ($E_F$) as compared to Fig. 5.15 (b), (c), and (d) for $\alpha$=1, 1.5, and 5. In the previous publication [121], the empirical parameter for exchange-correlation ($\alpha$) is set to 1. Reducing the empirical parameter for exchange-correlation ($\alpha$) lowers the higher energy sub-bands (i.e., 3$\Gamma$ sub-band) and gives an electronic structure that is closer to the ARPES experimental data. This suggests that electron-electron exchange-correlation interaction may have been overestimated or the effect of electron-electron Coulomic repulsion is underestimated, which is the opposite of the electron-electron exchange-correlation interaction.

Fig. 5.16 shows the sub-band energy difference between 3$\Gamma$ sub-band and 1$\Gamma$ sub-band (3$\Gamma$-1$\Gamma$), and the energy difference between 1$\Delta$ sub-band and 1$\Gamma$ sub-band (1$\Delta$-1$\Gamma$). Different electron-electron exchange-correlation interaction empirical parameters ($\alpha$) are used in the simulation to extract the the energy difference of the sub-bands. The energy difference between 2$\Gamma$ sub-band and 1$\Gamma$ sub-band is of $\sim$ 20 meV which is not listed in Fig. 5.16 since it does not change with the electron-electron exchange-correlation interaction empirical parameter ($\alpha$).

The energy difference of sub-bands 3$\Gamma$-1$\Gamma$ and 1$\Delta$-1$\Gamma$ reduces as the electron-electron exchange-correlation interaction empirical parameter ($\alpha$) decreases. It must be noted that the negative value of $\alpha$ tested here is for the numerical experimental purpose only and has no physical meaning. $\alpha < 0$ means that the electron-electron Coulombic repulsion interaction is underestimated and the electron-electron screening should be increased to match the ARPES experimental data. In the next section, we explore how the Si:P $\delta$-doped layer's electronic structure changes with the electron-electron screening.
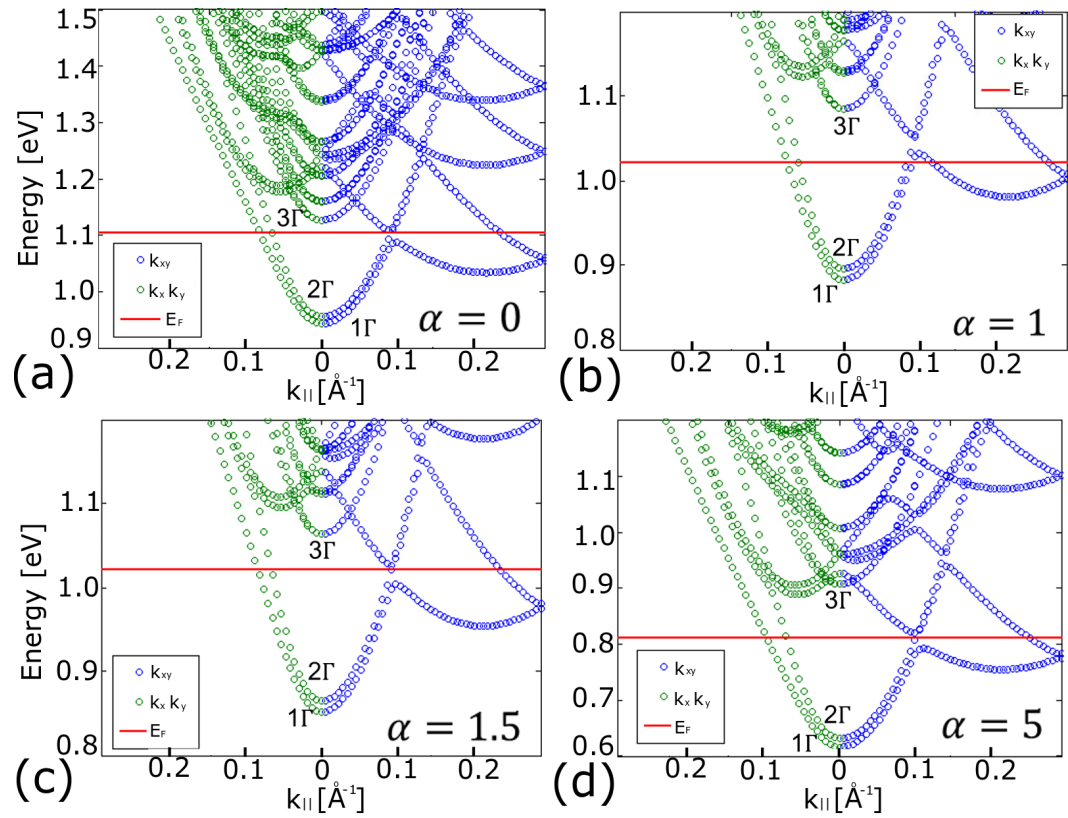
Fig. 5.15.: Si:P $\delta$-doped layer's electronic structure calculated for different exchange-correlation interaction empirical parameter ($\alpha$) (a) $\alpha$=0, (b) $\alpha$=1, (c) $\alpha$=1.5, and (d) $\alpha$=5. 1$\Gamma$, 2$\Gamma$, and 3$\Gamma$ sub-bands are identified and marked using the orbital analysis described in Sec. 5.3.3.
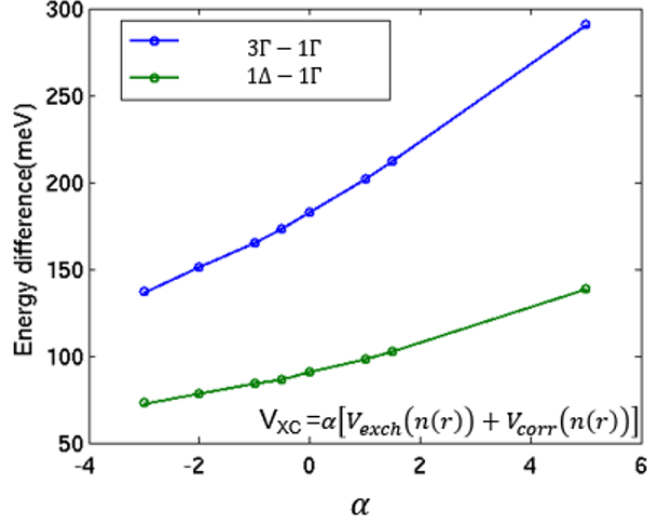
Fig. 5.16.: Energy differences 3Γ sub-band - 1Γ sub-band and 1Δ sub-band - 1Γ sub-band with different electron-electron exchange-correlation interaction empirical parameters ($\alpha$) used in the simulation.

### 5.7.4 Electron Coulombic repulsion interaction ($V_D$)

The electron-electron Coulombic repulsion interaction is related to the electron screening effect in a material system. The displacement field potential introduced by the electron-electron Coulombic repulsion interaction is shown here again as a reference:

$$\nabla^2 V_D(r) = -e^2 \left[n(r) - n_0(r)\right]/\varepsilon_r \qquad (5.9)$$

Solving the displacement field potential is equivalent to solving the Poisson equation. In the empirical tight-binding simulation framework, since only the "donor electrons" are considered in the self-consistent calculation, the dielectric constant ($\varepsilon_r$) used here should represent the screening in the host material. In the previous publication [121], the dielectric constant is assumed 11.9 which corresponds to the dielectric constant of the Silicon host material. In this section, we investigate how the dielectric constant ($\varepsilon_r$) changes the Si:P $\delta$-doped layer's electronic structure.

Fig. 5.17 shows the Si:P $\delta$-doped layer's electronic structures calculated by the empirical tight-binding method with different dielectric constants ($\varepsilon_r$) used in the displacement field potential ($V_D$). Fig. 5.17 (a) uses $\varepsilon_r = 11.9$, (b) is $\varepsilon_r = 14$, (c) is $\varepsilon_r = 20$, and (d) is $\varepsilon_r = 40$. $1\Gamma$, $2\Gamma$, and $3\Gamma$ sub-bands are identified using the orbital analysis described in Sec. 5.3.3. When the dielectric constant ($\varepsilon_r$) increases, the $3\Gamma$ sub-band's energy level reduces. For electronic structure calculated using the dielectric constant ($\varepsilon_r$) of 20, $3\Gamma$ sub-band is beneath the Fermi-level($E_F$) that is close to the ARPES experimental data. On the other hand, for electronic structure calculated using the dielectric constant ($\varepsilon_r$) of 40, the $3\Gamma$ sub-band is too close $1\Gamma$ sub-band that is not the case in the ARPES experimental data.
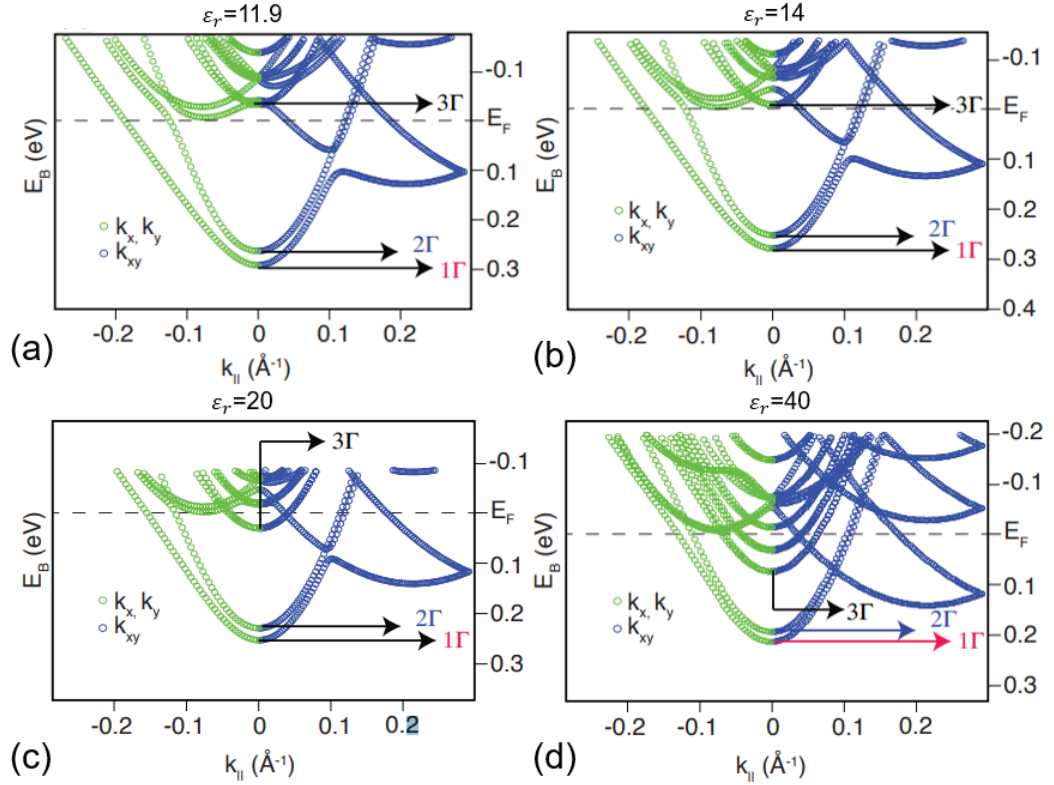


Fig. 5.17.: Electronic structure of Si:P $\delta$-doped layer calculated with the empirical tight-binding method using different dielectric constant ($\varepsilon_r$) (a) $\varepsilon_r = 11.9$, (b) $\varepsilon_r = 14$, (c) $\varepsilon_r = 20$, and (d) $\varepsilon_r = 40$. $1\Gamma$, $2\Gamma$, and $3\Gamma$ sub-bands are identified and marked using the orbital analysis described in Sec. 5.3.3. The figures are extracted from [88].

Fig. 5.17 shows the binding energies of 1Γ, 2Γ, and 3Γ sub-bands extracted from the empirical tight-binding simulation calculated using different dielectric constant ($\varepsilon_r$). For a dielectric constant of 20, the binding energies of 1Γ, 2Γ, and 3Γ sub-bands match the ARPES experimental data.
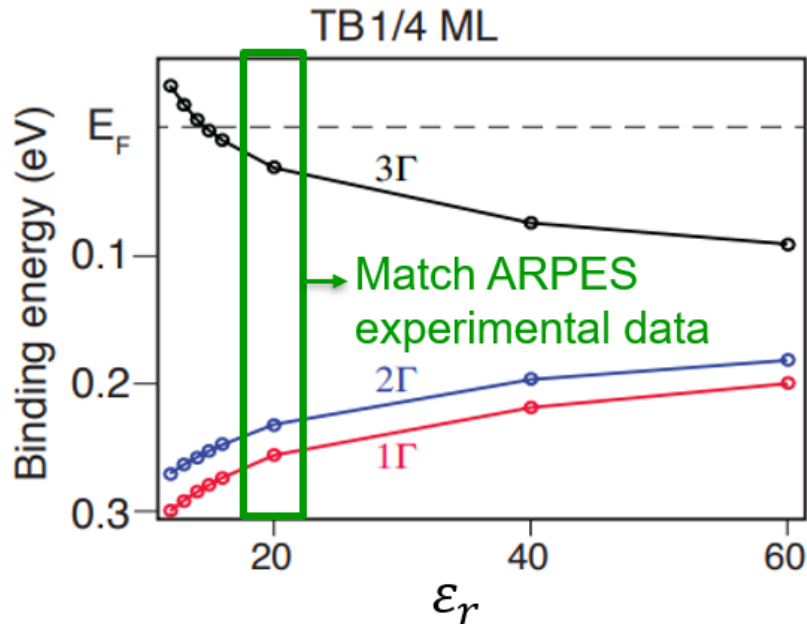


Fig. 5.18.: Binding energies of 1Γ, 2Γ, and 3Γ sub-bands extracted from the empirical tight-binding simulation calculated using different dielectric constant ($\varepsilon_r$). For $\varepsilon_r = 20$, the binding energies of 1Γ, 2Γ, and 3Γ sub-bands match the ARPES experimental data. The figure is extracted from [88].

Fig. 5.19 shows the electronic structure comparison for (a) the ARPES experimental data and (b) the empirical tight-binding simulation calculated using a dielectric constant ($\varepsilon_r$) of 20. 1Γ, 2Γ, and 3Γ sub-bands are identified using the orbital analysis described in Sec. 5.3.3. In the empirical tight-binding simulation, three Γ sub-bands (1Γ, 2Γ, and 3Γ) are observed below the Fermi-level ($E_F$) which matches the ARPES experimental data. Fig. 5.20 (a) shows the overlap between the APRES experimental data and the empirical tight-binding simulation along $k_x, k_y$ direction. The curvature of 1Γ and 2Γ sub-band obtained from the ARPES experimental data is similar to the

curvature obtained by the empirical tight-binding simulation. The energy difference for each $\Gamma$ sub-band is also listed. The energy difference for each $\Gamma$ sub-band extracted from the APRES experimental data is similar to the result from the empirical tight-binding simulation.
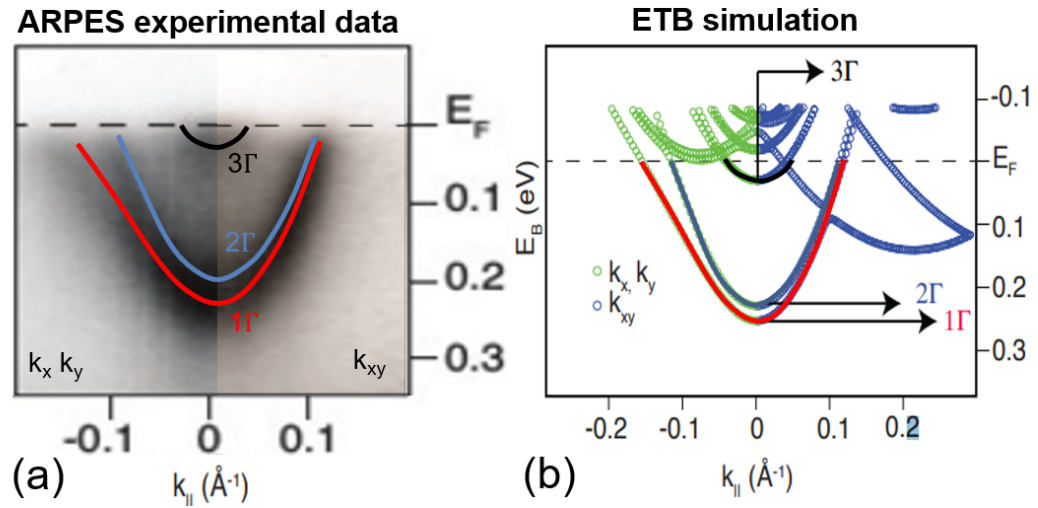


Fig. 5.19.: Comparison of Si:P $\delta$-doped layer's electronic structure obtained from (a) the ARPES experimental data and (b) the empirical tight-binding simulation using a dielectric constant ($\varepsilon_r$) of 20. The ETB simulation is calculated with $\varepsilon_r = 20$. $1\Gamma$, $2\Gamma$, and $3\Gamma$ sub-bands are identified and marked using the orbital analysis described in Sec. 5.3.3. The figures are extracted from [88].
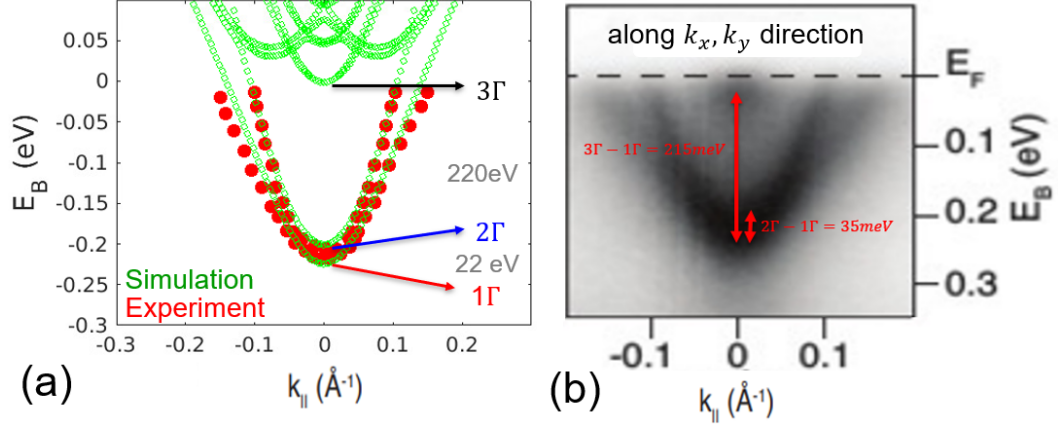
Fig. 5.20.: Comparison of the Si:P $\delta$-doped layer's electronic structure along $k_x, k_y$ direction obtained from (a) the empirical tight-binding simulation and (b) the ARPES experimental data. The energy difference between each sub-bands and the curvatures of the sub-bands are similar for the ARPES experimental data and the empirical tight-binding simulation. The figures are extracted from [88].

## 5.8  1$\Delta$ sub-band

The empirical tight-binding calculation in section 5.7 shows three $\Gamma$ sub-bands below the Fermi-levels, similar to the sub-bands observed in the ARPES experimental data. However, 1$\Delta$ sub-band in the empirical tight-binding calculation is not observed in the ARPES experimental data. This was the only discrepancy between the ARPES experimental data and the empirical tight-binding simulation. Three years since the first draft of this work, a new ARPES experiment presented in [145] shows the observation of 1$\Delta$ sub-band. In the first ARPES experiment, the $\Gamma$ sub-bands and the $\Delta$ sub-bands were not resolved with the same photon energy. The photon energy used to acquire 1$\Delta$ sub-band is $\sim$80 eV while the photon energy used to acquire the $\Gamma$ sub-bands is $\sim$110 eV [145].

Fig. 5.21 (a) and (b) show the electronic structure of the Si:P $\delta$-doped layer obtained from the ARPES experimental data and the empirical tight-binding calculation. The ARPES experimental data is extracted from [145] and the the empirical

tight-binding calculation for [88]. In Fig. 5.21 (a), 1Γ sub-band, 2Γ sub-band, and 1Δ sub-band are observed. Since 3Γ sub-band is close to the Fermi-level, in [145], the 3Γ sub-band is not observed due to process variation. In Fig. 5.21 (b), the empirical tight-binding calculation predicts the existance of 1Δ bands before the ARPES experiment.
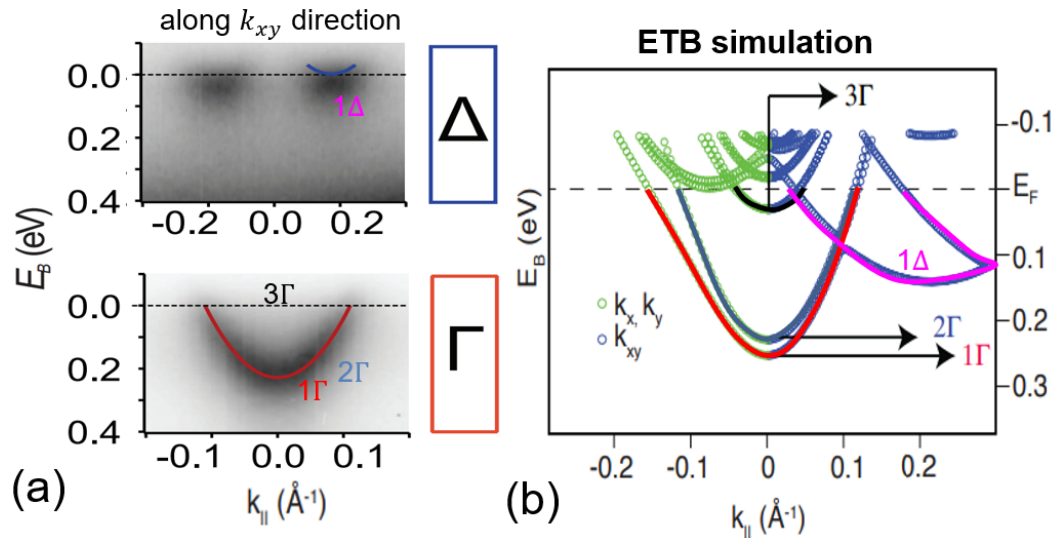


Fig. 5.21.: Electronic structure of the Si:P δ-doped layer obtained from (a) the ARPES experimental data [145] and (b) the empirical tight-binding calculation. 1Γ, 2Γ, 3Γ, and 1Δ sub-bands are identified and marked with the orbital analysis method described in Sec. 5.3.3. The experiment result shown in (a) is extracted from [145]. The simulation data shown in (b) is extracted from [88].

## 5.9 Summary

Different physical mechanisms are investigated with the empirical tight-binding simulation to explain the electronic structure of Si:P $\delta$-doped layer measured in the ARPES experiment. The empirical tight-binding simulation explains the 1$\Gamma$, 2$\Gamma$, and 3$\Gamma$ sub-bands and predicts the existence of 1$\Delta$ sub-band that is reported in a latter experimental work. The empirical tight-binding simulation matches the ARPES experimental data in various aspects such as valley splitting (2$\Gamma$-1$\Gamma$), energy splitting of higher sub-band (3$\Gamma$-1$\Gamma$), and the curvature of the sub-bands along different directions ($k_{xy}$ and $k_x, k_y$). It is found that the dielectric constant $\varepsilon_r$ of the Si:P $\delta$-doped layer $\varepsilon_r \sim$ should be 20. This improves the accuracy of the electrostatic modeling for the Si:P $\delta$-doped layer for donor-based quantum computing devices.

REFERENCES

# REFERENCES

[1] C. Qiu, F. Liu, L. Xu, B. Deng, M. Xiao, J. Si, L. Lin, Z. Zhang, J. Wang, H. Guo, H. Peng, and L.-M. Peng, "Dirac-source field-effect transistors as energy-efficient, high-performance electronic switches," *Science*, vol. 361, no. 6400, pp. 387–392, 2018. [Online]. Available: https://science.sciencemag.org/content/361/6400/387

[2] L. Chang, D. J. Frank, R. K. Montoye, S. J. Koester, B. L. Ji, P. W. Coteus, R. H. Dennard, and W. Haensch, "Practical strategies for power-efficient computing technologies," *Proceedings of the IEEE*, vol. 98, no. 2, pp. 215–236, Feb 2010.

[3] "CPU power dissipation," [Online] https://en.wikipedia.org/wiki/CPU_power_dissipation.

[4] Intel Corporation, "Enhanced Intel Speed Step Technology for the Intel Pentium M Processor (White Paper)," 2014 March, Archived Date:08/12/2015; https://web.archive.org/web/20150812030010/http://download.intel.com/design/network/papers/30117401.pdf.

[5] B. Hoefflinger, "ITRS 2028International Roadmap of Semiconductors," DOI:10.1007/978-3-319-22093-2_7.

[6] "International Technology Roadmap for Semiconductors (ITRS)," 2015. [Online]. Available: http://www.itrs2.net/

[7] Gonzalez, R. and Gordon, B.M. and Horowitz, M.A., "Supply and threshold voltage scaling for low power CMOS," *IEEE Journal of Solid-State Circuits*, vol. 32, no. 8, pp. 1210–1216, 1997.

[8] "International Technology Roadmap for Semiconductors." [Online]. Available: https://en.wikipedia.org/wiki/International_Technology_Roadmap_for_Semiconductors

[9] "International technology roadmap for semiconductors (itrs)," 2011, (Date of access:4/3/2016). [Online]. Available: http://www.itrs2.net/itrs-reports.html

[10] M. Bohr, "Intel's Revolutionary 22 nm Transistor Technology," 2011. [Online]. Available: http://download.intel.com/newsroom/kits/22nm/pdfs/22nm-Details_Presentation.pdf

[11] E. Memisevic, J. Svensson, M. Hellenbrand, E. Lind, and L.-E. Wernersson, "Vertical InAs/GaAsSb/GaSb tunneling field-effect transistor on Si with SS = 48 mV/decade and Ion = 10 $\mu$A/$\mu$m for Ioff = 1 nA/$\mu$m at Vds = 0.3 V," *2016 IEEE International Electron Devices Meeting (IEDM)*, pp. 19.1.1–19.1.4, 2016, doi:10.1109/IEDM.2016.7838450.

[12] E. Memisevic, J. Svensson, E. Lind, and L. E. Wernersson, "InAs/InGaAsSb/GaSb Nanowire Tunnel Field-Effect Transistors," *IEEE Transactions on Electron*, vol. 64, no. 11, pp. 4746–4751, 2017, doi:10.1109/TED.2017.2750763, isbn:0018-9383 1557-9646, issn:00189383.

[13] Memisevic, Elvedin and Svensson, Johannes and Lind, Erik and Wernersson, Lars Erik, "Vertical Nanowire TFETs with Channel Diameter Down to 10 nm and Point $S_{min}$ of 35 mV/Decade," *IEEE Electron Device Letters*, vol. 39, no. 7, pp. 1089–1091, 2018, doi:10.1109/LED.2018.2836862, issn:07413106.

[14] D. K. Mohata, R. Bijesh, S. Mujumdar, C. Eaton, R. Engel-Herbert, T. Mayer, V. Narayanan, J. M. Fastenau, D. Loubychev, A. K. Liu, and S. Datta, "Demonstration of MOSFET-like on-current performance in arsenide/antimonide tunnel FETs with staggered hetero-junctions for 300mV logic applications," in *2011 International Electron Devices Meeting*, Dec 2011, pp. 33.5.1–33.5.4, doi:10.1109/IEDM.2011.6131665.

[15] S. Sant, K. Moselund, S. Member, D. Cutaia, S. Member, H. Schmid, M. Borg, H. Riel, S. Member, and A. Schenk, "Lateral InAs/Si p-Type Tunnel FETs Integrated on Si. Part 1: experiment and device," *IEEE Transactions on Electron Devices*, vol. 63, no. 11, pp. 4240–4247, 2016, doi:10.1109/TED.2016.2612484, issn:0018-9383.

[16] J. Appenzeller, Y.-M. Lin, J. Knoch, and P. Avouris, "Band-to-Band Tunneling in Carbon Nanotube Field-Effect Transistors," *Phys. Rev. Lett.*, vol. 93, p. 196805, Nov 2004, doi:10.1103/PhysRevLett.93.196805. [Online]. Available: https://link.aps.org/doi/10.1103/PhysRevLett.93.196805

[17] J. Appenzeller, Y. M. Lin, J. Knoch, Z. Chen, and P. Avouris, "Comparing carbon nanotube transistors - the ideal choice: A novel tunneling device design," *IEEE Transactions on Electron Devices*, vol. 52, no. 12, pp. 2568–2576, 2005.

[18] W. Y. Choi, B. Park, J. D. Lee, and T. K. Liu, "Tunneling Field-Effect Transistors (TFETs) With Subthreshold Swing (SS) Less Than 60 mV/dec," *IEEE Electron Device Letters*, vol. 28, no. 8, pp. 743–745, Aug 2007, doi:10.1109/LED.2007.901273.

[19] A. M. Ionescu and H. Riel, "Tunnel field-effect transistors as energy-efficient electronic switches," *Nature*, vol. 479, no. 7373, pp. 329–337, 2011, doi:10.1038/nature10679.

[20] Seabaugh, Alan C. and Zhang, Qin, "Low-voltage tunnel transistors for beyond CMOS logic," *Proceedings of the IEEE*, vol. 98, no. 12, pp. 2095–2110, 2010.

[21] U. E. Avci, D. H. Morris, and I. A. Young, "Tunnel field-effect transistors: Prospects and challenges," *IEEE Journal of the Electron Devices Society*, vol. 3, no. 3, pp. 88–95, 2015, doi:10.1109/JEDS.2015.2390591.

[22] P. A. M. Dirac and R. H. Fowler, "On the theory of quantum mechanics," *Proceedings of the Royal Society of London. Series A, Containing Papers of a Mathematical and Physical Character*, vol. 112, no. 762, pp. 661–677, 1926. [Online]. Available: https://royalsocietypublishing.org/doi/abs/10.1098/rspa.1926.0133

[23] T. A. Ameen, H. Ilatikhameneh, G. Klimeck, and R. Rahman, "Few-layer Phosphorene: An Ideal 2D Material For Tunnel Transistors," *Scientific Reports*, vol. 6, pp. 28 515 EP –, Jun 2016, article. [Online]. Available: http://dx.doi.org/10.1038/srep28515

[24] H. Ilatikhameneh, G. Klimeck, J. Appenzeller, and R. Rahman, "Design rules for high performance tunnel transistors from 2-D materials," *IEEE Journal of the Electron Devices Society*, vol. 4, no. 5, pp. 260–265, 2016, doi:10.1109/JEDS.2016.2568219.

[25] F. W. Chen, H. Ilatikhameneh, T. A. Ameen, G. Klimeck, and R. Rahman, "Thickness Engineered Tunnel Field-Effect Transistors Based on Phosphorene," *IEEE Electron Device Letters*, vol. 38, no. 1, pp. 130–133, 2017.

[26] A. Prakash, H. Ilatikhameneh, P. Wu, and J. Appenzeller, "Understanding contact gating in Schottky barrier transistors from 2D channels," *Scientific Reports*, vol. 7, no. 1, pp. 1–30, 2017.

[27] A. Islam, X. Liu, B. Odhner, M. A. Tupta, and P. X. Feng, "Investigation of Electrostatic Gating in Two-Dimensional Transitional Metal Dichalcogenide (TMDC) Field Effect Transistors (FETs)," in *2018 IEEE 13th Nanotechnology Materials and Devices Conference (NMDC)*, Oct 2018, pp. 1–4.

[28] H. Ilatikhameneh, T. A. Ameen, G. Klimeck, J. Appenzeller, and R. Rahman, "Dielectric Engineered Tunnel Field-Effect Transistor," *IEEE Electron Device Letters*, vol. 36, no. 10, pp. 1097–1100, 2015, doi:10.1109/LED.2015.2474147.

[29] C. S. Pang, C. Y. Chen, T. Ameen, S. Zhang, H. Ilatikhameneh, R. Rahman, G. Klimeck, and Z. Chen, "WSe2 Homojunction Devices: Electrostatically Configurable as Diodes, MOSFETs, and Tunnel FETs for Reconfigurable Computing," *Small*, vol. 15, no. 41, p. 1902770, 2019. [Online]. Available: https://onlinelibrary.wiley.com/doi/abs/10.1002/smll.201902770

[30] G. S. Sangeetha, T. E. A. Khan, and T. A. S. Hameed, "Sige/si heterojunction tfet for analog signal applications," in *2016 International Conference on Next Generation Intelligent Systems (ICNGIS)*, Sep. 2016, pp. 1–6.

[31] P. Long, M. Povolotskyi, J. Z. Huang, J. Charles, T. Kubis, G. Klimeck, and M. J. Rodwell, "A high-current InP-channel triple heterojunction tunnel transistor design," *Device Research Conference - Conference Digest, DRC*, no. June, pp. 10–12, 2017, doi:10.1109/DRC.2017.7999437, isbn:9781509063277.

[32] Jun Z. Huang, Hesameddin Ilatikhameneh, Michael Povolotskyi, and Gerhard Klimeck, "Robust mode space approach for atomistic modeling of realistically large nanowire transistors," *Journal of Applied Physics*, vol. 123, no. 4, p. 044303, 2018, doi:10.1063/1.5010238.

[33] J. Z. Huang, P. Long, M. Povolotskyi, G. Klimeck, and M. J. W. Rodwell, "Sb- and al-free ultra-high-current tunnel fet designs," in *2017 Fifth Berkeley Symposium on Energy Efficient Electronic Systems Steep Transistors Workshop (E3S)*, Oct 2017, pp. 1–3.

[34] H. Lee, L. E. Yu, S. W. Ryu, J. W. Han, K. Jeon, D. Y. Jang, K. H. Kim, J. Lee, J. H. Kim, S. Jeon, G. Lee, J. Oh, Y. Park, W. Bae, H. Lee, J. Yang, J. Yoo,

S. Kim, and Y. K. Choi, "Sub-5nm All-Around Gate FinFET for Ultimate Scaling," in *2006 Symposium on VLSI Technology, 2006. Digest of Technical Papers.*, June 2006, pp. 58–59, doi:10.1109/VLSIT.2006.1705215.

[35] C. Schulte-Braucks, R. Pandey, R. N. Sajjad, M. Barth, R. K. Ghosh, B. Grisafe, P. Sharma, N. von den Driesch, A. Vohra, G. B. Rayner, R. Loo, S. Mantl, D. Buca, C. Yeh, C. Wu, W. Tsai, D. A. Antoniadis, and S. Datta, "Fabrication, characterization, and analysis of Ge/GeSn heterojunction p-type tunnel transistors," *IEEE Transactions on Electron Devices*, vol. 64, no. 10, pp. 4354–4362, Oct 2017, dOI:10.1109/TED.2017.2742957.

[36] M. Fujimatsu, H. Saito, and Y. Miyamoto, "71 mv/dec of sub-threshold slope in vertical tunnel field-effect transistors with gaassb/ingaas heterostructure," in *2012 International Conference on Indium Phosphide and Related Materials*, Aug 2012, pp. 25–28, dOI:10.1109/ICIPRM.2012.6403309.

[37] X. Zhao, A. Vardi, and J. A. del Alamo, "Sub-Thermal Subthreshold Characteristics in Top-Down InGaAs/InAs Heterojunction Vertical Nanowire Tunnel FETs," *IEEE Electron Device Letters*, vol. 38, no. 7, pp. 855–858, July 2017, dOI:10.1109/LED.2017.2702612.

[38] S. T. Auran Brunelli, B. Markman, A. Goswami, H.-Y. Tseng, S. Choi, C. PalmstrAom, M. Rodwell, and J. Klamkin, "Selective and confined epitaxial growth development for novel nano-scale electronic and photonic device structures," *Journal of Applied Physics*, vol. 126, no. 1, p. 015703, 2019, dOI:10.1063/1.5097174.

[39] H. Saito, Y. Miyamoto, and K. Furuya, "Fabrication of vertical InGaAs channel metal–insulator–semiconductor field effect transistor with a 15-nm-wide mesa structure and a drain current density of 7 MA/cm2," *Applied Physics Express*, vol. 3, no. 8, p. 084101, jul 2010. [Online]. Available: https://doi.org/10.1143$%$2Fapex.3.084101

[40] H. Ilatikhameneh, R. B. Salazar, G. Klimeck, R. Rahman, and J. Appenzeller, "From fowler–nordheim to nonequilibrium green's function modeling of tunneling," *IEEE Transactions on Electron Devices*, vol. 63, no. 7, pp. 2871–2878, July 2016.

[41] R. B. Salazar, H. Ilatikhameneh, R. Rahman, G. Klimeck, and J. Appenzeller, "A predictive analytic model for high-performance tunneling field-effect transistors approaching non-equilibrium Green's function simulations," *Journal of Applied Physics*, vol. 118, no. 16, 2015.

[42] H. Ilatikhameneh, T. Ameen, F. Chen, H. Sahasrabudhe, G. Klimeck, and R. Rahman, "Dramatic impact of dimensionality on the electrostatics of p-n junctions and its sensing and switching applications," *IEEE Transactions on Nanotechnology*, vol. 17, no. 2, pp. 293–298, March 2018.

[43] D. Reuter, C. Werner, a. D. Wieck, and S. Petrosyan, "Depletion characteristics of two-dimensional lateral p-n-junctions," *Applied Physics Letters*, vol. 86, no. 16, pp. 1–3, 2005.

[44] A. Nipane, S. Jayanti, A. Borah, and J. T. Teherani, "Electrostatics of lateral p-n junctions in atomically thin materials," *Journal of Applied Physics*, vol. 122, no. 19, 2017.

[45] H. Yu, A. Kutana, and B. I. Yakobson, "Carrier Delocalization in Two-Dimensional Coplanar p-n Junctions of Graphene and Metal Dichalcogenides," *Nano Letters*, vol. 16, no. 8, pp. 5032–5036, 2016.

[46] H. Ilatikhameneh, T. Ameen, B. Novakovic, Y. Tan, G. Klimeck, and R. Rahman, "Saving Moore's Law Down to 1 nm Channels with Anisotropic Effective Mass," *Scientific Reports*, vol. 6, no. August, pp. 1–6, 2016.

[47] G. B. Beneventi, E. Gnani, A. Gnudi, S. Reggiani, and G. Baccarani, "Dual-metal-gate InAs tunnel FET with enhanced turn-on steepness and high on-current," *IEEE Transactions on Electron Devices*, vol. 61, no. 3, pp. 776–784, 2014, dOI:10.1109/TED.2014.2298212.

[48] A. C. Ford, C. W. Yeung, S. Chuang, H. S. Kim, E. Plis, S. Krishna, C. Hu, and A. Javey, "Ultrathin body InAs tunneling field-effect transistors on Si substrates," *Applied Physics Letters*, vol. 98, no. 11, pp. 98–100, 2011.

[49] K. Tomioka, M. Yoshimura, and T. Fukui, "Steep-slope tunnel field-effect transistors using III-V nanowire/Si heterojunction," *Digest of Technical Papers - Symposium on VLSI Technology*, no. 2010, pp. 47–48, 2012.

[50] D. Cutaia, K. E. Moselund, H. Schmid, M. Borg, A. Olziersky, and H. Riel, "Complementary III-V heterojunction lateral NW Tunnel FET technology on Si," *Digest of Technical Papers - Symposium on VLSI Technology*, no. 619509, pp. 4–5, September 2016, doi:10.1109/VLSIT.2016.7573444.

[51] H. Ilatikhameneh, "Tunnel Field-Effect Transistors in 2-D Transition Metal Dichalcogenide Materials," *Ieee J. Explor. Solid State Computat. Devices Circuits*, vol. 1, pp. 12–18, April 2015.

[52] Y. Ma, B. Liu, A. Zhang, L. Chen, M. Fathi, C. Shen, A. N. Abbas, M. Ge, M. Mecklenburg, and C. Zhou, "Reversible Semiconducting-to-Metallic Phase Transition in Chemical Vapor Deposition Grown Monolayer $WSe_2$ and Applications for Devices," *ACS Nano*, vol. 9, no. 7, pp. 7383–7391, 2015.

[53] J. C. Slater and G. F. Koster, "Simplified lcao method for the periodic potential problem," *Phys. Rev.*, vol. 94, pp. 1498–1524, Jun 1954. [Online]. Available: https://link.aps.org/doi/10.1103/PhysRev.94.1498

[54] C. Gong, H. Zhang, W. Wang, L. Colombo, R. M. Wallace, and K. Cho, "Band alignment of two-dimensional transition metal dichalcogenides: Application in tunnel field effect transistors," *Applied Physics Letters*, vol. 103, no. 5, 2013.

[55] K. Novoselov, a. Mishchenko, a. Carvalho, and a. H. Castro Neto, "2d materials and van der waals heterostructures," *Science*, vol. 353, no. 6298, pp. 1–25, 2016. [Online]. Available: http://arxiv.org/abs/1608.03059

[56] K. C. Wang, T. K. Stanev, D. Valencia, J. Charles, A. Henning, V. K. Sangwan, A. Lahiri, D. Mejia, P. Sarangapani, M. Povolotskyi, A. Afzalian, J. Maassen, G. Klimeck, M. C. Hersam, L. J. Lauhon, N. P. Stern, and T. Kubis, "Control of interlayer physics in 2H transition metal dichalcogenides," *Journal of Applied Physics*, vol. 122, no. 22, 2017. [Online]. Available: http://dx.doi.org/10.1063/1.5005958

[57] H. Ilatikhameneh, G. Klimeck, J. Appenzeller, and R. Rahman, "Scaling Theory of Electrically Doped 2D Transistors," *IEEE Electron Device Letters*, vol. 36, no. 7, pp. 726–728, 2015, doi:10.1109/LED.2015.2436356, issn:0741-3106.

[58] M. Luisier, A. Schenk, W. Fichtner, and G. Klimeck, "Atomistic simulation of nanowires in the $sp^3d^5s^*$ tight-binding formalism: From boundary conditions to strain calculations," *Phys. Rev. B*, vol. 74, p. 205323, Nov 2006. [Online]. Available: https://link.aps.org/doi/10.1103/PhysRevB.74.205323

[59] P. Flynn and M. Hill, "Quantum Dielectric Theory of Electronegativity in Covalent Systems. I. Electronic Dielectric Constant," vol. 2, no. 1934, 1955.

[60] V. Wang, Y. Kawazoe, and W. T. Geng, "Native point defects in few-layer phosphorene," *Physical Review B - Condensed Matter and Materials Physics*, vol. 91, no. 4, pp. 1–9, 2015.

[61] A. Kumar and P. K. Ahluwalia, "Tunable dielectric response of transition metals dichalcogenides MX 2 (M=Mo, W; X=S, Se, Te): Effect of quantum confinement," *Physica B: Condensed Matter*, vol. 407, no. 24, pp. 4627–4634, 2012. [Online]. Available: http://dx.doi.org/10.1016/j.physb.2012.08.034

[62] S. Steiger, M. Povolotskyi, H. H. Park, T. Kubis, and G. Klimeck, "NEMO5: A parallel multiscale nanoelectronics modeling tool," *IEEE Transactions on Nanotechnology*, vol. 10, no. 6, pp. 1464–1474, 2011.

[63] J. E. Fonseca, T. Kubis, M. Povolotskyi, B. Novakovic, a. Ajoy, G. Hegde, H. Ilatikhameneh, Z. Jiang, P. Sengupta, Y. Tan, and G. Klimeck, "Efficient and realistic device modeling from atomic detail to the nanoscale," *Journal of Computational Electronics*, vol. 12, no. 4, pp. 592–600, 2013.

[64] H. Ilatikhameneh, T. A. Ameen, C. Chen, G. Klimeck, and R. Rahman, "Sensitivity challenge of steep transistors," *IEEE Transactions on Electron Devices*, vol. 65, no. 4, pp. 1633–1639, April 2018.

[65] M. Luisier and G. Klimeck, "Atomistic full-band simulations of silicon nanowire transistors: Effects of electron-phonon scattering," *Physical Review B - Condensed Matter and Materials Physics*, vol. 80, no. 15, pp. 1–11, 2009.

[66] W. G. Vandenberghe, A. S. Verhulst, B. Sorée, W. Magnus, G. Groeseneken, Q. Smets, M. Heyns, M. V. Fischetti, and W. Magnus, "Figure of merit for and identification of sub-60 mV / decade devices Figure of merit for and identification of sub-60 mV / decade devices," vol. 013510, no. 2013, 2016.

[67] P. Long, J. Z. Huang, M. Povolotskyi, D. Verreck, J. Charles, T. Kubis, G. Klimeck, M. J. W. Rodwell, and B. H. Calhoun, "A tunnel fet design for high-current, 120 mv operation," in *2016 IEEE International Electron Devices Meeting (IEDM)*, Dec 2016, pp. 30.2.1–30.2.4, dOI:10.1109/IEDM.2016.7838511.

[68] K. Wang, Y. Chu, D. Valencia, J. Geng, J. Charles, P. Sarangapani, and T. Kubis, "Nonequilibrium green's function method: Büttiker probes for carrier generation and recombination," in *2018 International Conference on Simulation of Semiconductor Processes and Devices (SISPAD)*, Sep. 2018, pp. 5–8, dOI:10.1109/SISPAD.2018.8551714.

[69] T. A. Ameen, H. Ilatikhameneh, J. Z. Huang, M. Povolotskyi, R. Rahman, and G. Klimeck, "Combination of Equilibrium and Nonequilibrium Carrier Statistics into an Atomistic Quantum Transport Model for Tunneling Heterojunctions," *IEEE Transactions on Electron Devices*, vol. 64, no. 6, pp. 2512–2518, 2017, doi:10.1109/TED.2017.2690626.

[70] J. Z. Huang, P. Long, M. Povolotskyi, H. Ilatikhameneh, T. a. Ameen, R. Rahman, M. J. Rodwell, and G. Klimeck, "A Multiscale Modeling of Triple-Heterojunction Tunneling FETs," *IEEE Transactions on Electron Devices*, vol. 64, no. 6, pp. 2728–2735, 2017.

[71] J. Geng, P. Sarangapani, K.-C. Wang, E. Nelson, B. Browne, C. Wordelman, J. Charles, Y. Chu, T. Kubis, and G. Klimeck, "Quantitative multiscale, multi-physics quantum transport modeling of gan-based light emitting diodes," *physica status solidi (a)*, vol. 215, no. 9, p. 1700662, 2018, dOI:10.1002/pssa.201700662.

[72] C. S. Lent and D. J. Kirkner, "The quantum transmitting boundary method," *Journal of Applied Physics*, vol. 67, no. 10, pp. 6353–6359, 1990.

[73] M. Luisier and G. Klimeck, "Atomistic full-band simulations of silicon nanowire transistors: Effects of electron-phonon scattering," *Physical Review B - Condensed Matter and Materials Physics*, vol. 80, no. 15, pp. 1–11, 2009.

[74] S. Datta, *Quantum Transport: Atom to Transistor.* Cambridge University Press, 2005, DOI:10.1017/CBO9781139164313.

[75] S. Datta, "Nanoscale device modeling: the Green's function method," *Superlattices and Microstructures*, vol. 28, no. 4, pp. 253–278, Oct 2000, DOI:10.1006/SPMI.2000.0920.

[76] R. Lake, G. Klimeck, R. C. Bowen, and D. Jovanovic, "Single and multiband modeling of quantum electron transport through layered semiconductor devices," *Journal of Applied Physics*, vol. 81, no. 12, pp. 7845–7869, 1997. [Online]. Available: https://doi.org/10.1063/1.365394

[77] C. Chen, T. A. Ameen, H. Ilatikhameneh, R. Rahman, G. Klimeck, and J. Appenzeller, "Channel thickness optimization for ultrathin and 2-d chemically doped tfets," *IEEE Transactions on Electron Devices*, vol. 65, no. 10, pp. 4614–4621, Oct 2018.

[78] J. Towns, T. Cockerill, M. Dahan, I. Foster, K. Gaither, A. Grimshaw, V. Hazlewood, S. Lathrop, D. Lifka, G. D. Peterson, R. Roskies, J. Scott, and N. Wilkins-Diehr, "XSEDE: Accelerating Scientific Discovery," *Computing in Science & Engineering*, vol. 16, no. 05, pp. 62–74, sep 2014, dOI: 10.1109/MCSE.2014.80.

[79] G. Mil'nikov, N. Mori, and Y. Kamakura, "Equivalent transport models in atomistic quantum wires," *Physical Review B - Condensed Matter and Materials Physics*, vol. 85, no. 3, pp. 1–11, 2012.

[80] W. J. Jeong, J. Seo, and M. Shin, "Efficient TB-NEGF simulations of ultra-thin body tunnel FETs," *International Conference on Simulation of Semiconductor Processes and Devices, SISPAD*, no. 3, pp. 81–84, 2016, dOI:10.1109/SISPAD.2016.7605153.

[81] G. Klimeck, R. Lake, R. C. Bowen, W. R. Frensley, and T. S. Moise, "Quantum device simulation with a generalized tunneling formula," *Applied Physics Letters*, vol. 67, no. 17, pp. 2539–2541, 1995. [Online]. Available: https://doi.org/10.1063/1.114451

[82] G. Klimeck, R. Lake, S. Datta, and G. W. Bryant, "Elastic and inelastic scattering in quantum dots in the coulomb-blockade regime," *Phys. Rev. B*, vol. 50, pp. 5484–5496, Aug 1994. [Online]. Available: https://link.aps.org/doi/10.1103/PhysRevB.50.5484

[83] R. Lake, G. Klimeck, R. C. Bowen, and D. Jovanovic, "Single and multiband modeling of quantum electron transport through layered semiconductor devices," *Journal of Applied Physics*, vol. 81, no. 12, pp. 7845–7869, 1997.

[84] P. Long, M. Povolotskyi, J. Z. Huang, H. Ilatikhameneh, T. Ameen, R. Rahman, T. Kubis, G. Klimeck, and M. J. W. Rodwell, "Extremely high simulated ballistic currents in triple-heterojunction tunnel transistors," in *2016 74th Annual Device Research Conference (DRC)*, June 2016, pp. 1–2.

[85] P. Long, J. Z. Huang, M. Povolotskyi, D. Verreck, G. Klimeck, and M. J. W. Rodwell, "High-current InP-based triple heterojunction tunnel transistors," in *2016 Compound Semiconductor Week (CSW) [Includes 28th International Conference on Indium Phosphide Related Materials (IPRM) 43rd International Symposium on Compound Semiconductors (ISCS)*, June 2016, pp. 1–2.

[86] J. Z. Huang, P. Long, M. Povolotskyi, G. Klimeck, and M. J. Rodwell, "P-Type Tunnel FETs with Triple Heterojunctions," *IEEE Journal of the Electron Devices Society*, vol. 4, no. 6, pp. 410–415, 2016, dOI:10.1109/JEDS.2016.2614915.

[87] A. Tankasala, J. Salfi, J. Bocquel, B. Voisin, M. Usman, G. Klimeck, M. Y. Simmons, L. C. L. Hollenberg, S. Rogge, and R. Rahman, "Two-electron states of a group-v donor in silicon from atomistic full configuration interactions," *Phys. Rev. B*, vol. 97, p. 195301, May 2018. [Online]. Available: https://link.aps.org/doi/10.1103/PhysRevB.97.195301

[88] F. Mazzola, C. Y. Chen, R. Rahman, X. G. Zhu, C. M. Polley, T. Balasubramanian, P. D. C. King, P. Hofmann, J. A. Miwa, and W. Justin, "The sub-band structure of atomically sharp dopant profiles in Silicon," *arXiv e-prints*, p. arXiv:1904.10929, Apr 2019, provided by the SAO/NASA Astrophysics Data System. [Online]. Available: https://ui.adsabs.harvard.edu/abs/2019arXiv190410929M

[89] D. Martín and C. Algora, "Temperature-dependent GaSb material parameters for reliable thermophotovoltaic cell modelling," *Semiconductor Science and Technology*, vol. 19, no. 8, pp. 1040–1052, jul 2004.

[90] S. Karishy, P. Ziadé, G. Sabatini, H. Marinchio, C. Palermo, L. Varani, J. Mateos, and T. Gonzalez, "Review of electron transport properties in bulk InGaAs and InAs at room temperature." *Lithuanian Journal of Physics*, vol. 55, no. 4, pp. 305–314, 2015.

[91] S. Krivec, M. Poljak, and T. Suligoj, "Electron mobility in ultra-thin InGaAs channels: Impact of surface orientation and different gate oxide materials," *Solid-State Electronics*, vol. 115, pp. 109–119, 2016. [Online]. Available: http://dx.doi.org/10.1016/j.sse.2015.08.009

[92] A. I. Khan, C. W. Yeung, Chenming Hu, and S. Salahuddin, "Ferroelectric negative capacitance mosfet: Capacitance tuning antiferroelectric operation," in *2011 International Electron Devices Meeting*, Dec 2011, pp. 11.3.1–11.3.4, DOI:10.1109/IEDM.2011.6131532.

[93] K. S. Li, P. G. Chen, T. Y. Lai, C. H. Lin, C. C. Cheng, C. C. Chen, Y. J. Wei, Y. F. Hou, M. H. Liao, M. H. Lee, M. C. Chen, J. M. Sheih, W. K. Yeh, F. L. Yang, S. Salahuddin, and C. Hu, "Sub-60mV-swing negative-capacitance FinFET without hysteresis," *Technical Digest - International Electron Devices Meeting, IEDM*, vol. 2016-February, no. December, pp. 22.6.1–22.6.4, 2015, DOI:10.1109/IEDM.2015.7409760.

[94] T. A. Ameen, H. Ilatikhameneh, P. Fay, A. Seabaugh, R. Rahman, and G. Klimeck, "Alloy engineered Nitride Tunneling Field-Effect Transistor: a solution for the challenge of heterojunction TFETs," *IEEE Transactions on Electron Devices*, vol. 66, no. 1, pp. 736–742, Jan 2019, doi:10.1109/TED.2018.2877753.

[95] U. E. Avci and I. A. Young, "Heterojunction TFET Scaling and resonant-TFET for steep subthreshold slope at sub-9nm gate-length," in *2013 IEEE International Electron Devices Meeting*, Dec 2013, pp. 4.3.1–4.3.4, doi:10.1109/IEDM.2013.6724559.

[96] T. A. Ameen, H. Ilatikhameneh, G. Klimeck, and R. Rahman, "Few-layer phosphorene: An ideal 2D material for tunnel transistors," *Scientific Reports*, vol. 6, no. June, pp. 1–7, 2016, doi:10.1038/srep28515.

[97] Jun Z. Huang, Pengyu Long, Michael Povolotskyi, Gerhard Klimeck, Mark J.W. Rodwell, "Sb and Al free ultra high current tunnel FET design," *2017 Fifth Berkeley Symposium on Energy Efficient Electronic Systems & Steep Transistors Workshop (E3S)*, no. IEEE, pp. 8–10, 2017.

[98] Y. Tan, M. Povolotskyi, T. Kubis, T. B. Boykin, and G. Klimeck, "Transferable tight-binding model for strained group IV and III-V materials and heterostructures," *Physical Review B*, vol. 94, no. 4, pp. 1–17, 2016, DOI:10.1103/PhysRevB.94.045311.

[99] T. A. Ameen, H. Ilatikhameneh, A. Tankasala, Y. Hsueh, J. Charles, J. Fonseca, M. Povolotskyi, J. O. Kim, S. Krishna, M. S. Allen *et al.*, "Theoretical study of strain-dependent optical absorption in a doped self-assembled inas/ingaas/gaas/algaas quantum dot," *Beilstein Journal of Nanotechnology*, vol. 9, no. 1, pp. 1075–1084, 2018.

[100] C. Y. Chen, H. Ilatikhameneh, J. Z. Huang, G. Klimeck, and M. Povolotskyi, "Impact of body thickness and scattering on III-V triple heterojunction Fin-TFET modeled with atomistic mode space approximation," *arXiv e-prints*, Feb 2020, arxiV:2002.04220. [Online]. Available: https://arxiv.org/abs/2002.04220

[101] A. Tabata, T. Benyattou, G. Guillot, Z. Sobiesierski, S. A. Clark, R. H. Williams, M. Gendry, G. Hollinger, and P. Viktorovitch, "Surface InAs/InP quantum wells: epitaxial growth and characterization," in *[Proceedings 1991] Third International Conference Indium Phosphide and Related Materials*, April 1991, pp. 496–499, DOI:10.1109/ICIPRM.1991.147421.

[102] Gan Feng and Kunishige Oe and Masahiro Yoshimoto, "Temperature dependence of Bi behavior in MBE growth of InGaAs/InP," *Journal of Crystal Growth*, vol. 301-302, pp. 121 – 124, 2007, 14th International Conference on Molecular Beam Epitaxy, DOI:https://doi.org/10.1016/j.jcrysgro.2006.11.242. [Online]. Available: http://www.sciencedirect.com/science/article/pii/S002202480601270X

[103] B. Lambert, Y. Toudic, Y. Rouillard, M. Gauneau, M. Baudet, F. Alard, I. Valiente, and J. C. Simon, "High reflectivity 1.55 m (Al)GaAsSb/AlAsSb Bragg reflector lattice matched on InP substrates," *Applied Physics Letters*, vol. 66, no. 4, pp. 442–444, 1995, DOI:10.1063/1.114050. [Online]. Available: https://doi.org/10.1063/1.114050

[104] J. W. Matthews and A. E. Blakeslee, "Defects in epitaxial multilayers. I. Misfit dislocations," *Journal of Crystal Growth*, vol. 27, pp. 118–125, dec 1974, DOI:10.1016/0022-0248(74)90424-2.

[105] T. Akazaki, K. Arai, T. Enoki, and Y. Ishii, "Improved InAlAs/InGaAs HEMT characteristics by inserting an InAs layer into the InGaAs channel," *IEEE Electron Device Letters*, vol. 13, no. 6, pp. 325–327, 1992, DOI:10.1109/55.145073.

[106] V. Nagavarapu, R. Jhaveri, and J. C. Woo, "The tunnel source (PNPN) n-MOSFET: A novel high performance transistor," *IEEE Transactions on Electron Devices*, vol. 55, no. 4, pp. 1013–1019, 2008.

[107] D. B. Abdi and M. J. Kumar, "In-built N+ Pocket p-n-p-n tunnel field-effect transistor," *IEEE Electron Device Letters*, vol. 35, no. 12, pp. 1170–1172, 2014.

[108] S. Baronia, K. Nigam, D. Sharma, B. R. Raad, and P. Kondekar, "A novel approach of PNPN dual metal double gate tunnel field effect transistor for improving DC characteristics," *Proceedings of 2016 International Conference on Advanced Communication Control and Computing Technologies, ICACCCT 2016*, no. 978, pp. 44–47, 2017.

[109] D. B. Abdi and M. J. Kumar, "2-D Threshold Voltage Model for the Double-Gate p-n-p-n TFET With Localized Charges," *IEEE Transactions on Electron Devices*, vol. 63, no. 9, pp. 3663–3668, Sep. 2016, DOI:10.1109/TED.2016.2589927.

[110] H. Ilatikhameneh, G. Klimeck, J. Appenzeller, and R. Rahman, "Scaling Theory of Electrically Doped 2D Transistors," *IEEE Electron Device Letters*, vol. 36, no. 7, pp. 726–728, 2015, doi:10.1109/LED.2015.2436356, issn:0741-3106.

[111] H. Ilatikhameneh, R. B. Salazar, G. Klimeck, R. Rahman, and J. Appenzeller, "From fowler–nordheim to nonequilibrium green's function modeling of tunneling," *IEEE Transactions on Electron Devices*, vol. 63, no. 7, pp. 2871–2878, July 2016, DOI:10.1109/TED.2016.2565582.

[112] B. E. Kane, "A Silicon-based nuclear spin quantum computer," *Nature*, vol. 393, no. 6681, pp. 133–137, 1998, doi:10.1038/30156, isbn:0028-0836, pmid:73619900037.

[113] R. Vrijen, E. Yablonovitch, K. Wang, H. Jiang, A. Balandin, V. Roychowdhury, T. Mor, and D. DiVincenzo, "Electron spin resonance transistors for quantum computing in Silicon-Germanium heterostructures," *Physical Review A*, vol. 62, 05 1999, doi:10.1103/PhysRevA.62.012306.

[114] L. C. Hollenberg, A. S. Dzurak, C. Wellard, A. R. Hamilton, D. J. Reilly, G. J. Milburn, and R. G. Clark, "Charge-based quantum computing using single donors in semiconductors," *Physical Review B - Condensed Matter and Materials Physics*, vol. 69, no. 11, pp. 2–5, 2004.

[115] Y. Wang, C.-Y. Chen, G. Klimeck, M. Y. Simmons, and R. Rahman, "Characterizing Si:P quantum dot qubits with spin resonance techniques," *Scientific Reports*, vol. 6, no. August, p. 31830, 2016. [Online]. Available: http://www.nature.com/articles/srep31830

[116] A. Tankasala and H. Ilatikhameneh, "Quantum-kit: Simulating shor's factorization of 24-bit number on desktop," *arXiv preprint arXiv:1908.07187*, 2019.

[117] A. Tankasala, Y. Wang, G. Klimeck, and R. Rahman, "Atomistic configuration interaction simulations of two-electron states of donors in silicon," in *APS Meeting Abstracts*, 2015.

[118] F. J. Ruess, L. Oberbeck, M. Y. Simmons, K. E. J. Goh, A. R. Hamilton, T. Hallam, S. R. Schofield, N. J. Curson, and R. G. Clark, "Toward atomic-scale device fabrication in silicon using scanning probe microscopy," *Nano Letters*, vol. 4, no. 10, pp. 1969–1973, 2004.

[119] M. Y. Simmons, S. R. Schofield, J. L. O'Brien, N. J. Curson, L. Oberbeck, T. Hallam, and R. G. Clark, "Towards the atomic-scale fabrication of a silicon-based solid state quantum computer," *Surface Science*, vol. 532-535, pp. 1209–1218, 2003.

[120] B. Weber, Y. H. M. Tan, S. Mahapatra, T. F. Watson, H. Ryu, R. Rahman, L. C. L. Hollenberg, G. Klimeck, and M. Y. Simmons, "Spin blockade and exchange in Coulomb-confined silicon double quantum dots." *Nature nanotechnology*, vol. 9, no. 6, pp. 430–5, jun 2014. [Online]. Available: http://www.ncbi.nlm.nih.gov/pubmed/24727686

[121] S. Lee, H. Ryu, H. Campbell, L. C. L. Hollenberg, M. Y. Simmons, and G. Klimeck, "Electronic structure of realistically extended atomistically resolved disordered Si:P delta doped layers," *Physical Review B - Condensed Matter and Materials Physics*, vol. 84, no. 20, pp. 1–9, 2011.

[122] S. Ristic, A. Prijic, and Z. Prijic, "Dependence of static dielectric constant of silicon on resistivity at room temperature," *Serbian Journal of Electrical Engineering*, vol. 1, pp. 237–247, 01 2004.

[123] R. Rahman, C. J. Wellard, F. R. Bradbury, M. Prada, J. H. Cole, G. Klimeck, and L. C. L. Hollenberg, "High Precision Quantum Control of Single Donor Spins in Silicon," vol. 036403, no. July, pp. 3–6, 2007.

[124] G. P. Lansbergen, R. Rahman, C. J. Wellard, I. Woo, J. Caro, N. Collaert, S. Biesemans, G. Klimeck, L. C. L. Hollenberg, and S. Rogge, "Gate-induced quantum-confinement transition of a single dopant atom in a silicon FinFET," *Nature Physics*, vol. 4, no. 8, pp. 656–661, 2008.

[125] Y. L. Hsueh, H. Büch, Y. Tan, Y. Wang, L. C. L. Hollenberg, G. Klimeck, M. Y. Simmons, and R. Rahman, "Spin-lattice relaxation times of single donors and donor clusters in silicon," *Physical Review Letters*, vol. 113, no. 24, pp. 1–5, 2014.

[126] Y. Hsueh, A. Tankasala, Y. Wang, G. Klimeck, M. Simmons, and R. Rahman, "Phonon induced two-electron relaxation in two donor qubits in silicon," in *APS March Meeting Abstracts*, 2016.

[127] Samuel J. Hile, Lukas Fricke, Matthew G. House, Eldad Peretz, Chin Yi Chen, Yu Wang, Matthew Broome, Samuel K. Gorman1, Joris G. Keizer, Rajib Rahman, and Michelle Y. Simmons, "Addressable electron spin resonance using donors and donor molecules in silicon," *Science Advances*, vol. 4, no. 7, p. eaaq1459, 2018, doi:10.1126/sciadv.aaq1459.

[128] M. Usman, J. Bocquel, J. Salfi, B. Voisin, A. Tankasala, R. Rahman, M. Y. Simmons, S. Rogge, and L. C. Hollenberg, "Spatial metrology of dopants in silicon with exact lattice site precision," *Nature Nanotechnology*, vol. 11, no. 9, pp. 763–768, 2016.

[129] J. C. Slater and G. F. Koster, "Simplified lcao method for the periodic potential problem," *Phys. Rev.*, vol. 94, pp. 1498–1524, Jun 1954. [Online]. Available: https://link.aps.org/doi/10.1103/PhysRev.94.1498

[130] W. Kohn and L. J. Sham, "Self-consistent equations including exchange and correlation effects," *Phys. Rev.*, vol. 140, pp. A1133–A1138, Nov 1965. [Online]. Available: https://link.aps.org/doi/10.1103/PhysRev.140.A1133

[131] M. Luisier, A. Schenk, W. Fichtner, "Full-band atomistic study of source-to-drain tunneling in si nanowire transistors," in *Simulation of Semiconductor Processes and Devices 2007*, T. Grasser and S. Selberherr, Eds. Vienna: Springer Vienna, 2007, pp. 221–224, DOI:10.1007/978-3-211-72861-1_52.

[132] X. Mi, S. Kohler, and J. R. Petta, "Landau-Zener interferometry of valley-orbit states in Si/SiGe double quantum dots," *Phys. Rev. B*, vol. 98, p. 161404, Oct 2018, doi:10.1103/PhysRevB.98.161404. [Online]. Available: https://link.aps.org/doi/10.1103/PhysRevB.98.161404

[133] J. Salfi, B. Voisin, A. Tankasala, J. Bocquel, M. Usman, M. Simmons, L. Hollenberg, R. Rahman, and S. Rogge, "Valley filtering in spatial maps of coupling between silicon donors and quantum dots," *Physical Review X*, vol. 8, no. 3, p. 031049, 2018.

[134] M. L. V. Tagliaferri, P. L. Bavdaz, W. Huang, A. S. Dzurak, D. Culcer, and M. Veldhorst, "Impact of valley phase and splitting on readout of silicon spin qubits," *Phys. Rev. B*, vol. 97, p. 245412, Jun 2018. [Online]. Available: https://link.aps.org/doi/10.1103/PhysRevB.97.245412

[135] F. A. Zwanenburg, A. S. Dzurak, A. Morello, M. Y. Simmons, L. C. L. Hollenberg, G. Klimeck, S. Rogge, S. N. Coppersmith, and M. A. Eriksson, "Silicon quantum electronics," *Reviews of Modern Physics*, vol. 85, no. 3, pp. 961–1019, jul 2013, doi:10.1103/RevModPhys.85.961. [Online]. Available: http://link.aps.org/doi/10.1103/RevModPhys.85.961

[136] T. B. Boykin, G. Klimeck, M. A. Eriksson, M. Friesen, S. N. Coppersmith, P. V. Allmen, F. Oyafuso, and S. Lee, "Valley splitting in strained silicon quantum wells," *Applied Physics Letters*, vol. 84, no. 1, p. 115, 2004, doi:10.1063/1.1637718, issn:00036951. [Online]. Available: http://scitation.aip.org/content/aip/journal/apl/84/1/10.1063/1.1637718

[137] T. B. Boykin, G. Klimeck, M. Friesen, S. N. Coppersmith, P. V. Allmen, F. Oyafuso, and S. Lee, "Valley splitting in low-density quantum-confined heterostructures studied using tight-binding models," *Physical Review B - Condensed Matter and Materials Physics*, vol. 70, no. 16, pp. 1–12, 2004, doi:10.1103/PhysRevB.70.165325, isbn:1098-0121\n1550-235X, issn:01631829.

[138] M. O. Nestoklon, E. L. Ivchenko, J. M. Jancu, and P. Voisin, "Electric field effect on electron spin splitting in SiGe/Si quantum wells," *Physical Review B*, vol. 77, p. 155328, 2008, arxivId:0712.1955, doi:10.1103/PhysRevB.77.155328, issn:1098-0121. [Online]. Available: http://arxiv.org/abs/0712.1955

[139] J. A. Miwa, P. Hofmann, M. Y. Simmons, and J. W. Wells, "Direct measurement of the band structure of a buried two-dimensional electron gas," *Physical Review Letters*, vol. 110, no. 13, pp. 1–5, 2013, doi:10.1103/PhysRevLett.110.136801, issn:00319007, pmid:23581353.

[140] J. A. Miwa, O. Warschkow, D. J. Carter, N. A. Marks, F. Mazzola, M. Y. Simmons, and J. W. Wells, "Valley splitting in a silicon quantum device platform," *Nano Letters*, vol. 14, no. 3, pp. 1515–1519, 2014, doi:10.1021/nl404738j, issn:15306992, pmid:24571617.

[141] Y. A. Bychkov and E. I. Rashba, "Oscillatory effects and the magnetic susceptibility of carriers in inversion layers," *Journal of Physics C: Solid State Physics*, vol. 17, no. 33, pp. 6039–6045, nov 1984, doi:10.1088/0022-3719/17/33/015.

[142] G. Dresselhaus, "Spin-orbit coupling effects in zinc blende structures," *Phys. Rev.*, vol. 100, pp. 580–586, Oct 1955, doi:10.1103/PhysRev.100.580. [Online]. Available: https://link.aps.org/doi/10.1103/PhysRev.100.580

[143] E. Gawlinski, T. Dzurak, and R. A. Tahir Kheli, "Direct and exchange correlation carrier interaction effects in a resonant tunnel diode," *Journal of Applied Physics*, vol. 72, no. 8, pp. 3562–3569, 1992, doi:10.1063/1.351435. [Online]. Available: https://doi.org/10.1063/1.351435

[144] R. Parr and Y. Weitao, *Density-Functional Theory of Atoms and Molecules*, ser. International Series of Monographs on Chemistry. Oxford University Press, 1994, isbn: 9780195357738, [Online] Available: https://books.google.com/books?id=mGOpScSIwU4C.

[145] A. J. Holt, S. K. Mahatha, R. M. Stan, F. S. Strand, T. Nyborg, D. Curcio, A. Schenk, S. P. Cooil, M. Bianchi, J. W. Wells, P. Hofmann, and J. A. Miwa, "Observation and origin of the $\Delta$-manifold in Si:P $\delta$-layers," Nov 2019. [Online]. Available: http://arxiv.org/abs/1911.08274

VITA

VITA

Chin-Yi Chen receives her B.S. in Physics from National Central University, Taiwan, and M.S in Optoelectronic from National Taiwan University, Taiwan. She has experience in memory device design and GaN HEMT simulation. Her Ph.D. work at Purdue Universality focuses on semiconductor device optimization using atomistic quantum simulations. Her list of publication is as below:

**First author publications:**

1. *"Channel thickness optimization for ultra-thin and 2D chemically doped TFETs."*, C. Chen, T. A. Ameen, H. Ilatikhameneh, R. Rahman, G. Klimeck and J. Appenzeller, in IEEE Transactions on Electron Devices, vol. 65, no. 10, pp. 4614-4621, Oct. 2018. DOI: 10.1109/TED.2018.2862408 **(Documented in Ch2)**

2. *"Impact of body thickness and scattering on III-V triple heterojunction double-gated TFET modeled with atomistic mode space approximation."*, Chin-Yi Chen and Hesameddin Ilatikhameneh and Jun Z. Huang and Gerhard Klimeck and Michael Povolotskyi, 2020, https://arxiv.org/abs/2002.04220, **(Documented in Ch3)**

3. *"Engineering doping profile of triple heterojunction TFETs using atomistic quantum transport simulations."*, Chin-Yi, Chen et. al. **(Documented in Ch4)**

**First theory author publications:**

1. *"The Sub-band Structure of Atomically Sharp Dopant Profiles in Silicon."*, Federico Mazzola, Chin-Yi Chen, Rajib Rahman, Xie-Gang Zhu, Craig M Polley, Thiagarajan Balasubramanian, Phil DC King, Philip Hofmann, Jill A Miwa, Justin W Wells, 2019, https://arxiv.org/abs/1904.10929 **(Documented in Ch5)**

2. *"WSe2 Homojunction Devices: Electrostatically Configurable as Diodes, MOS-FETs, and Tunnel FETs for Reconfigurable Computing."*, C. S. Pang, C. Y.

Chen, T. Ameen, S. J. Zhang, H. Ilatikhameneh, R. Rahman, G. Klimeck, Z. H. Chen, Small 2019, 15, 1902770. https://doi.org/10.1002/smll.201902770

3. *"Addressable electron spin resonance using donors and donor molecules in silicon."*, Samuel J Hile, Lukas Fricke, Matthew G House, Eldad Peretz, Chen Chin-Yi, Yu Wang, Matthew Broome, Samuel K Gorman, Joris G Keizer, Rajib Rahman, and Michelle Y Simmons, (2018), Science Advances, 4(7), eaaq1459. http://doi.org/10.1126/sciadv.aaq1459

**Co-author publications:**

1. *"Sensitivity Challenge of Steep Transistors."*, Hesameddin Ilatikhameneh, Tarek Ameen, ChinYi Chen, Gerhard Klimeck, Rajib Rahman, in IEEE Transactions on Electron Devices, vol. 65, no. 4, pp. 1633-1639, April 2018. DOI: 10.1109/TED.2018.2808040

2. *"All-electrical control of donor-bound electron spin qubits in silicon."*, Yu Wang, Chin-Yi Chen, Gerhard Klimeck, Michelle Y. Simmons, and Rajib Rahman, arXiv:1703.05370, https://arxiv.org/abs/1703.05370

3. *"Characterizing Si:P quantum dot qubits with spin resonance techniques."*, Yu Wang, Chin-Yi Chen, Gerhard Klimeck, Michelle Simmons, Rajib Rahman; Scientific Reports 6, Article number: 31830 (2016); DOI:10.1038/srep31830